8-2009

Single Walled Carbon Nanotube Networks as Transparent Conductors

Matthew Patrick Garrett
University of Tennessee - Knoxville

To the Graduate Council:

I am submitting herewith a dissertation written by Matthew Patrick Garrett entitled "Single Walled Carbon Nanotube Networks as Transparent Conductors." I have examined the final electronic copy of this dissertation for form and content and recommend that it be accepted in partial fulfillment of the requirements for the degree of Doctor of Philosophy, with a major in Physics.

Robert Compton, Major Professor

We have read this dissertation and recommend its acceptance:

Bin Hu, John Quinn, Hanno Weitering

Accepted for the Council:

Carolyn R. Hodges

Vice Provost and Dean of the Graduate School

(Original signatures are on file with official student records.)

To the Graduate Council:
I am submitting herewith a dissertation written by Matthew Patrick Garrett entitled "Single Walled Carbon Nanotube Networks as Transparent Conductors." I have examined the final electronic copy of this dissertation for form and content and recommend that it be accepted in partial fulfillment of the requirements for the degree of Doctor of Philosophy, with a major in Physics.

Robert Compton, Major Professor

We have read this dissertation
and recommend its acceptance:

Bin Hu_____

John Quinn_____

Hanno Weitering_____

Accepted for the Council:

Carolyn R. Hodges_____
Vice Provost and Dean of the Graduate School

(Original signatures are on file with official student records.)

Single Walled Carbon Nanotube Networks as Transparent Conductors

A Dissertation

Presented for the

Doctor of Philosophy

Degree

The University of Tennessee, Knoxville

Matthew Patrick Garrett

August 2009

Acknowledgements

I could not imagine turning in this dissertation without thanking Dave Geohegan, my research adviser. He provided me with funding, equipment, and a steady supply of new ideas and rigorous critique. I don't think he could have imagined what my stay in his group would evolve into when he took me on as a part-time summer student the year I was studying for my qualifying exams. Ilia Ivanov deserves a huge amount of credit also, as he is the person most familiar with my project, putting up with me in his lab space even in the early days when I knew nothing about what I was doing. He helped me getting my experiments going, worked with me analyzing all my data, and was the first person to show up and help when anything in the lab wasn't working.

I must also thank Bob Compton, who served in official capacity as my adviser, since Dave couldn't formally hold that position. Always willing to look at anything I'd done, no matter how far outside his area of expertise, his years of experience working with students and familiarity with the physics program proved invaluable, especially in the later stages of forging my way towards graduation.

I must also acknowledge the work of Yue Wu, Zhihuai Xu, and Ming Shao, all of the Material Science and Engineering Department, as they fabricated the OLED and OPV devices from the films I prepared and provided me with the device performance results discussed in chapter 8. They deserve as much credit as I do for the results in that chapter.

It would be impossible to name everyone that aided in my progress not just in the Multiscale Functionality group but at CNMS as a whole, but they deserve my appreciation also, for making the CNMS an enjoyable place to work, and for helping me with anything I needed for my research.

Abstract

A variety of technological applications depend on transparent conducting films, and carbon nanotubes have the properties required to serve in that role. Single-walled carbon nanotube networks have been studied as transparent conductors in order to understand and optimize their electrical and optical properties. Nanotube films are complex networks of semiconducting and metallic nanotubes, bundled and branched in multifarious directions, with different strength connections between bundles. Chemical modification of nanotubes and inclusion of non-nanotube material can further alter network properties. Separating the contributions of all aspects of the network is a necessary but daunting task in order to optimize nanotube films.

To understand and optimize film conductivity, the effect of sonication on nanotubes in several dispersants was examined. Film transmittance and resistance was found to depend on the method of dispersion of the starting material, and the characteristics of a good dispersant were outlined.

A purification method was developed specifically for SWNT transparent conductors, eliminating the problems of more complicated purification procedures which were developed for general purification. Our single-step centrifugation purification procedure was shown to achieve similar yield and purity films as multi-step acid-oxidation purification.

The films were doped, lowering network conductivity by a multiplicative factor, dependent on the method of dispersion and dopant. A linear relationship was found between the intensity of absorbance spectrum's first semiconducting transition and the change in film conductivity upon

doping. The contributions of doping to bundle and junction conductivity have been separated by impedance spectroscopy modeling.

Networks of transmittances up to 98%T have been prepared to determine the lower limit of conductivity for a SWNT film. It was shown that the percolation threshold of the networks depend on nanotube purity and dispersant. A model has been proposed which not only determines the percolation threshold of a network, but also describes the distribution of conductivities that arise from the variety of nanotube bundles and junctions.

Films have also been incorporated into functioning photovoltaic and LED devices, proving the effectiveness of these networks as transparent electrodes. This demonstrates the necessity of understanding network behavior and of developing methods for producing films for technological application.

Table of Contents

List of Figures

List of Tables

List of Acronyms

AFM	atomic force microscope
Alq3	aluminum tris(8-hydroxyquinoline)
BWF	Breit-Wigner Fano
CE	Crown Ether
CSA	chlorosulfonic acid
DMF	dimethylformamide
DOS	density of states
EL	electroluminescence
FOM	figure of merit
HFI	hydrofluoroisopropanol
ITO	indium tin oxide
LCAO	linear combination of atomic orbitals
LED	light emitting diode
MEHPPV	poly[2-methoxy-5-(2'-ethyl-hexyloxy)-1,4-phenylene vinylene]
ODCB	ortho-dichlorobenzene
OLED	organic light emitting diode
OPV	organic photovoltaic
PDMS	polydimethylsiloxane
PEDOT	poly(3,4-ethylenedioxythiophene)
PEDOT:PSS	poly(3,4-ethylenedioxythiophene) poly(styrenesulfonate)
PFO	poly(9,9-dioctylfuorene)
PV	photovoltaic
RBM	radial breathing mode
SEM	scanning electron microscope
SC	sodium cholate
SDBS	sodium dodecyl benzene sulfate
SDS	sodium dodecyl sulfate
SWNT	single wall nanotube
TCNQ	tetracyanoquinodimethane
TEM	transmission electron microscope
TGA	thermogravitational analysis

CHAPTER 1 INTRODUCTION

1.1 Theoretical Background

Carbon Nanotubes have been studied extensively since their discovery because of their behavior as a one dimensional quantum system, the fact that they occur as both metallic and semiconducting forms, and their potential application in composite materials and electronic devices. A single walled carbon nanotube (SWNT) is the hexagonal lattice of a graphite sheet rolled up into a cylinder, end-capped with buckyballs [1]. The lattice can be rolled in different directions to make tubes of different radii and chirality, and the geometry of the rolling can be characterized by a single vector,

$$\vec{C}_h = n\vec{a}_1 + m\vec{a}_2 \tag{1.1}$$

the chiral, or roll-up, vector (Figure 1). The translational symmetry can be described by a vector,

$$\vec{T} = t_1\vec{a}_1 + t_2\vec{a}_2 \tag{1.2}$$

perpendicular to $\vec{C}_h$, which gives the distance that the tube repeats itself along its length. From hexagonal symmetry,

$$t_1 = 2m + n \tag{1.3}$$

$$t_2 = 2n + m \tag{1.4}$$

Nanotubes are chiral unless $m=0$ (zigzag) or $m=n$ (armchair) [2]. The electronic properties of the resulting nanotube can be calculated by a LCAO approximation, using $\vec{C}_h$ as the boundary condition. This does not take into account the overlap of π orbitals due to curvature of the nanotube, and is therefore more accurate for larger diameter nanotubes.

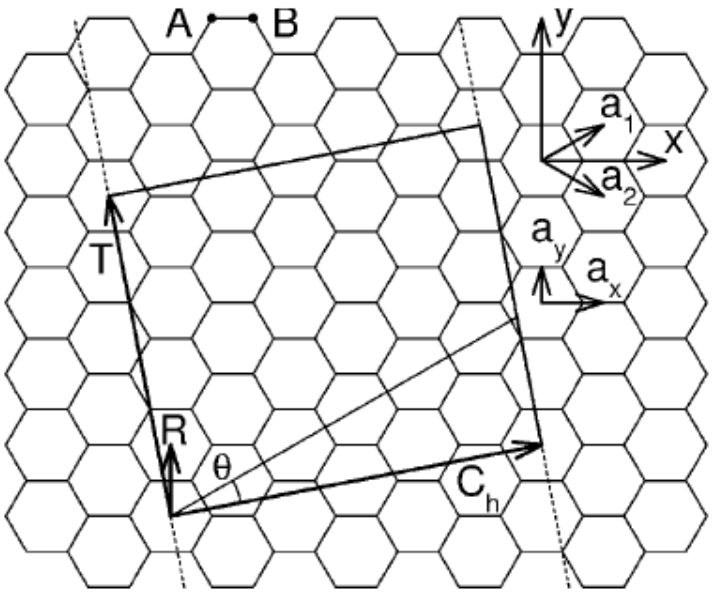

Figure 1 [2] The hexagonal lattice shown will be rolled into a chiral nanotube with a circumference $\vec{C}_h$. The lattice repeats itself along its length every $\vec{T}$.

The method of arriving at the electronic structure of nanotubes is the zone-folding scheme [2]. The basis of the zone folding scheme is that a 1D DOS can be constructed from a 2D DOS by specially selected lines which cut into the 2D surface. A reciprocal space can be constructed from the real lattice, described by vectors $\vec{b}_1$ and $\vec{b}_2$, such that

$$\vec{a}_i \cdot \vec{b}_j = 2\pi\delta_{ij} \tag{1.5}$$

The reciprocal space vectors are then

$$\vec{K}_1 = -(\vec{t}_2\vec{b}_1 - \vec{t}_1\vec{b}_2)/N \tag{1.6}$$

$$\vec{K}_2 = (m\vec{b}_1 - n\vec{b}_2)/N \tag{1.7}$$

The vector $\vec{K}_1$ points along the direction of the rolling of the reciprocal space. At each multiple of $\vec{K}_1$ lies a cutting line, with *N* cutting lines along the tube circumference in reciprocal space. The area of the first Brillouin zone is then given by

$$N\vec{K}_1 \times N\vec{K}_2 = \left|\vec{b}_1 \times \vec{b}_2\right| \tag{1.8}$$

The 2D dispersion relation is given by the cone from the K-point (Figure 2), and where intersects the cone yields the DOS of the nanotube. From this illustration, it is clear that the band gap is zero only if the cut lines intersect the K-point of the lattice.

From this model, tubes with *(n-m)/3=integer* are metallic, and all others are semiconducting. From this result, 1/3 of all nanotubes should be metallic, and the other 2/3 semiconducting. The one-dimensional nature of the tubes gives rise to van Hove singularities in the density of states, a defining feature characteristic of 1-D objects [3, 4].

1.2 Carbon Nanotubes as Transparent Conducting Films

Due to their high aspect ratio, strength, and electronic properties, carbon nanotubes have been investigated for use as transistors [5-7], as light emitting diodes [8, 9], and as solar cells [10, 11]. Transparent conductive coatings are a necessary part of many technological devices. The above devices are among the many technologies that use these thin coatings [12]. Each has a specific range of transparency and resistance that must be met for its application, and nanotubes are well on their way to meeting this goal (Figure 3). The current standard for coatings is Indium Tin Oxide. ITO can be manufactured well within the technologically necessary range, down to 10Ω/Square at over 80%T. However, ITO must be deposited at high temperatures and cannot withstand repeated bending once deposited [12]. Also ITO is becoming increasingly expensive, due to limited supply, as it is a by-product of mining, and from increasing demand from industrial use. An ideal replacement material would have the same conductive properties at high

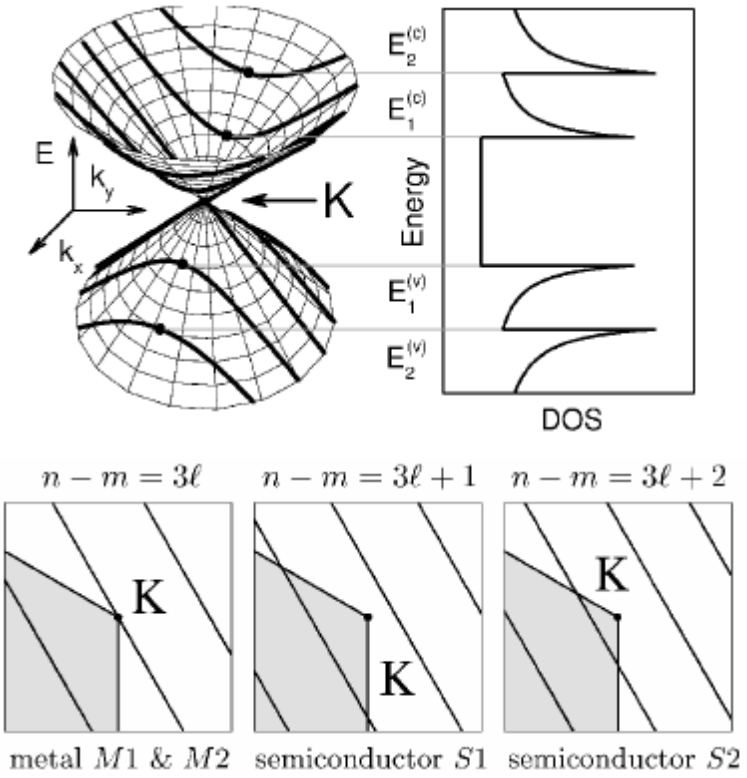

Figure 2 [2] The cutting lines, determined by the tube wrapping direction, at each K_1, intersect the cone and give rise to the characteristic DOS of a 1D object. There is a band gap unless the cut line passes through the K-point. The DOS shown is metallic.

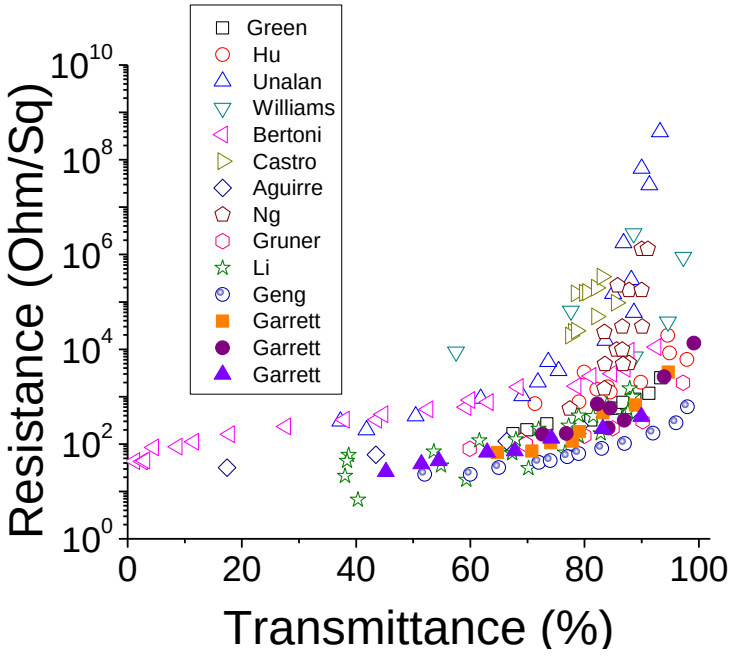

Figure 3 Nanotube coatings achieved by various groups are shown [9, 13-22]. For use in a flat panel display, a coating must be at least 80%T and under 200Ω/Sq. For a touch screen monitor the coating must be under 1000Ω/Sq and over 90%T, and an organic LED must have at least 90%T at under 10Ω/Sq.

transparencies, would be flexible, and could be deposited at room temperature on a wide variety of substrates [12].

Carbon nanotubes are well on their way to meeting this goal [8]. Nanotubes have generated much interest as a replacement for ITO as they can be deposited in thin layers on a wide range of substrates and maintain their conductive properties under flexing [13-15]. Also while ITO has become more expensive, Nanotubes have dropped in price as methods of manufacture and purification have improved. However, to meet the appropriate conductivity requirements at the necessary transmittance, perfection of the networks that comprise the nanotube films is necessary. Also, doping of nanotubes has been shown to alter their conductivity, and as a result,

altering the networks by the appropriate chemical additives would be expected to lower the resistance of these films [13-15].

Nanotube films have been produced by many different methods, among them spray application techniques [7, 14, 19], evaporation [23], PDMS stamping [21-23], and Langmuir–Blodgett deposition [17-19]. We employ a method developed by Andrew Rinzler's group at the University of Florida [24]. The method involves vacuum filtering a solution of nanotubes through a 0.1μm pore size cellulose nitrate filter, which leaves a uniform film of nanotubes on the filter paper, allowing only the solvent or surfactant to pass through. The excess surfactant can be washed away from the nanotubes by simply pumping deionized water through the filtration apparatus. The complete nanotube film-on-filter can then be inverted tube side down on a

substrate, and the cellulose nitrate filter dissolved in acetone and methanol, leaving only a thin layer of nanotubes.

This is a superior method of creating thin films of nanotubes, as there are no nanotubes wasted, as found in methods such as spray deposition or spin coating, and it allows very precise control over the number of nanotubes applied over a specific area, creating a film that it always optically uniform. It is even possible, by a variation of this method, to make films that are free standing and need no substrate for adhesion [25]. By adhering the films to glass microscope slides, we are able to perform absorbance spectroscopy, as well as Raman spectroscopy, four-point-probe resistance measurements, impedance spectroscopy, SEM and AFM imaging, as well as optical microscopy, providing a wealth of information about our samples.

1.3 Individual SWNT

Our films are composed of both semiconducting and metallic nanotubes in a random arrangement, where electrical transport occurs not only through each type of tube, but through junctions between tubes as well. In order to understand and characterize transport behavior through these networks, one must first understand the conductive properties of not only the nanotubes themselves, but junctions between nanotubes as well.

A detailed study of nanotube resistances at junctions by Buldum[26] reveals that the resistances can vary anywhere from a few hundred kΩ to several MΩ, depending on the nature of the contact. The inter-tube resistance for crossing junctions is strongly dependent on the lattice alignment of the two nanotubes. When atoms in the lattice align “in registry” in the same

manner that they would between two layers of a graphene sheet, the resistance for crossing of two (10,10) nanotubes was found to be 682kΩ, but when the lattices are out of registry, the resistance was found to be 3.21MΩ [26]. The same study showed that the resistance between nanotubes in parallel alignment depends on the length of contact between nanotubes, with the longer contact length yielding lower resistance. This is also dependent on the nanotube lattices being in registry with one another, again with in-registry tubes yielding lower resistances. The transport waves reflecting between tube ends interfere, producing resonances, and the number of resonances at the overlap increase with the size of the overlap. These parallel-aligned tubes also exhibit negative differential resistance behavior, due to the quantum interference at the junctions. Interestingly, smaller diameter tubes, despite having smaller contact areas, yield lower resistances at crossing junctions than higher diameter tubes. This is due to the conducting states being quantitized along the tube diameter. The amount of the transport wave through the junction in proportion to tube diameter is larger for smaller tubes, resulting in lower resistance. Between two contacting nanotubes of given diameter, rotating the nanotubes relative to one another and therefore increasing the contact area, does decrease resistance. They have also found that application of force to the junctions decreases resistance, with a larger drop for in-registry tubes than out-of-registry tubes.

The internal resistance of a single-wall carbon nanotubes have been measured to be as low as 15kΩ for metallic tubes, to as high as a few MΩ for semiconducting tubes, with most semiconducting tubes in the range from 160-500kΩ, and metallic tubes generally below 40kΩ [27-29]. The lowest of the measured values in these studies are very close to the quantum resistance, $h/2e^2$=12.6kΩ, the lower limit of 1-D resistance. An experimental study has shown

the junction resistance between two metallic nanotubes to be around 200-300kΩ, with the junctions between two semiconducting nanotubes to be in the 400kΩ-2MΩ range [30]. The contacts between metallic and semiconducting tubes yield a Schottky barrier height between 200-300 meV, which is approximately half the band gap of a semiconducting nanotube. Given that 1/3 of nanotubes are metallic and 2/3 semiconducting, a random arrangement of nanotubes would have a distribution of junctions with 4/9 semiconducting-semiconducting, 4/9 metal-semiconducting, and the remaining 1/9 metal-metal.

It is, of course, impossible to relate the behavior of networks consisting of millions of SWNT to properties of individual SWNT in the network. However, knowing the range of conductances expected from different types of nanotubes and junctions is important to understanding which aspects of the network relate to overall resistance. Understanding the makeup of a SWNT sample in terms of relative amounts of semiconducting and metallic nanotubes is especially important for determining the effects of dopants on the network.

1.4 Bulk networks

The resistance-to-transmittance ratio of a given nanotube network changes based on the thickness (SWNT per square area) of the network. To find the optimum resistance to transmittance ratio for a nanotube film, we are interested in the percolation threshold of the nanotube network. Percolation occurs when the number of nanotubes in the film is large enough to form a conducting path through the film, characterized by a sudden drop in sheet resistance at a critical loading, at which point the resistance changes very little upon addition of more nanotubes. The percolation threshold is therefore the lower limit for conductivity of a nanotube

network. An understanding of percolation behavior will not only give us the limit of transparency for which a network will never be conductive, but will allow for a broader understanding of transport, and for predictions of conductivity for networks of a wide range of thicknesses.

From percolation theory, we expect that the loading in which the film becomes conductive is dependent on the length and the orientation of the SWNTs (or SWNT bundles.) The network can be modeled as a simple arrangement of long, straight conducting sticks. When the average length of the nanotube equals the average spacing between nanotubes, a percolated network forms. At random orientation, longer nanotubes will percolate at lower loadings than shorter ones [31].

Since metallic tubes and metal-metal junctions have higher conductivity than other types, one would expect that separation of metallic tubes prior to film deposition would create a more conductive network. This has been done, and an improvement from 3000 to 900 Ohm/Sq at 90%T was demonstrated [13]. However, as shown in Figure 3, these monodispersed metallic films did not achieve conductivity that was higher than has been achieved with mixtures of semiconducting and metallic nanotubes. This demonstrates the importance of considering the effects of bundling and dispersion when designing nanotube films. The high aspect ratio of large bundles can make a more conductive film than monodispersed metallic SWNT, even if those bundles consist of mostly semiconducting SWNT. Also, semiconducting SWNT with a higher diameter tend to have smaller band gaps, and form larger contact area at junctions, and should result in a network with higher conductivity [32].

It has recently been shown, by varying the relative fraction of metallic and semiconducting SWNT in films, that all-metallic films are not optimum [33]. In that study, films consisting of approximately 20% metallic nanotubes had the highest conductivity. Not surprisingly, doping had a greater effect on the resistance of the semiconducting enriched films than on the metallic enriched films. With $SOCl_2$ doping, the resistance was only 180 Ohm/Sq at 76%T, and 920 Ohm/Sq at 80%T for films with 6% and 94% metallic content, respectively. It should be noted that these 94% metallic films were a 10% lower transmittance at the same conductivity than the all-metallic films in reference [13].

Some groups have attributed the formation of large bundles to increased film conductivity [14, 34], while others have attributed individual tubes and small bundles to increased conductivity [35, 36]. Separation of different size bundles, as well as separating single tubes of different length and diameter distributions for deposition as films would yield the best insight into this problem. Due to the impossible nature of making extensive networks with bundles of only a single size, we have taken the approach of using different methods of dispersion and purification, which yields samples with different degrees of bundling, and different amounts of non-nanotube content. We were than able to change the conductivity of the bundles and junctions by doping the films. This allows us to determine the effects of dopants on the films, independent of other aspects of network formation and morphology.

1.5 Dispersion and purity

Choice of a nanotube sample is the first step in forming a nanotube film. Each method of growing nanotubes yields a different range of diameters, lengths, and defects; as well as turning a different amount of starting material into nanotubes. Once produced, the sample can be purified, removing metal catalyst and amorphous carbon, further changing the quality of the available material. The quality of the material obviously will alter the electrical and optical properties of the final film. It is expected that starting with material that contains a high percentage of nanotubes compared to the amount of carbonaceous impurities and catalyst will result in films with lower resistance. It is also expected that starting with a sample of nanotubes that have few defects will result in higher quality films.

Before making a film, the nanotubes must be dispersed in solution. The solvents dimethylformamide (DMF), toluene, xylene, and ortho-dichlorobenzene (ODCB) have been used in our group to disperse carbon nanotubes with promising results, as have the surfactants sodium dodecyl sulfate (SDS), sodium cholate (SC), and Triton X-100.

We have carefully monitored the sonication process of ORNL laser-grown and purified nanotubes in several dispersants, making films from the solution after different amounts of sonication time, recording the visible-spectrum transmittance and resistance of each resultant film. We have used our data from Raman spectroscopy, absorbance spectroscopy, and SEM to determine which factors contribute most to the change in network properties of these films. We have also developed a process of purification which is specifically applicable to SWNT

networks, in addition to making networks of films with SWNT that have been purified by other well-known procedures.

1.6 Doping

Nanotubes that have been doped in solution have been shown to have higher conductivity than undoped nanotubes [24, 37]. Similarly, nanotube films can be doped by exposure to the chemical dopant. We have doped our films with HNO_3 and $SOCl_2$, which have both been shown to increase conductivity by hole doping [24, 34, 37, 38]. The use of ortho-dichlorobenzene as a dopant has been studied as well.

It was found that the films can be doped simply by immersing them in the dopant of choice, or by exposing them to the vapors of the dopant. Dopants applied in this way can change conductivity by either increasing the conductivity of the nanotubes themselves, increasing the conductivity within bundles, or by increasing the conductivity at junctions between bundles and individual nanotubes. Since the resistance of a junction between two nanotubes is greater than the resistance of a semiconducting nanotube, it was suspected that dopants that decrease resistance at junctions may be more effective than those that decrease the resistance of the nanotube itself.

One paper which reported on $SOCl_2$ doping of tubes while in solution attributed the drop in resistance of the resulting buckypaper to the formation of bundles [34], but doping an already created film cannot allow bundles to form, so there must be another mechanism at play in our method. The advantage to doping the tubes once they are affixed to a substrate, is that it is

possible to separate the effects of the dopants from the effects of network geometry, as the dopants can only alter conductivities of tubes or junctions. Doping before or during dispersion, before being made into a film, could actually change the number of connections or layout of the bundles, therefore not allowing the study of doping effects independent of film geometry.

1.7 Summary of goals

To work towards an optimization of the transmittance and conductance of SWNT networks, it is first necessary to understand of dispersion, as dispersion is what determines film morphology. Next, it is necessary to understand purity, as non-nanotube carbon and SWNT defects all affect film quality. Not only must the purity of the starting material be known, but most importantly the purity of the resultant films must be monitored also, as the dispersion process can change the final purity of the film.

Once these processes are understood, networks of varying densities can be constructed, and their properties understood, not only as individual networks, but as a function of varying purities and dispersants as well. Once understood, these networks can be doped chemically, not only further improving their conductivity but also shedding further insight into the working of the networks. This approach has allowed the contribution of factors such as degree of dispersion, sample purity, film thickness, and amount of doping to be studied separately, determining the contribution of each to network quality.

CHAPTER 2 EXPERIMENTAL TECHNIQUES

2.1 Resistance Measurements

The accurate assessment of sheet resistance is of fundamental importance to making conductive films. Sheet resistance (Ohm/Square) is the two-dimensional equivalent of the familiar 1-D linear resistivity (Ohm/cm) and 3-D bulk resistivity (Ohm-cm). In reality, we are measuring sheet resistance, with resistivity being only a property of a bulk 3-D substance. An essentially 1-D object, such as a wire, has a visualized resistivity that is calculated by dividing its measured resistance by its length, even though the real resistivity is actually a property of the bulk material. Similarly, one can consider our measurements to be a measurement of sheet resistivity, a property of a specific film, a quantity independent of its geometry. This concept of 2-D resistivity is especially useful for nanotube films, with the tubes being randomly oriented, and therefore isotropic, in two dimensions, but anisotropic in the third dimension, with no tubes aligned normal to the film surface.

Two-dimensional resistance and resistivity is unique in that the dimensional units of the object are irrelevant when relating resistance to resistivity. In one-dimension, if one were to measure the resistance of two otherwise identical wires with different lengths, the resistances would increase proportionally with length (see Figure 4).

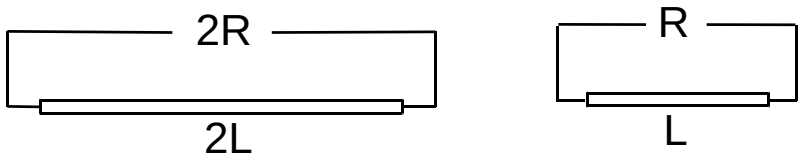

Figure 4 For a 1-D object of given resistivity, the resistance is proportional to length.

Similarly, measuring resistances between opposite walls of rectangles with different dimensions, increasing sample size perpendicular to the electrode length will increase resistance proportionally. By increasing sample size along the electrode length, the resistance drops proportionally. An increase in sample dimensions in all directions will therefore have no effect on the measured resistance (see Figure 5). That is, the sheet resistance, as measured across opposite sides of the square, is independent of the dimension of the square, and a measurement of sheet resistance is also a measurement of sheet resistivity. The units for sheet resistance are Ohm/Square.

This does not hold true for resistance measured across opposite sides of a cube, given the familiar relation $R = \rho L / A$, with ρ the bulk resistivity of the cube, A the area of the faces which are being contacted for the resistance measurement, and L the distance between faces (see Figure 6). If one wishes to acquire a bulk resistivity from a sheet resistance measurement, sheet resistance can be related to bulk resistivity by simply multiplying by the sample thickness.

The most direct measurement of sheet resistance would be to make electrodes onto two sides of a film and measure the resistance of the square area between the electrodes, the measured value being the sheet resistance. However, this would require extensive and irreversible preparation of each sample before any measurement could be made. Instead we have employed two different techniques to determine the conductivity of our samples, an AC and a DC technique, which allows for cross-checking of accuracy between the DC measurements and the low-frequency AC measurements. Both methods consist of point-probes placed in contact with the film surface, and require no modification of the film.

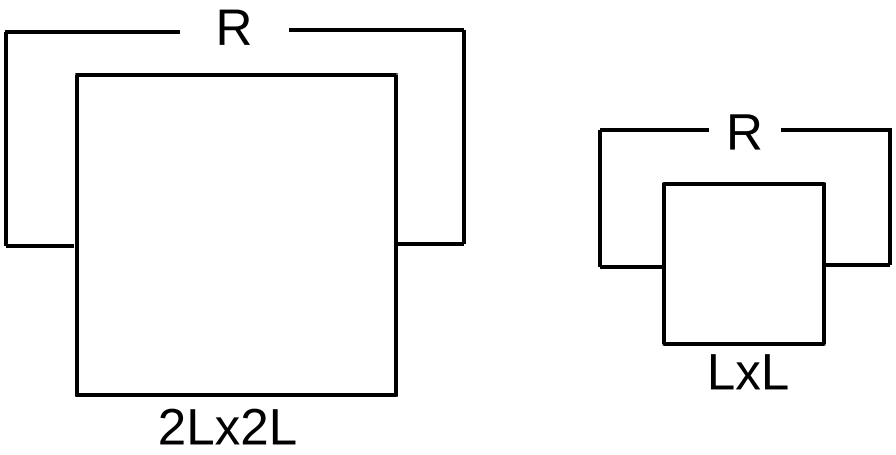

Figure 5 The resistance measurement of a 2-D object depends only upon sample resistivity, not on sample dimensions.

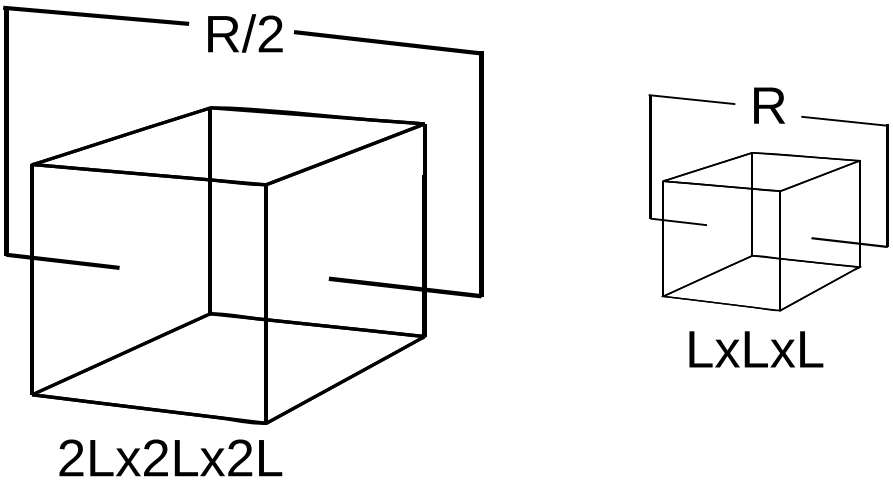

Figure 6 An increase in dimensions of a 3-D sample in all directions causes a proportional drop in resistance.

The four-probe technique[39] has been employed to determine the sheet resistance of our samples, as it can be done quickly, and does not require any further preparation or alteration of the sample. It allows the sheet resistance to be measured independent of any other measurements on the sample, such as thickness, and therefore the same setup can be used on samples of widely varying thicknesses and surface areas. The four probe method works by contacting four equally-spaced point electrodes onto the sample surface. Current is passed through the outer two electrodes, and the voltage is measured across the inner two electrodes, as in Figure 7. This method has the added value that any contact resistance between the probe tip and the sample is eliminated by nature of the four-probe system. Only a simple conversion factor is needed to arrive at the sheet resistance from the measured resistance in a four-probe setup. This factor depends on sample geometry, but values for many different geometries are very well tabulated [40, 41].

The elimination of contact resistance in a four-probe setup is easily seen by viewing the system as a series of floating resistances between the current source and sink[42]. In Figure 7, the mutual resistance of point 2 with electrodes 1 and 4 is given by

$$R_M = R_{21} - R_{24} \tag{2.1}$$

For both points 2 and 3, the mutual resistance is then

$$R_M = R_{21} - R_{24} - R_{31} + R_{34} \tag{2.2}$$

The actual measurement of each resistance would include not only the resistance of the DUT but the contact resistance as well:

$$R_{ab} = R_{sample-ab} + R_{contact-a} + R_{contact-b} \tag{2.3}$$

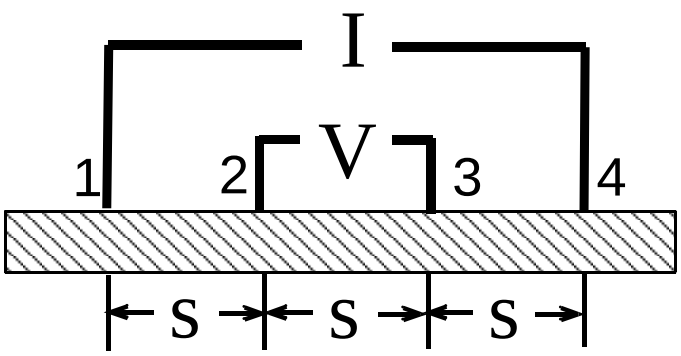

Figure 7 Setup for four-probe resistance measurements. Current is sourced from probes 1 and 4, voltage is measured between probes 2 and 3

In equation 2.3 the sample resistance measured between two contact positions *ab*, $R_{sample-ab}$, depends on the spacing between those two electrodes. If the resistance of each contact is the same, for all *a* and *b*, as is the case with our experimental setup, it is quickly noted that the contact resistance will cancel out of equation 2.2, leaving only the different resistances contributed to by the sample.

Four-probe DC measurements were carried out with a Keithley 6430 source-ohm-meter. The currents required to perform these measurements are very small, from a milliamp to a few picoamps, with the source-ohm-meter automatically choosing progressively smaller currents for increasingly higher resistances, so no heating of the film will occur during the measurement process. Using power output from ohms law, and a 700 J/(kg*K) heat capacity for carbon, the instrument settings give, at most, a 3C temperature increase over a 10s measurement period. This does not include the obvious loss of heat from the film to the substrate. Therefore no discrepancies in measured sheet resistance arise from temperature variations in the films while measurements are ongoing.

AC impedance measurements were carried out with a Zahner Thales impedance spectroscopy system in a two-probe configuration in addition to the four-probe configuration. At sufficiently low frequency, AC measurements are expected to agree with DC measurements, and a relation between two and four probe measurements is therefore necessary. Two-probe and four-probe measurements can be related to one another in two different ways.

The floating potential at any point away from a current point source on a conductive sheet is given by Uhlir[40]

$$V_{2\,probe} = \frac{\rho I}{2\pi} \ln r \tag{2.4}$$

If we wish to measure sheet resistance of a sample using two point-electrodes with spacing *s*, then from ohms law the measured resistance is

$$R(s)_{2\,probe} = \frac{\rho}{2\pi} \ln s \tag{2.5}$$

One can note that subtracting *R(2s)* from *R(s)* gives the relation

$$R(2s)_{2\,probe} - R(s)_{2\,probe} = \frac{\rho}{2\pi} \ln 2 \tag{2.6}$$

This is half the four-probe resistance, as given by Smits[41]

$$R(s)_{4\,probe} = \frac{\rho}{\pi} \ln 2 \tag{2.7}$$

Therefore one can measure the two probe resistance at 1s spacing and then again at 2s spacing, and readily arrive at the measured four-probe resistance. The advantage of this method is that

the contact resistance is automatically eliminated upon subtraction. The disadvantage is, of course, that additional measurements are required.

The second method consists of using a conversion factor between the two and four probe measurements. It can be shown[39-41] that the floating potentials for a four-probe and two-probe configuration are given by

$$V_{4\,probe} = \frac{\rho I}{2\pi} \ln \frac{r_2}{r_1} \tag{2.8}$$

$$V_{2\,probe} = \frac{\rho I}{2\pi} \ln r \tag{2.9}$$

Where r_i is the distance from the current source for which the potential is measured. Assuming that the two configurations differ by some multiplicative expression A, one obtains

$$V_{4\,probe} = A V_{2\,probe} \tag{2.10}$$

$$\frac{\rho I}{2\pi} \ln 2 = A \frac{\rho I}{2\pi} \ln r \tag{2.11}$$

Where we have taken $r_2 = 2r_1$, which is the condition for a standard 4-probe configuration with the probes equally spaced. We see that for constant tip spacing, s, the factor of conversion, A, between four-probe and two-probe measurements is constant and independent of source current or sample resistivity.

$$A = \frac{\ln 2}{\ln s} \tag{2.12}$$

By calculating this constant for the probe station setup, it is possible to compare two and four probe measurements for all of the samples. While this calculation does not mathematically eliminate the contact resistance, a constant contact resistance would appear into an

experimentally determined conversion constant, still allowing an experimental comparison between measurements. This has been done in chapter 5.1.

2.2 Spectrophotometry

Since transparent films are of interest in this work, absorbance spectroscopy is obviously vital for determining how much light in the visible spectrum is able to pass through the film. In addition, the NIR spectrum shows the electronic transitions within semiconducting and metallic SWNT and gives the diameter distribution of the SWNT. It can be used to determine the relative amounts of carbonaceous impurities within the samples.

The absorbance spectrum of any nanotube sample consists of an essentially featureless curve, which is due to the π-plasmon of both the nanotubes and of the amorphous carbon in the sample. Superimposed upon this curve are three distinct peaks, the first of which is due to the transition of the metallic nanotubes, and the other two are from the first two transitions of semiconducting nanotubes (Figure 8). These peaks appear only for single-walled nanotubes, and other forms of carbon have no such transitions.

The assignment of absorbance spectra peaks to nanotubes of certain diameters and chiralities was first done by Kataura [43]. Kataura calculated the energy gaps for a large number of nanotubes and plotted them as a function of diameter (Figure 9).

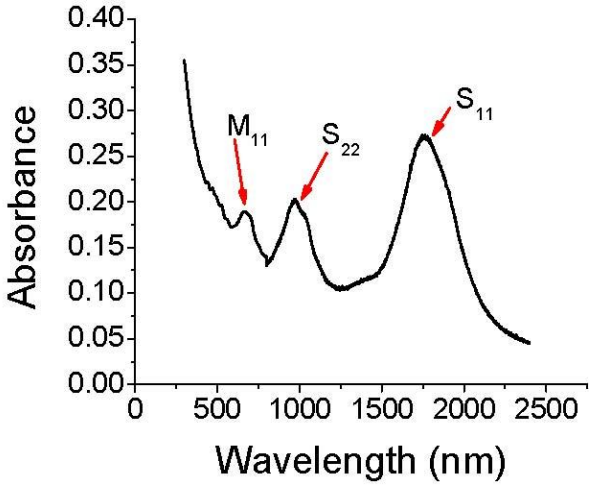

Figure 8 The absorbance spectrum of a nanotube thin film, showing the first two semiconducting transitions (S_{11} and S_{22}) and the first metallic transition (M_{11}). The exact position of the peaks and the width depends on the diameter distribution of the sample.

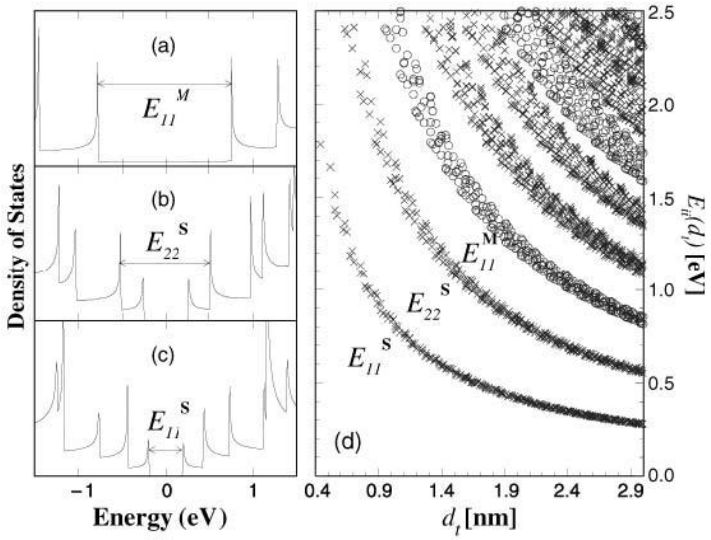

Figure 9 [44] Kataura plot showing transition energies as a function of tube diameter. Only the first three transition peaks appear on the absorbance spectrum, as the other transitions have a large amount of overlap, are unnoticeable from the large high energy π-plasmon peak, are indistinguishable from the near-total substrate absorbance, or occur at energies outside the range of a standard spectrophotometer.

Given knowledge of the approximate diameter range of a given sample of nanotubes (from TEM), he was able to match the energies at which absorption occurred to the tube diameters on his plot. From this information he was also able to show that the first two peaks in the absorption spectra were from semiconducting tubes and the third from metallic tubes.

These calculations, like most calculations concerning Raman or absorbance spectroscopy in nanotubes, have been done with the assumption that all optical behavior can be accounted for as transitions between van Hove singularities in the density of states. In conventional bulk semiconductors the electron-hole binding energies are small enough in comparison to the band gap to be neglected, and are washed out thermally at room temperature [45]. This is not true for carbon nanotubes, where the exciton energy is ten times higher and plays an important role in interpreting experimental data. Calculations for semiconducting SWNT of small diameter also show that the contribution of excitons dominate the electronic response [46]. Upon including the electron-hole interactions, the calculated absorption peaks for a given tube will shift noticeably, demonstrating the need to include quasiparticle interactions when relating diameter and chirality distributions to absorption spectra [46].

2.3 Spectrophotometric Purity Assessment

The intensities of each transition peak in the absorbance spectrum relative to the intensity of the π-plasmon signal should depend on the relative amounts of nanotubes and amorphous carbon in the sample (Figure 10). Unfortunately, the plasmon signal of the nanotubes cannot currently be separated from the plasmon signal of the amorphous carbon, so a measure of absolute purity is not attainable. The procedure outlined by Itkis[38] in Figure 11 is to draw a baseline at the edge

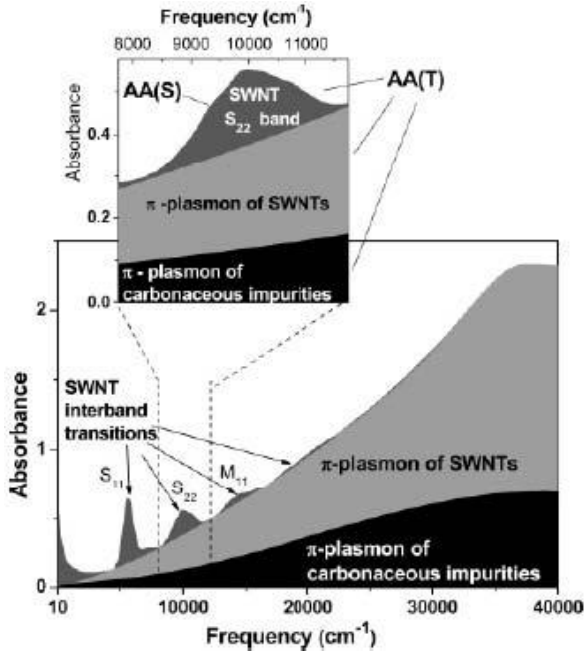

Figure 10 [47] The absorbance spectrum is composed of the π-plasmon of the nanotubes and of the amorphous carbon, in addition to the peaks from VHS transitions.

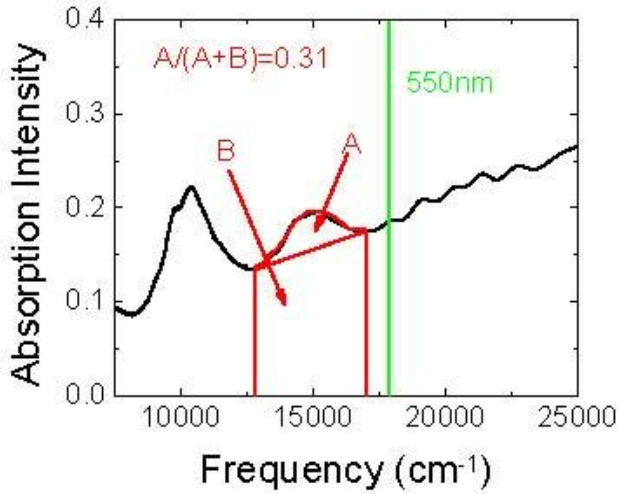

Figure 11 The S_{22} transition is used to determine carbon impurities, by dividing peak area (A) by the sum of the peak area and plasmon area (B) The center of the visible spectrum is shown as well.

of the S_{22} band and find the area under only the S_{22} peak (between the peak and the baseline), comparing it to the total area under the peak (between the peak and the x-axis.) The ratio of the area under only the peak to the total area under the peak can be used to compare purities between samples.

The S_{22} peak was originally chosen to compare purities, since the solvent used to disperse tubes, DMF, has very little absorbance at those wavelengths. The S_{22} band is also more prominent than the M_{11} band, and is less affected by doping than the S_{11} band. To measure purity by absorbance, the samples must be prepared in the same way to ensure reproducibility in comparing batches of nanotubes. The original paper that introduced this method described evaluating the samples by dispersing tubes in DMF by sonication, and reported discrepancies and difficulties when attempting to evaluate absorbance purity between solution phase and solid phase SWNT samples [38]. We are interested in the absorbance of nanotubes in thin layers, in different stages of bundling, often with aggregates in the sample. It is not yet known how well this assessment, when made on thin films, can be compared to solution-phase tubes, due to nanotube-solvent interactions or possible differences in light scattering between dispersed SWNT and SWNT films.

A similar method for the determination of purity using absorbance spectroscopy has been developed by Landi.[48] In this method, instead of a linear baseline subtraction, the π-plasmon contribution is determined by a Lorentzian curve fit, as in Figure 12. To demonstrate this effectiveness, a subtraction of the area just below the peak, as determined by a line connecting the edges of the base of the peak, was compared to a modified baseline drawn arbitrarily below

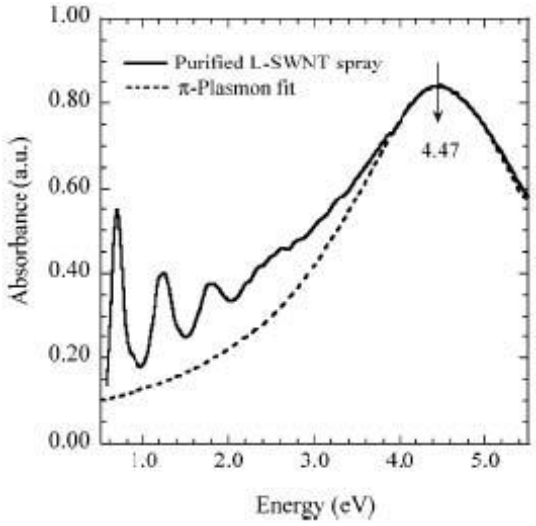

Figure 12 The π-plasmon, as modeled by Landi[48]. The plasmon peak is not visible in our absorbance spectra, as the glass substrate allows for almost no transmission at those wavelengths.

the peak (Figure 13). By adding carbon impurities to a "pure" sample, Landi was able to show that for a properly chosen line, the assessed purity is proportional to the true purity. The curve from the modeled Lorentzian fits this trend and lies at the position of that arbitrary line. For example, if an assessment of purity by the Itkis method yields a value of 0.14, and another sample has a value of 0.28, the second sample, while purer, does not have twice the purity as the first. However, if two samples evaluated by the method of Landi gave the same two values, the second would be twice as pure as the first; true relative purity (Figure 13).

We have used the method of Itkis to determine purity of our SWNT films, due to its repeatability and ease of application between samples. It has been found that valid purity assessments are attainable with this simpler method, and its application allows comparison to other work on SWNT purity, as it is the most popular purity assessment method using optical absorbance of SWNT [49].

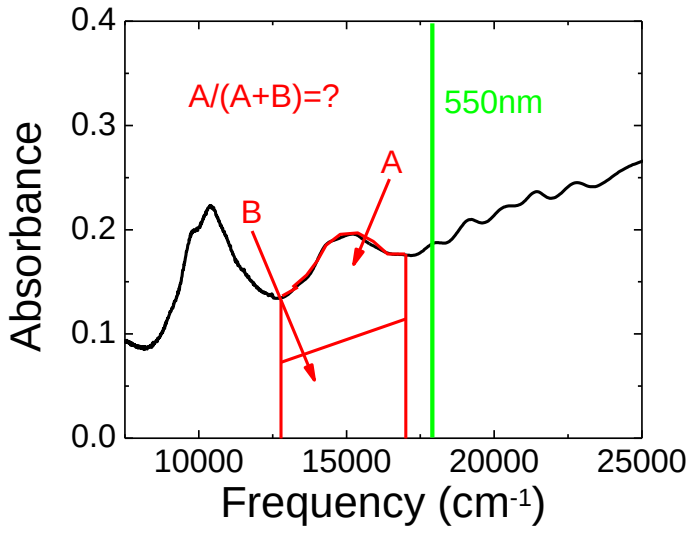

Figure 13 The assessment of Landi differs from that of Itkis as the position of the baseline falls at the position of the π-plasmon fit instead of at the base of the peak edge. The left and right limits for each assessment are the same.

2.4 Raman Spectroscopy

The most sensitive tool available to determine electronic and vibronic makeup of nanotube samples is Raman Spectroscopy. Raman scattering occurs when an incident photon excites a vibrational state, bringing it either from its ground state to an excited state (Stokes scattering), emitting a phonon, or from an excited state to its ground state (antiStokes scattering), absorbing a phonon, illustrated in Figure 14.

If the excited state and ground state are both real states, then a resonance occurs. In carbon materials, not only can the incoming photon (laser energy) be tuned to create a resonant condition, but the phonons from the Raman process also excite real vibrational states, causing a double resonant process. This double resonance is dominant for carbon nanotubes, although rare

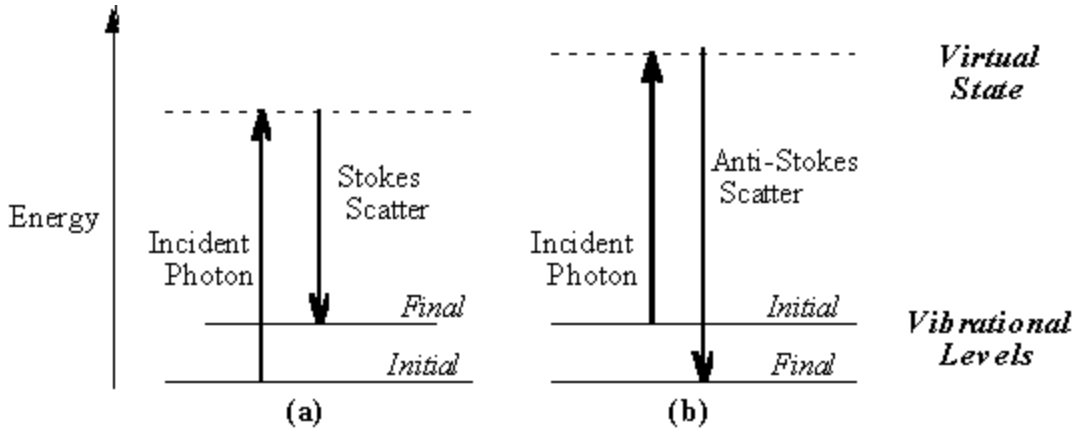

Figure 14 Stokes (a) and anti-Stokes (b) Raman scattering. Resonance occurs when the excited state (dashed line) is a real state instead of a virtual state [51].

for bulk solids of other materials [50]. There are two types of resonance that can occur: incoming and outgoing. Incoming resonance occurs when the laser energy matches the transition energy between two real states; $E_{laser} = E_e - E_i$. Outgoing resonance occurs when the phonon matches the transition energy between real states, $E_{laser} \pm E_{phonon} = E_f$. If any state is a virtual state, then the incoming resonance condition would not be met [52]. Raman transitions between virtual states are the most commonly occurring case for most materials, but not for carbon nanotubes. When both incoming and outgoing resonance occur, the material is said to be double resonant. This double resonance is rare among bulk solids, but is the dominant Raman condition for carbon nanotubes [50]. SWNT also have a number of second order modes, which arise from either emission of two phonons from a single Raman process, or one phonon and an elastic scattering in a single Raman process. These peaks are typically broader, as the two phonons can be of different energies.

The double resonant peaks are sharper in carbon nanotubes than in graphite, as the incident and scattered photon and phonon vectors are quantitized in one dimension along the tube

circumference, whereas 2D graphite has no such restriction [53]. Therefore, a given laser energy can only excite tubes of certain chiralities, with only those tubes in resonance contribute to the spectra.

Raman spectra from a nanotube sample consists of several bands, each corresponding to a certain aspect of the nanotube. At 1500-1650cm^{-1} the most prominent peak occurs, the G band. This corresponds to the tangential mode of the hexagonal lattice, in-plane vibrations. The Radial Breathing Mode (RBM), occurring below 400cm^{-1}, arises from the out-of-plane vibrations in the direction of the nanotube radius. Its position depends on the chiral vector of the tubes (Figure 15 and Figure 16). There is also a peak between 1250 and 1450cm^{-1}, the D band, which arises from structural defects in the nanotubes, and is also contributed to by impurities in the sample. For this reason, the intensity of the D band relative to the intensity of the G band is a good indicator of SWNT defects.

Graphite has a characteristic 1582cm^{-1} Raman mode, which occurs in carbon nanotubes as well, as the "G band". Unlike graphite, it can occur anywhere between 1500 and 1650 cm^{-1} [54], and is split into several peaks. The most prominent feature, the G+ band, is from vibrations in the direction of the tube axis, with the smaller G-band feature from lattice-plane vibrations tangential to the tube, with the G- mode occurring at a lower frequency due to the curvature of the nanotube [44]. The difference between the position of the G+ and G- band can therefore provide information as to the diameter of the tubes being studied, but not as accurately as the RBM. Free electrons in metallic tubes cause the G-band to be broader than for semiconducting tubes, but can

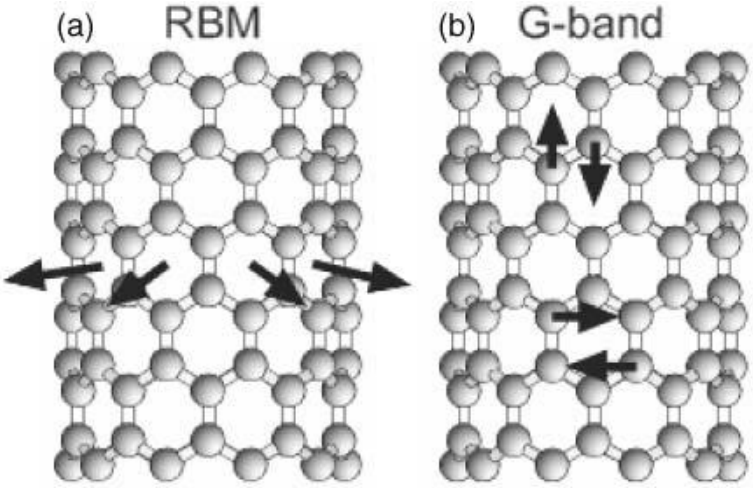

Figure 15 [44] The out-of-plane (a) and in-plane (b) vibrational modes of a nanotube. The stronger G+ band is the vibration along the tube axis, and the weaker G- band is the vibration perpendicular to the axis.

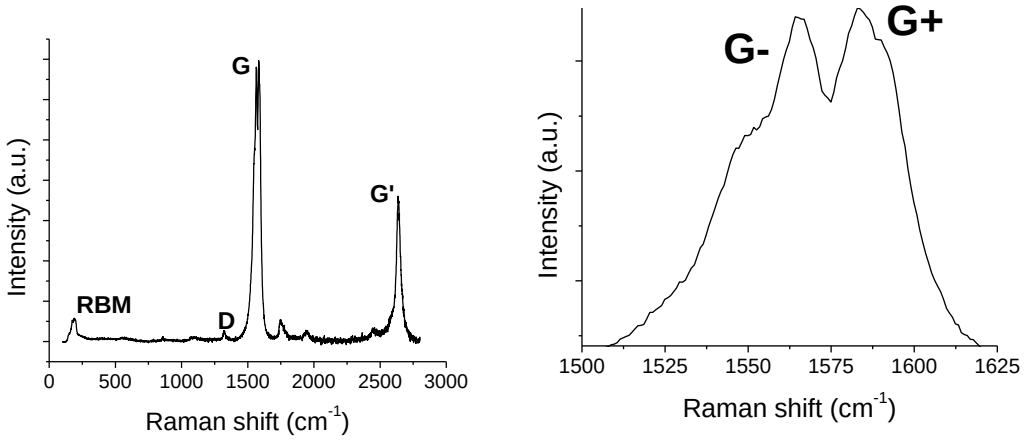

Figure 16 Raman specra of SWNT sample showing G, D, D*, and RBM. The prominent D* is the first overtone of the D band, and the peaks between the G and D* bands are other higher order features.

also indicate impurities that provide free charge. This free charge gives the metallic G band a BWF lineshape rather than the usual Lorentzian. Conversely, proton donors in solution can cause a shifting back to the Lorentzian form [55]. The shape of the G-band can then be used to distinguish metallic tubes or doping in a sample.

The Radial Breathing Mode is the Raman band that arises from the vibration of the nanotube along the direction of its radius. The peak position of the RBM is related to diameter by

$$\omega = A/d_t + B \tag{2.13}$$

where *A* and *B* are experimentally determined constants, and *d* is the diameter of the nanotube. *A* has been found to be 248 for nanotubes on oxidized Si [44], or more recently calculated to be 227 [50]. *B* accounts for interactions with other tubes in a bundle, with a surfactant, or with a substrate, but these environmental effects are very small [56], and that term is therefore usually ignored. The tube diameter is given by

$$d_t = a_0\sqrt{n^2 + nm + m^2}/\pi \tag{2.14}$$

with a_0=2.461Å, and n, m are the chiral indicies described in chapter 1.1. These calculations vary for small diameter tubes, where the tight curvature yields a different diameter than the calculated one, and that have a more prominent nonradial vibration [56]. Chiral indices can be assigned to nanotubes from the RBM position from these equations, but are sensitive to the correct values of *A* and *B*. It is best to have other information available if one wants to determine the chiral indices of a given nanotube sample. One approach to this is described by Maultzsh [56], by plotting the experimentally attained transition energies vs. the inverse RBM frequency ($d_t \propto 1/\omega_{RBM}$). This can be done without knowing the values of coefficients *A* and *B*.

Comparing this to a Kataura plot of the calculated excitonic transition energies gives the chiral indices of the experimentally observed nanotubes. Heller has shown that the RBM peak does not shift with bundling, although the intensities of fine structure features within the RBM do change [55]. However, Rao has found the opposite, with the RBM down-shifted by $10cm^{-1}$ between dispersed tubes and bundles, contradicting theoretical calculations predicting an up-shift in RBM from 6-$20cm^{-1}$ [57]. The changes from bundled tubes result from electronic mobility between tubes, perpendicular to the nanotube axis, instead of the completely 1D confinement found in isolated nanotubes.

The disorder-induced D-band, found in graphite at $1355cm^{-1}$ [58], also appears in nanotubes at a similar frequency. In isolated nanotubes, the D-band consists of a narrow peak on top of a broader one, This has been attributed to the broad peak coming from amorphous carbon in the sample, the narrow line from defects within the nanotube [44]. It has more recently been shown that the superimposed features result from the double resonant process. The low intensity band is from a double resonant process, and is broadened as there is multiple ways double resonance can occur in a tube. The higher intensity feature results from the matching of the scattered wavelength to a Van Hove Singularity energy [54]. The dependence of the D-band on nanotube diameter is not as well understood as the dependence of the RBM feature, although it has a similar dependence. The Raman-shift frequency of the D-band increases as the diameter of the tubes increases [59], in the form

$$\omega_D = \omega_0 + C / d_t \tag{2.15}$$

As the diameter of the tube increases, ω_D approaches ω_0, ω_0 being the frequency of the graphite D-band. The D-band position is determined from the double resonance effect and from the

curvature of the nanotube, with *C* being negative due to the curvature dominating the shift, unlike for the RBM, where the constant is positive, as the double resonant process dominates [60]. This was found to be a useful relationship for bundles (found by averaging the effects of many different isolated tubes, which inherently ignores any inter-tube interactions), and bulk samples. However, when probing a single band transition in isolated nanotubes at a single laser frequency, this relation does not hold. The D-band frequency decreases as the tube diameter increases, with the D-band frequency for the SWNT remaining below the D-band frequency of graphite.

As the D-band only occurs in imperfect crystals, it has been used to quantify defects and carbon impurities in nanotube samples. Since the D-band is much narrower in nanotubes than in graphitic carbon, this would suggest that one could use the width of the D-band to characterize amorphous carbon in a nanotube sample [54]. The width alone, however, is not an indicator of amorphous carbon, as one would have to take into account the dependence of band position on the diameter distribution of a given sample [54]. With the intensity of the D-band dependent on the number of defects, the ratio of G/D bands has also been used an indicator of the purity of the nanotubes in the sample [54, 61, 62]. Thus far, these defect-characterization techniques are only qualitative, and there is no broad consensus as to the best way to use the D-band to quantify defects.

2.5 Validity of Measurements

Many of the films described in this thesis are very thin and contain only very small amounts of nanotubes. It is therefore wise to question some of the measurements made on the thinnest of

samples, due to the low signal received from them. This is especially true for purity assessment. By preparing films of different thicknesses from nanotubes prepared from exactly the same method, we are able to determine the minimal amount of tubes needed to assess purity by Raman and absorbance spectroscopy. The starting purity of the tubes and the preparation method are the two factors which determine film purity. The transparency of the film should not affect purity, since it only depends on the amount of material present. As one can see from the linear Beer's Law dependence of absorbance on nanotube loading in Figure 17, the visible spectrum absorbance measurements are accurate for all loadings. However, the absorbance purity is not. The Itkis purity in Figure 17 is only constant for higher loadings, and begins to become erratic at $0.8\mu g/cm^2$ (93%T).

Raman purity in Figure 18 exhibits a similar behavior. The intensities of the G band increase linearly with loading, but the variance of the G/D ratio at low loadings is so high that samples thinner than $0.7\ \mu g/cm^2$ (95%T) cannot have purity accurately assessed with our equipment.

2.6 Figure of Merit

Since we are interested in comparing preparation methods to arrive at the best way to make a nanotube film, and our ultimate goal is a high transparency low resistance film, it was necessary to find a way of comparing quality of films. A comparison of a single factor such as conductivity between films is not an accurate assessment of film quality, as conductivity, of course, changes with film thickness. A thick film made of poor material may have a higher conductivity than a thin film made of good material. In order to compare the quality of our films

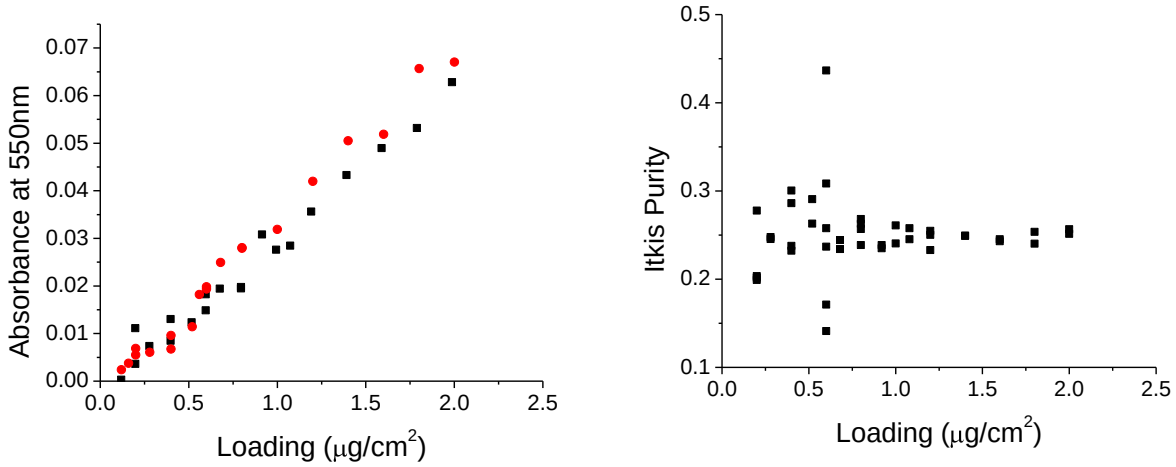

Figure 17 Absorbance has the expected linear dependence on loading throughout all thicknesses, and therefore can be used as a metric of nanotube density at all thicknesses. However, absorbance purity is not reliable for films thinner than 0.8μg/cm^2.

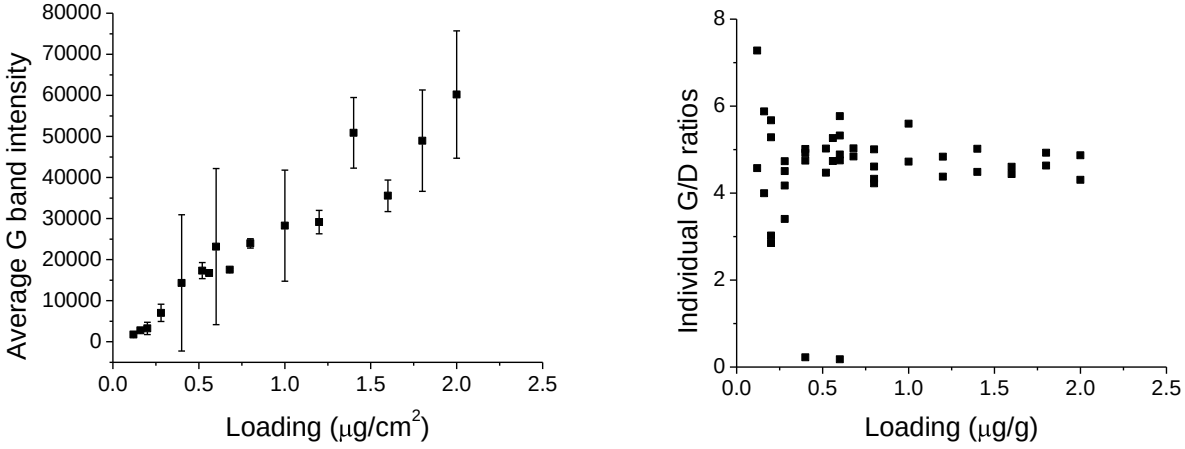

Figure 18 The signal intensity, as measured by the G band peak, increases with nanotube density, but the Raman purity becomes less reliable at low densities.

based on method of preparation, an assessment metric, the figure of merit (FOM), was introduced, which depends on transparency and conductivity [12]. For reasons described below, we will use the quantity absorbance/conductivity as the FOM to compare films. A lower number means a higher quality film.

Dividing sheet resistance by visible-spectrum transmittance (T/R) is a common way of assessing thin film quality, in some cases along with modifications to correct for desired emphasis on transparency over resistance [63, 64]. Since the ideal film has a high T and low R, the larger value of T/R, the higher quality film. For several reasons, this is not the best quantity to assess quality of nanotube films.

It is important to understand how the properties of absorbance, transmittance, and resistance scale with the thickness of nanotube films. For nanotube networks, like traditional films, absorbance scales linearly with thickness, in accordance with beers law (Figure 17). However, the resistances of traditional thin films scale with thickness differently than nanotube films, as the latter are percolating networks, while the former behave as bulk materials. For a bulk material, one would expect that resistance decreases in proportion to thickness, in accordance with the well-know relationships between resistivity and resistance discussed in the beginning of this chapter. However, a network of nanotubes obeys a percolation law and therefore the relationship between resistance and thickness has strong nonlinear behavior at low nanotube densities, although it can be approximated as linear for the thickest of films.

The ideal FOM would be dependent on the method used to prepare the film only, and independent of film thickness. For example, if the plot of R vs T was a line that intersects the origin, then the slope of that line would just be R/T, a constant independent of thickness, and therefore would be an ideal FOM. This is not the case. As Figure 19 shows, for a network of nanotubes, R vs T has a strongly nonlinear dependence on thickness for all loadings, whereas Abs vs σ is approximately linear for films %T<90. This line does not intersect the origin, so Abs/σ is still a less-than-ideal FOM. The slope of this line is, of course, constant, so slope could be used as a thickness-independent FOM for assessing films with %T>90. Unfortunately, this would require having films of several loadings for each method of preparation in order to fit the data, which is at best time consuming, and often not possible. A method which only requires one film to determine the FOM is the only experimentally viable one.

Abs/σ was chosen over the more common Resistance/Transmittance, as R/T varies more with thickness than Abs/σ, as can be seen in Figure 20. Since Abs/σ, too, is not completely independent of thickness, film thicknesses therefore still have to be within a certain range of one another to be compared. This thickness dependence is especially pronounced for high transmittance films, but becomes increasingly negligible as film thickness increases.

Even for high transmittance films, nearer the percolation threshold, where the thickness dependence is most pronounced, Abs/σ still has less variation than R/T. Over a wide range of thicknesses (60%-90% T), Abs/σ only varies by a factor of two, while R/T varies by a factor of seven; Abs/σ varies by a factor of 1.4 between 92% and 97% transmittance, while R/T varies by

a factor of 3.8 (Figure 20). We therefore have chosen Abs/σ as the FOM to be used in assessing quality of our films, with lower values of the FOM corresponding to higher quality films.

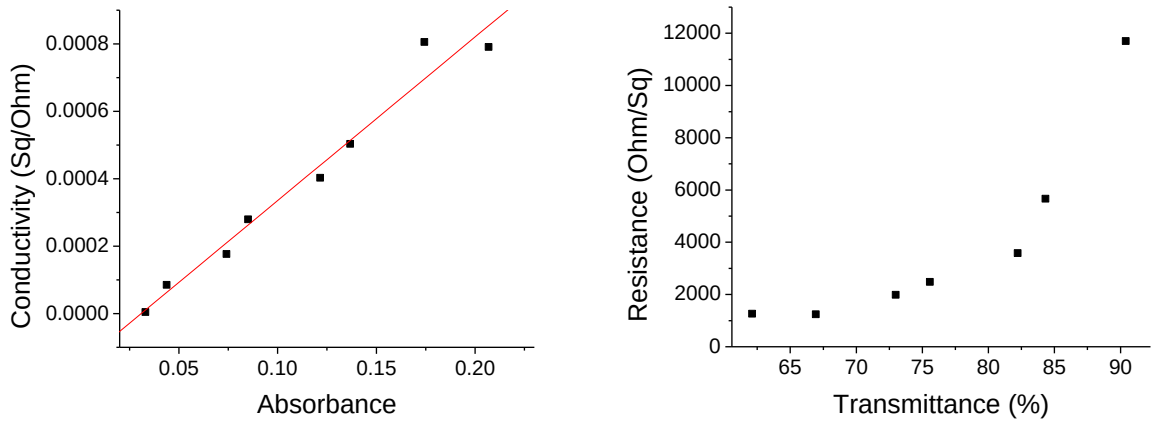

Figure 19 SWNT dispersed in pH 11 Triton X-100. For nanotube loadings which give T<90% σ vs Abs is approximately linear, while R vs T is not.

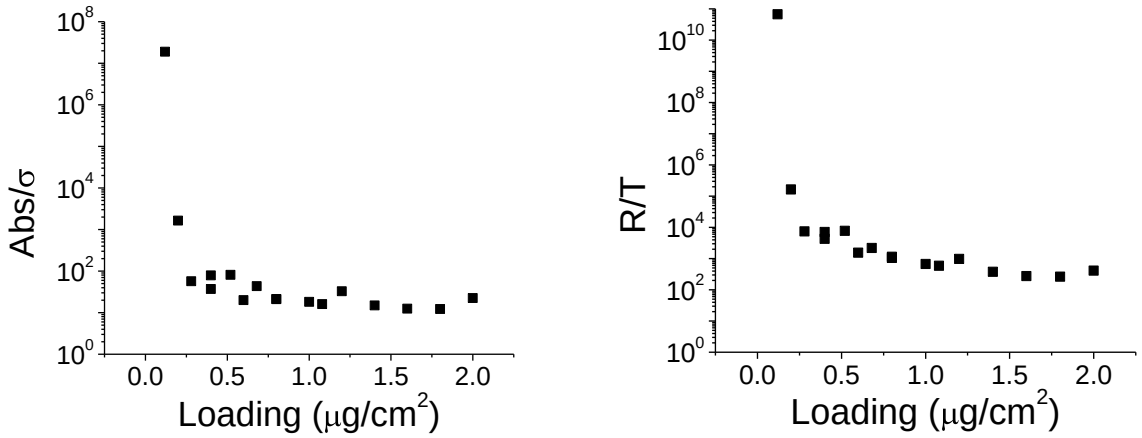

Figure 20 Both options for figure of merit are not constant as a function of loading, especially at the lowest of loadings.

CHAPTER 3 STUDY OF THE EFFECT OF DISPERSION METHOD ON FILM QUALITY

3.1 Experimental Approach

Different methods of dispersion yield different size bundles and amounts of aggregates, both in solution and on the final sample. The choice of solvent and method of dispersion, for example, sonication or shear mixing, can also change the nature of the nanotubes in the solution. An optimal dispersing agent, most likely either an organic solvent or a surfactant, needs to be found. Also, a method of dispersing nanotubes in the agent is necessary for optimizing the network when the film is made. This is further complicated by the fact that prolonged sonication can degrade nanotubes, inducing defects, shortening them, and breaking them down into amorphous carbon. Sonication can also degrade some solvents, forming a polymer coating on the nanotubes. Therefore there should be an optimal sonication time in a given dispersant, where the nanotubes are de-aggregated enough to form a conductive network at low loadings, but do not yet have large amounts of defects or extra amorphous carbon, which adds to the absorbance without creating conductive channels. Even when the SWNT have been dispersed optimally, the film conductivities for different dispersants can vary by orders of magnitude. It is necessary to have a method for determining the best dispersant and to understand why certain dispersants are better than others.

To determine the optimal dispersion method for SWNT, nanotubes were sonicated for varying times in several dispersants, and films made at each stage of the dispersion. The conductivity and transparency of each film was assessed to determine the FOM. This allows the optimal

dispersion for thin film applications to be determined. This does not necessarily mean that the nanotubes themselves are better dispersed, only that the dispersion is better suited for thin film manufacture. For example, a dispersant which produces very long yet thin bundles, or which dopes the bundles during dispersion, may yield a better FOM than an "ideal" dispersant that yields monodispersed tubes. Absorbance purity analysis, Raman spectroscopy and SEM imaging were performed on each sample at each stage of dispersion in order to understand the mechanisms which make some dispersants work better than others.

The degree of dispersion depends on container shape, volume of solution, type and purity of nanotubes, and many other factors. We have found this high number of variable factors make it impossible to set a specific "optimal sonication time", even for a given dispersant or a given nanotube sample. For example, round bottom flasks and small volumes of solution tend to disperse tubes more quickly than large volumes in containers of other shapes. Also, solutions of SWNT "bricks" which have undergone baking (and therefore compression) in a chemical purification procedure tend to take longer than raw (fluffy) SWNT to reach an un-aggregated, uniform color dispersion. Dispersion is further complicated by the tendency of nanotubes to quickly re-aggregate once sonication stops, in some cases aggregation has been observed while measurements are ongoing. Despite these complications, we were able to acquire an understanding of the processes involved which affect resistance and transmittance among various dispersants, and determine which dispersants yield higher quality films.

3.2 Choice of dispersants

Many chemicals were studied for their ability to disperse SWNT. Carboxymethyl cellulose salt can be dissolved in water at sufficiently low concentration (0.01%), and used to disperse SWNT. Higher concentrations are too viscous to use in making films. Despite dispersing well, it was found that the SWNT do not adhere to the filter during the filtration process, precluding the making of a uniform film. Dispersion with 0.005% humic acid sodium salt in water was also attempted. Low concentration was also necessary, due to the dark color of the mixture, and due to the inability of higher concentrations to pump through the filter pores. Humic acid film quality was poor, 4900Ohm/Sq at 70%T, with the low visible-spectrum transmittance expected, due to the brown color of the dispersant. $SOCl_2$ and H_2SO_4 were also found to disperse SWNT, but are not compatible with the filter material. Also, despite $SOCl_2$ dispersing tubes very quickly upon sonication, the tubes also precipitate out very quickly, the uniform solution becoming visibly re-aggregated within a matter of seconds after completion of sonication.

Xylene and Toluene were also explored as dispersants. Both exhibited an increase in Itkis purity, and either a decrease in or unchanging G/D ratio as sonication progressed (Figure 21). Solutions of both solvents remained heavily aggregated throughout prolonged sonication, which contributed to the relatively poor film quality (as compared to surfactants) from these solvents. The FOM for SWNT films prepared from each of these never falls below 200, whereas with surfactants, FOM's below 100 are regularly attained. The importance of the Iitkis purity increase and the G/D ratio decrease will be described further in chapters 3.4 and 3.7.

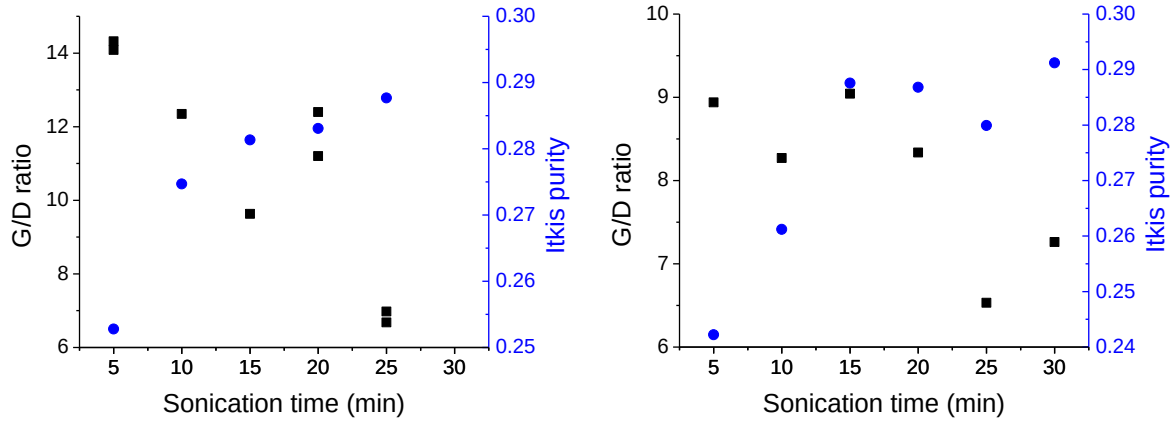

Figure 21 Films made from dispersions of Toluene (left) and Xylene (right). Sonication quickly induces defects into the SWNT, as measured by Raman spectroscopy (squares), while absorbance purity (circles) continues to increase as the SWNT become better dispersed.

Ortho-dichlorobenzene was found to disperse SWNT well. However, sonication in ODCB quickly introduces defects into SWNT, as determined by Raman Spectroscopy. ODCB is known to polymerize upon prolonged sonication [65, 66], and this polymerization is evident in the SEM images of Figure 22. Most notably, the polymerized solvent causes a significant decrease in transmittance as sonication time increases (Figure 23). Despite this, ODCB-dispersed films were of high quality, with FOM's below 100. This is due to the doping effect of ODCB on semiconducting SWNT, and is discussed in chapter 6.

Surfactants such as SDBS, SC, Triton X-100, and SDS were found to disperse SWNT most easily, as compared to solvents. This is evident from the larger bundle sizes found in solvent dispersed films over surfactant dispersed films, as seen in Figure 24. Triton X-100 and SDS were used most extensively to disperse SWNT, with SDS giving the highest quality films, with

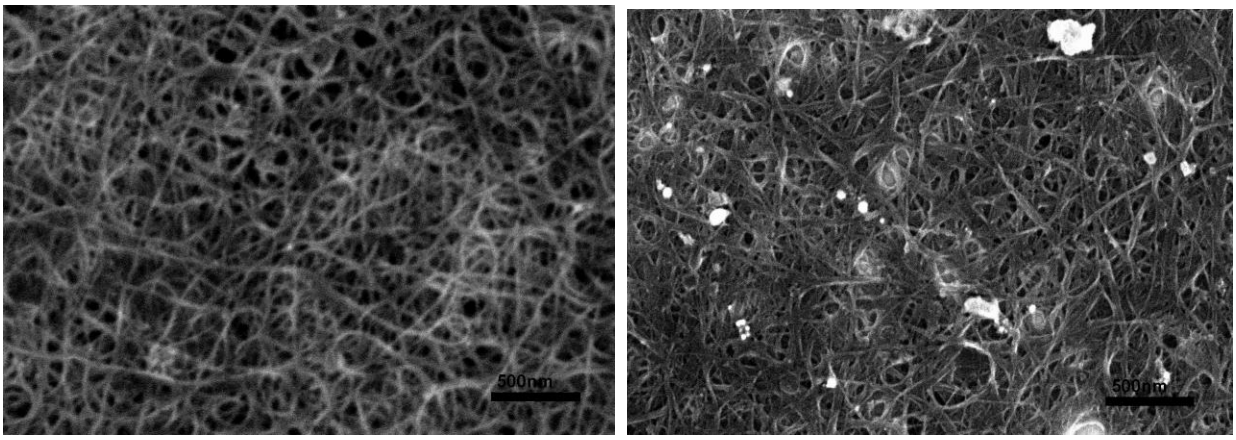

Figure 22 SEM showing pure SWNT dispersed in ODCB. Right image shows intense polymerization from the solvent, left image shows film where little solvent degradation has occurred.

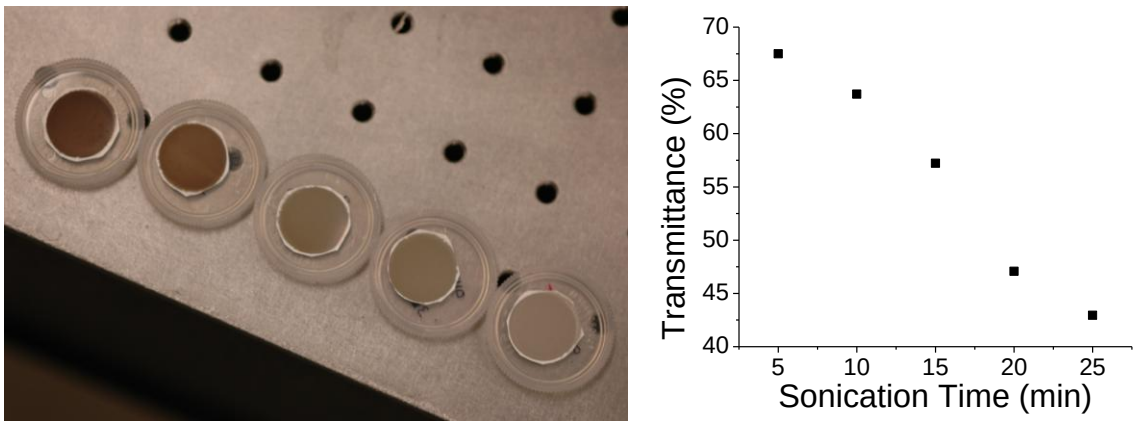

Figure 23 Films made from a constant volume of SWNT/ODCB solution. The solution was sonicated at varying times from 5min (far right) to 25min (far left). Samples get progressivly darker as the solution undergoes more sonication, due to ODCB polymerization on the nanotube surface.

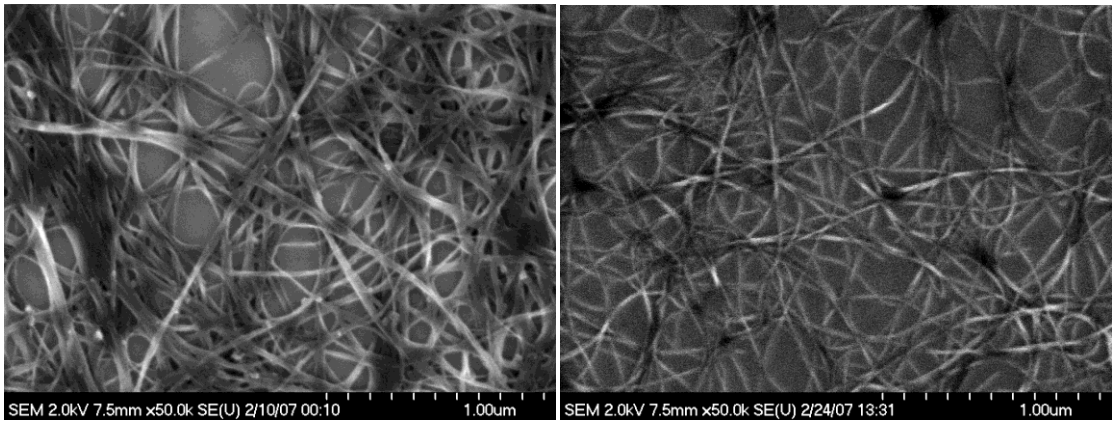

Figure 24 Dispersion in toluene (left) and sodium cholate (right). Surfactants yield smaller bunle sizes than solvents, and those films are of higher quality.

FOMs below 50. The results of these dispersions are discussed in depth in the following sections.

3.3 Effect of dispersion time and surfactant choice on film transmittance

Sonication has been carried out over a range of time periods for solutions of each dispersant studied. As sonication time increased, we found that the FOM improved (decreased) in all cases except for ODCB. This was almost always due to an increase in conductivity, rather than a drop in absorbance, with ODCB being the most notable exception, as discussed previously. In the case of ODCB dispersions, the FOMs did reach minimums, and then increased rapidly as tube quality degraded without becoming further dispersed.

Given that a solution contains a given amount of nanotube material, one might expect that the solution would have a constant absorbance, independent of the amount of sonication the solution has undergone. This was observed for SDS; however, Figure 25 shows that absorbance did increase with sonication time for Triton X-100. This increase was less significant than the

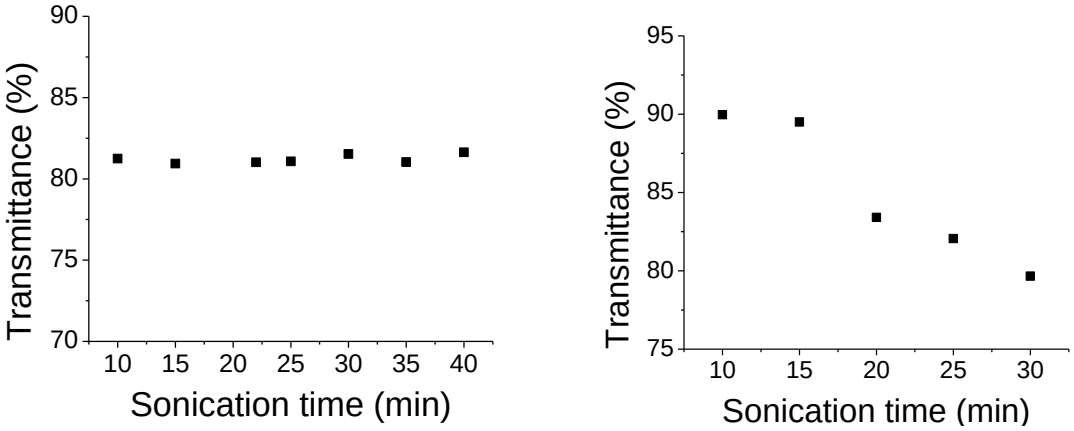

Figure 25 For progressively longer sonication times, the transmittance of films made with SDS (left) remains constant, while the transmittance of films made with Triton X-100 (right) decreases.

change observed from sonopolymerization of ODCB. While sonopolymerization of ODCB and other haloaromatic solvents is a well known phenomena [65, 66], no such sonopolymerization is known to occur in Triton X-100. Therefore it is most likely that the decrease in transmittance observed in Triton X-100 dispersions is due to a different mechanism than solvent degradation as in ODCB dispersions.

A non-dispersed solution consists of a few small, dense, nanotube aggregates which have total visible-spectrum absorbance, and a dispersant which has almost no visible-spectrum absorbance. The total absorbance of this solution is therefore very small. As sonication commences, the aggregates break up into smaller pieces and eventually loose bundles and individual tubes, increasing the total absorbance of the solution. As we make films from this solution at different points in the sonication process, along with this increase in absorbance, we expect an increase in conductivity as the aggregates break into their constituent bundles. This resistance drop is observed in our films. It is therefore reasonable to assume that this observed increase in

absorbance could be due to the nanotubes becoming better dispersed (less aggregated), although Triton X-100 decomposing with sonication cannot completely be ruled out without further testing. This absorbance increase is often accompanied by an increase in absorbance purity, the implications of which will be discussed in chapter 3.7.

3.4 Raman purity and film quality

Sonication has been known to induce defects onto SWNT, and since these defects detract from the conductivity of a SWNT, it is often assumed that a higher number of defects will mean a lower conductivity film. This assumption, however, has never been thoroughly investigated. The best judge of nanotube defects is the Raman G/D ratio. The Raman G/D ratio decreased when Triton X-100 was used as a dispersant, but did not for SDS dispersions, meaning that sonication in Triton X-100 induces defects onto SWNT, but sonication in SDS does not. Despite the greater number of defects and the decrease in transmittance for prolonged dispersion in Triton X-100, longer sonication times did yield higher quality films. This means the greater number of nanotube defects at greater sonication times was typically counterbalanced by a better dispersion, so the FOM did drop. This degradation of tubes was still evidenced in the overall better FOMs achieved for SDS than Triton X-100 (Figure 26). That is, since SDS can disperse SWNT without inducing tube defects, the overall film quality was still better than films made with Triton X-100 as a dispersant.

A sample of SWNT purified by HNO_3 treatment was found to be impossible to disperse in Triton X-100 by our standard method of bath sonication, but would disperse with a cup-horn sonicator.

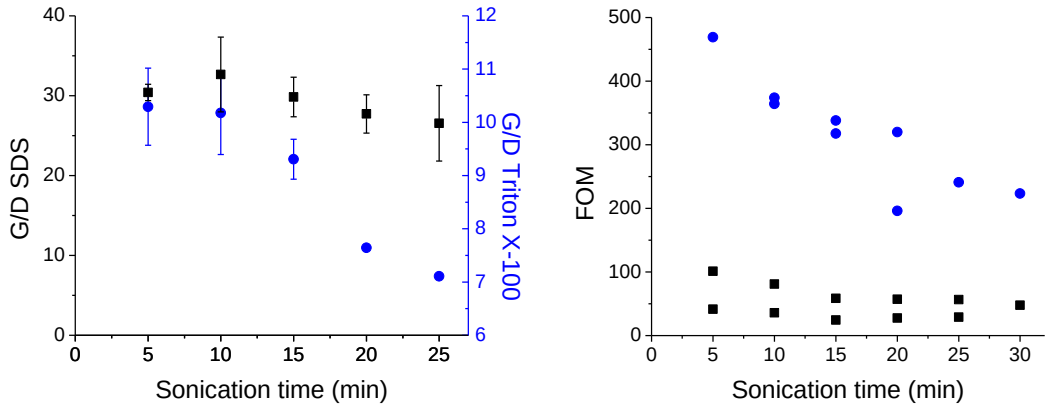

Figure 26 Sonication in SDS causes no change in G/D ratio, while sonication in Triton X-100 causes the G/D ratio to fall. SDS films are higher quality (lower FOM) than Triton X-100 films. Left: Raman G/D ratios of purified SWNT dispersed into 1% Triton X-100 in H_2O and 1% SDS in H_2O. Right: FOM for purified SWNT. SDS is black squares, Triton X-100 is blue circles.

This allowed us to monitor film quality while isolating the effects of sonication damage to SWNT from the effects of further dispersion. An initial dispersion was done with horn sonication. The solution was then moved to the bath sonicator to study its dispersion further. We found that this sonication showed no signs of further dispersion, such as a visible difference in the solution, a change in the SEM image appearance, or a change in any of the absorbance-related properties such as transition peak intensity. In addition, the transmittance remained constant, which for Triton X-100 indicates that no further dispersion is occurring. As seen in other Triton X-100 -dispersed samples in Figure 27, though, the SWNT degradation measured by G/D ratio did occur, and the resistance dropped as well. This confirms that nanotube defects induced by sonication do negatively affect film quality.

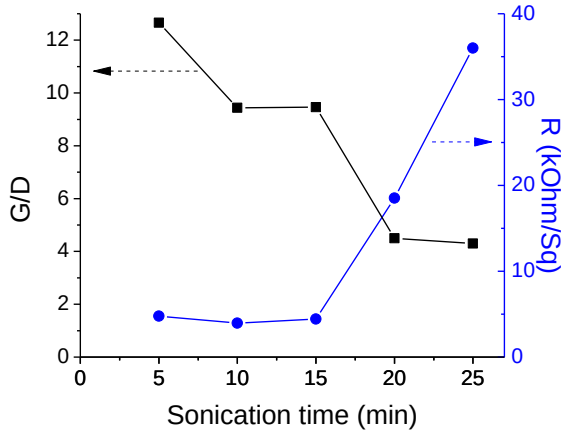

Figure 27 Relationship between nanotube defects and sheet resistance show that sonication-induced defects cause sheet resistance to increase. All films are 85%T.

3.5 Dispersion in ODCB

Dispersion in ODCB results in a low G/D ratio, as well as quickly decreasing Itkis purity upon sonication. ODCB is a nanotube dopant, and exposure to ODCB liquid or its vapors will result in an increase in nanotube conductivity. It was considered that solvent interactions could be the cause of the G/D ratio change during ODCB sonication. However, doping of SDS dispersed and Triton X-100 dispersed films by exposure to ODCB does not change the G or D band intensities, so it is reasonable to conclude that the observed decrease in G/D ratio results from sonication-induced defects rather than interaction of ODCB with the SWNT sidewalls. Similarly, some dopants are known to lower the magnitude of the semiconducting transitions in the absorbance spectrum. However, when ODCB was used as a dopant, no structure change was ever observed in the S_{22} band of the absorbance spectrum. Purity of ODCB dispersed SWNT can therefore still accurately be assessed by the Itkis method.

Itkis purity rapidly drops with sonication in ODCB, as the FOM rises (worsens). Due to the doping effect, a better FOM is attained than with other dispersants which have comparably low G/D ratios and Itkis purities, such as Triton X-100 or xylene (Figure 28 and Figure 29). Even with the doping effect, the FOM is still not as low as SDS, which does not degrade nanotube quality.

3.6 Different surfactant concentrations and film quality

For SDS, the FOM decreases as a function of sonication time, which is the case for most dispersants. Interestingly, the FOM is better for higher percentages of SDS in solution. This could support the idea that residual SDS makes the films more conductive, as higher amounts of SDS in the solution correspond to higher conductivities. However, the films were thoroughly washed, and different amounts of residual SDS would show up as correspondingly different intensities in the S_{11} band, which did not happen.

Also, the shape of the absorbance peaks depends only upon concentration of SDS, not on dispersion time. Each concentration of SDS has identical absorbance spectra for all sonication times, as evidenced by the normalized curves for each dispersant and dispersion time in Figure 30. This means that the drop in FOM as sonication progresses is caused by better dispersion, rather than SDS continuing to interact with the bundles in a manner that continues to dope the SWNT.

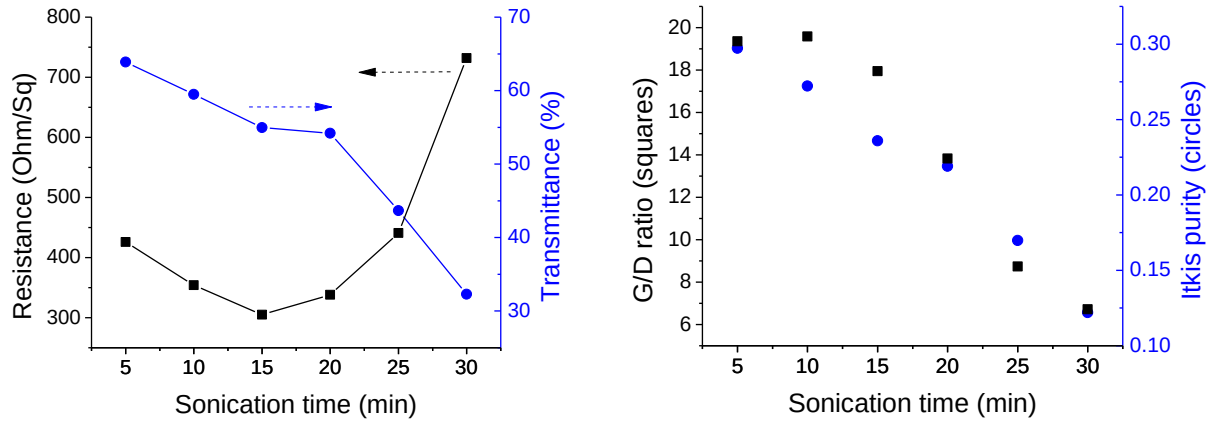

Figure 28 Solvent polymerization causes a rapid decrease in transmittance and increase in resistance upon prolonged sonication in ODCB (left). SWNT dispersed in ODCB are quickly degraded as measured by Raman G/D ratio and optical absorbance purity (right).

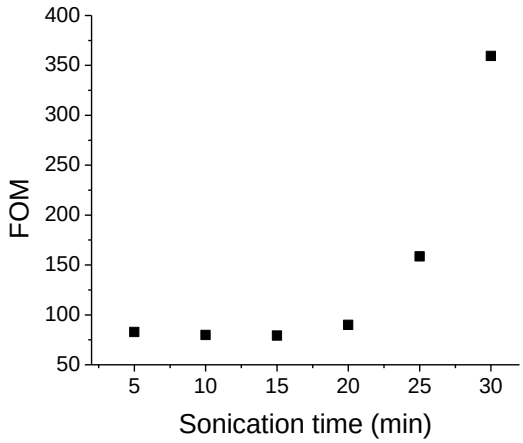

Figure 29 Figure of Merit for pure SWNT dispersed in ODCB. Film quality is degraded with longer sonication times. Each film was made with the same volume aliquot removed from the starting solution after each sonication interval.

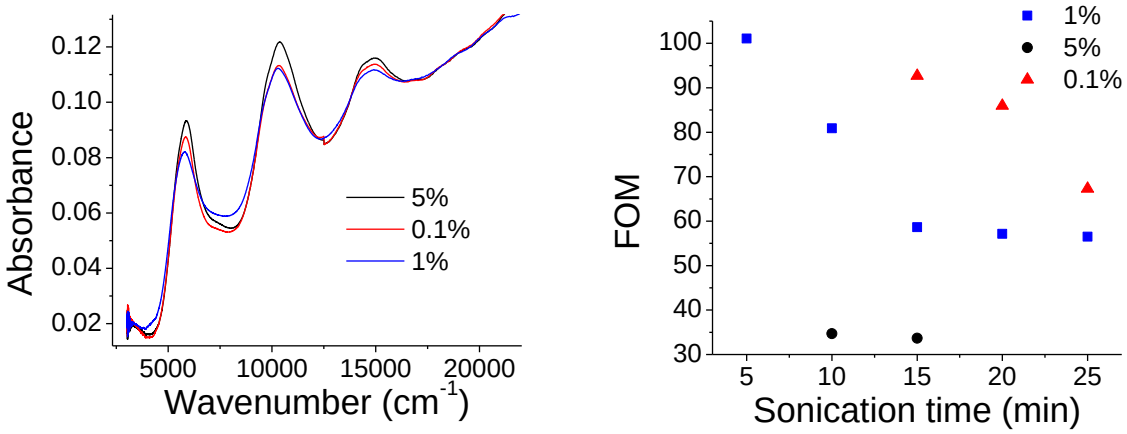

Figure 30 Absorbance spectrum and FOM for SWNT dispersed in different concentrations of SDS. S_{11} intensity does not drop along with surfactant concentration, while FOM does fall correspondingly. Due to the lack of absorbance spectrum change with surfactant concentration, the lower FOM must be related to better dispersion, rather than any SDS remaining on the films.

3.7 Itkis purity change during dispersion

If SWNT were to break down into amorphous carbon during dispersion, one would expect the absorbance purity to decrease. Otherwise, a constant absorbance purity would be expected. Surprisingly, an increase in Itkis purity is observed during continued sonication in certain dispersants, namely xylene, toluene, and Triton X-100 (Figure 31). This is a surprising result, as Itkis purity is a metric of the amount of SWNT relative to the total amount of carbon in a sample. At first glance, an increase in Itkis purity would mean that nanotubes are being created during sonication; but this is clearly not the case.

As the films are created by vacuum-pumping solution through a filter with pore size smaller than the nanotubes, it was considered that the non-nanotube carbon was being filtered through. This would leave a greater percentage of SWNT on the filter than was in the starting solution, therefore increasing Itkis purity. Carbon was never observed in the filtrate when measured with

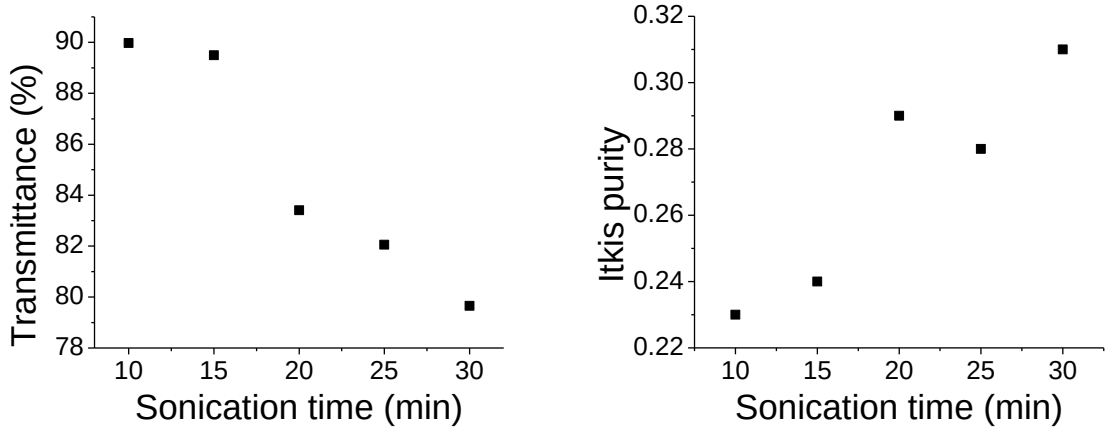

Figure 31 There is a decrease in visible-spectrum transmittance and corresponding increase in itkis purity for purified SWNT dispersed in Triton X-100.

absorbance spectroscopy, and the solution itself also exhibited an increase in purity, so this is not what is happening. If carbon was being lost in the filtration process, transmittance would also increase, as a result of there being less material in the film, when, in fact, the opposite is observed.

The real cause of this is amorphous carbon already in the starting material being thoroughly dispersed sooner than the nanotubes in the starting material. The purity for short sonication times is lower, as the spectrophotometer is detecting amorphous carbon in greater proportion to the SWNT. For longer sonication times, the SWNT are better distributed, and can be detected by the spectrophotometer as well as the other types of similarly dispersed carbon. This is in agreement with our observation that transmittance drops with continued sonication, due to greater amounts of material becoming dispersed with greater amounts of sonication. In every case in which Itkis purity increases, transmittance also falls, supporting this idea. In spite of this, it has not been completely ruled out that the Itkis purity and corresponding transmittance

increase could be caused by interactions of xylene, toluene, and triton x-100 with the nanotubes as sonication progresses. That would provide an alternate explanation to better dispersion for the observed change in absorbance properties with continued sonication.

3.8 Conclusions

Chemicals which bind to and coat the SWNT, such as surfactants, and ODCB, have been shown to be the most effective dispersants. This aids in breaking down the SWNT into smaller bundles. Solvents which do not bind to the SWNT, such as xylene and toluene, tend to exhibit larger bundle sizes, and the films are less conductive.

An ideal solvent will disperse nanotubes at the same time as, or even before, non-nanotube carbon. In this case absorbance purity would be at a high point immediately upon initial dispersion, and then remain constant if all material is equally and thoroughly dispersed. If either non-nanotube carbon becomes better dispersed or if the tubes begin to degrade into amorphous carbon due to the sonication, purity will decrease. This is what is observed for SDS dispersions. Itkis purity remains constant for the duration of sonication, without a change in transmittance, meaning that it disperses SWNT and other carbon equally well.

It has been shown that sono-induced defects notably lower film conductivity, and over-sonication should therefore be avoided. The damage from long sonication times, however, is often counteracted by better dispersion.

We have found that films made with SDS and ODCB dispersed tubes have a greater conductivity than those dispersed in Triton X-100, despite Raman G/D-band data showing that sonication in ODCB will induce tube defects and break them down into amorphous carbon. The low conductivity of ODCB-dispersed films is due to doping of the tubes during dispersion.

Films made from SDS show lower resistances at given transmittances than films made from other dispersants. The window of opportunity to make a film of given high-quality is comparably wide for SDS, holding the same FOM over a wide range of sonication times. SDS is therefore the best dispersant for SWNT that we have tested, due to its ability to quickly de-aggregate tubes with out inducing defects or breaking them down into amorphous carbon.

CHAPTER 4 PURIFICATION OF SWNT FOR MANUFACTURE OF THIN FILMS

As-grown nanotubes include impurities such as catalyst particles and different types of non-nanotube carbon, which presents a hurdle to making highly conductive thin films. Also, SWNT tend to aggregate in solution, with some nanotubes dispersing into free-floating bundles upon sonication, and others becoming intertwined into undispersible clumps. To improve the absorbance/conductivity ratio of a SWNT film, a method to remove the aggregates and impurities from solution is necessary.

Most purification techniques are time-consuming multi-step procedures which can include a combination of acid reflux, oxidation, microfiltration, or centrifugation [67-85]. After purification, SWNTs are heavily bundled as a result of strong Van der Waals interactions, and are hard to disperse without additional surface functionalization. In many cases the chemical functionalization needed for dispersion results in significant SWNT degradation [86-89], and the dispersed SWNT are of lower quality than the starting material. Physical purification procedures including chromatography, polymer-assisted purification and microwave irradiation have been also reported [70, 90-95]. Weight yields for these methods vary from 3%-50% [71, 96, 97], depending on the level of purity achieved. Despite the growing number of approaches, a 100% pure SWNT sample has never been achieved.

There have been reports on the use of simple centrifugation treatments to purify as-produced SWNT, but without the rigorous analysis of recently developed purity assessments.

Furthermore, the purity assessments which have been done do not examine the usefulness to transparent conductors [96-99]. Additionally, centrifugation has been used in the preparation of SWNT films, but without attempting to uncover the mechanisms which cause improvements in film quality [100, 101] We have undergone a thorough analysis of the effect of simple single-step centrifugation on the combined purity , resistance, and optical transmittance of the resultant SWNT films.

We have developed a single step, high yield, nondestructive procedure for the purification of laser –produced SWNTs, and examined the direct effects on the conductivity and transparency of SWNT thin film networks. The centrifugation procedure both increases the purity of the resulting film and simultaneously removes the unwanted aggregates and other non-nanotube impurities (Figure 32).

4.1 Effect of centrifugation times on purity

Raw laser-grown nanotubes were dispersed at 360 W, 40 kHz with a 5μg/g concentration in 1% wt. SDS/H_2O, until the solution was uniform to the eye (2 hours). This solution was divided into several centrifuge tubes, and centrifuged at 9000rpm (8800 x g) for varying times, from 25 minutes to 6 hours. At each time interval, a film was prepared from the top 1/3 of each centrifuge tube. It was found that at approximately 1 hour, no further improvement to the films occurred, based on electrical and optical measurements (Figure 33). Between one and two hours, however, a decrease in the number of small nanotube aggregates was noticed. Two hours was therefore chosen as the optimal centrifugation time for making films. Initially, lower spin speeds

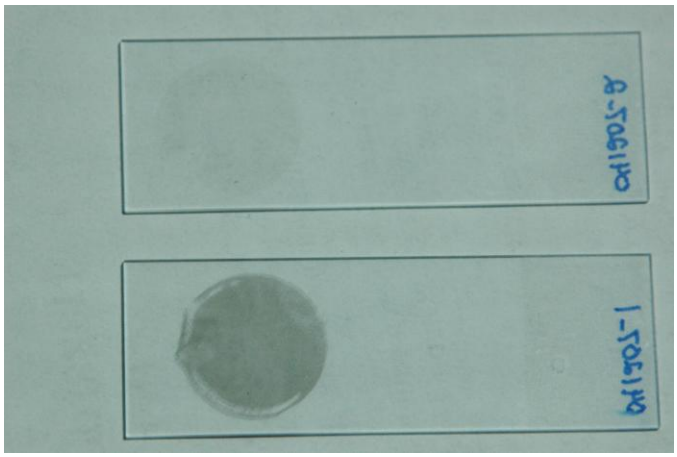

Figure 32 Film made with raw SWNT (bottom) and SWNT purified by our centrifugation method (top). Both films have the same sheet resistance (8kOhm/Sq), but the centrifugation procedure changed the transmittance from 70% to 95%

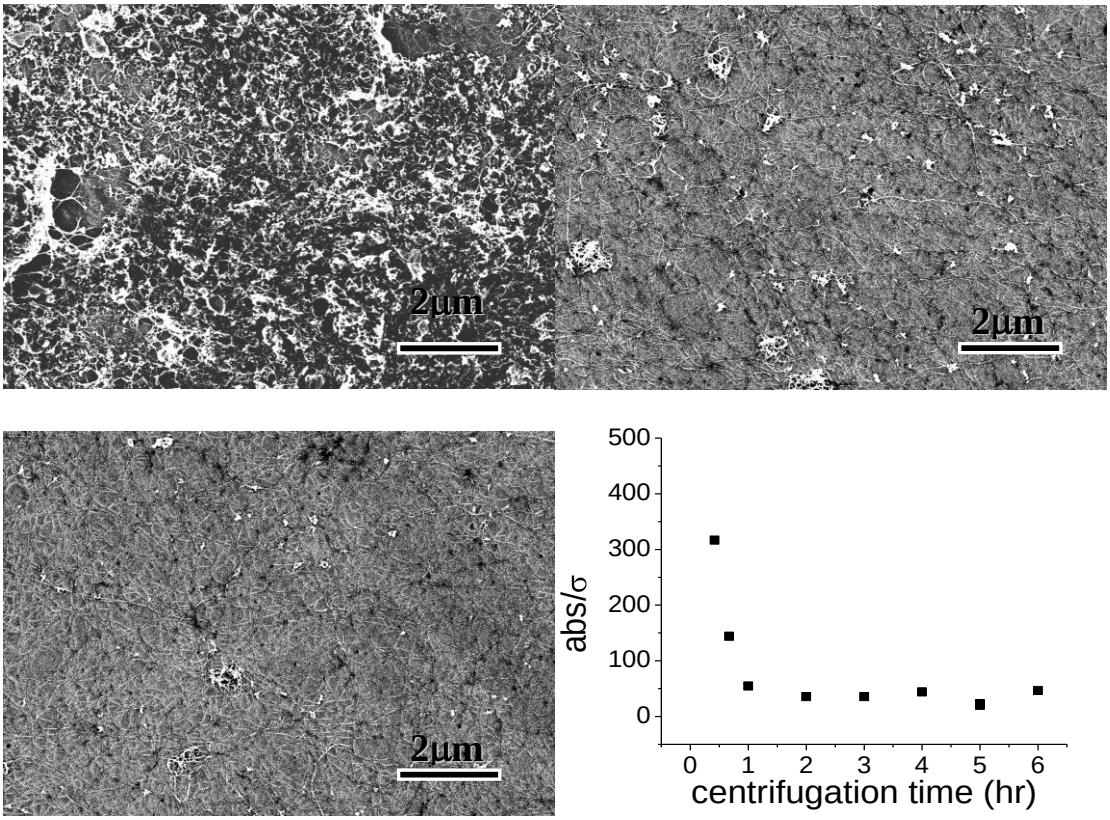

Figure 33 SEM of as-prepared material (top left), 1 hr centrifugation (top right), and 2 hr centrifugation (bottom left) . The FOM reaches a plateau after 1 hour, in which no further improvement to film quality occurs. However, SEM at a 2hr interval shows slightly fewer aggregates, and therefore 2 hours was used for further centrifugation procedures.

were explored, but were found to be ineffective. Higher speeds were not possible, due to the limitations of our equipment.

Centrifuging longer than one hour also aided in one of the bigger experimental problems of the procedure. As we were using a fixed angle rotor, and not a swinging bucket rotor, the solids tend to stick to the sides of the centrifuge tubes in addition to pelleting at the bottom. Although longer centrifuge times did not enhance the quality of the supernatant, we have found that while centrifuging for prolonged times, a greater proportion of the material is accumulated on the bottom rather than the sides of the centrifuge tube. This makes the supernatant easier to extract without disturbing the unwanted solids.

4.2 Purity gradient for centrifuged SWNT

As-produced, laser-grown SWNTs were dispersed in 1% wt. SDS/H_2O to form a 5ug/g concentration. Dispersion was carried out in an ultrasonic bath (Blackstone~NEY Multisonik 2 Ultrasonicator) operating at 360 W, 40 kHz, for 90 minutes until no aggregates were visible to the eye. A film was made with 1.5 ml of this solution, and the remaining 19 ml was centrifuged at 9000 rpm (8800 x g) in a Fisher Marathon 21000 centrifuge with a fixed angle rotor) for two hours. Six films were made with the centrifuged solution, starting with the top 3ml of the centrifuge tube, and continuing in 3ml increments until no solution remained.

As a control, chemically purified SWNT were subjected to the same sonication and centrifugation procedure to test for further improvements to films made from pre-purified material. The chemically treated SWNT were purified by HNO_3 reflux, filtration, multiple HCl

treatments, oxidative burns, and oven dryings before undergoing the centrifugation process. The chemical purification process yielded 10.7% of the as-grown material.

While still an effective method to further increase the quality of films made from chemically treated treated nanotubes, the method is most effective for improving the conductivity of films made from raw tubes. from raw tubes. The relative quality of the films was assessed by defining a figure of merit (FOM) as the (FOM) as the optical absorbance at 550 nm divided by the electrical sheet conductivity (in square/ohm). For square/ohm). For as-grown material, the FOM was improved over twelve-fold, decreasing from 1280 for 1280 for films prepared without centrifugation to 104 for films prepared with centrifugation. For pre-pre-purified material, the FOM only decreased from 188 to 144 with centrifugation. The data from the same from the same procedure carried out with raw SWNT in 1% Sodium Cholate confirm that this method of method of purification is applicable not only to SDS but to other dispersants as well (see

Table 1).

For the solution of as-grown material, the figure of merit of the resulting films was highest for films made films made with material from the aliquot taken from the top of the centrifuge tube and lowest for material at for material at the bottom. Interestingly, the bottommost aliquot was still of higher purity than the original the original solution, meaning that most of the carbonaceous impurities were concentrated in the pellet at the pellet at the bottom, and that all of the supernatant was at least somewhat purified. The series of films made films made from chemically treated material still showed an improvement in the FOM, only without the without the noted increase in Itkis purity and G/D ratio (see

Table 1).

Table 1 Optical transmittances (at 550 nm), sheet resistances, purity, and figure of merit of nanotube films prepared by different purification methods. Material without centrifugation at top, and with centrifugation in the bottom table.

dispersant/ SWNT type	kΩ/Sq	%T	Itkis purity	G/D	FOM (abs/σ)
SDS/ as-produced	19.7	86	0.1	3.1	1290
SDS/ pre-purified	2.4	83.5	0.23	8.7	188
SC/ as-produced	8	70	0.09	2.5	1239
dispersant/ SWNT type	kΩ/Sq	%T	Itkis purity	G/D	FOM (abs/σ)
SDS/ as-produced	7.6	97	0.26	7.1	104
SDS/ pre-purified	2.2	86	0.27	8.7	144
SC/ as-produced	8	96	0.18	4.6	142

For centrifugation of chemically treated material, we attribute the film-quality improvement to the removal of poorly dispersed nanotube aggregates, which, despite having high nanotube content, make little contribution to the film conductivity while detracting from the visible-spectrum transmittance. For as-grown nanotubes, centrifugation removes not only nanotube-containing aggregates, but also non-nanotube carbon, as evidenced by the change in G/D band ratios in Figure 34 and spectrophotometric purity in Figure 35. SEM images confirm this, showing a more uniform, less aggregated film for the samples which are made from centrifuged solution, while TEM of Figure 36 shows a sample freer from catalyst particles and non-nanotube carbon.

One of the most important quantities for any purification procedure is yield. A useful purification procedure will recover the largest amount of SWNT possible from the original

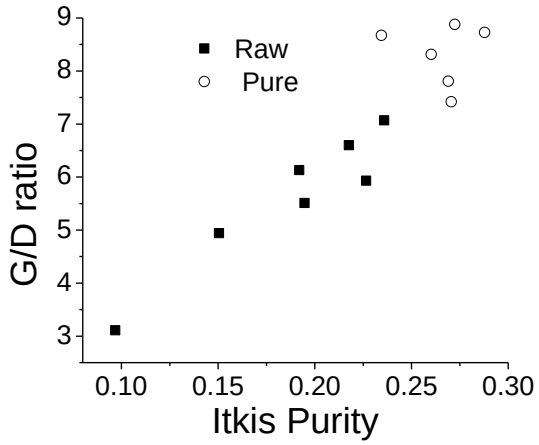

Figure 34 G/D ratio increases along with Itkis purity during centrifugation.

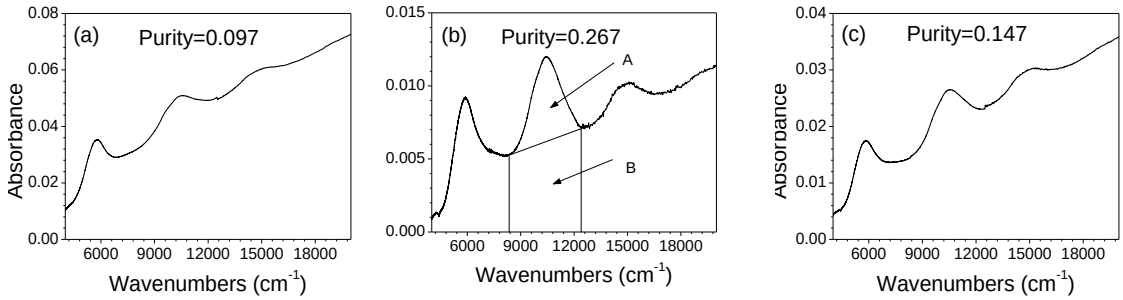

Figure 35 Absorbance spectra showing the difference in SWNT content of (a) as-prepared material (b) material from the topmost portion of the centrifuge tube, (c) bottommost supernatant of the centrifuged material. Purity = A/(A+B)

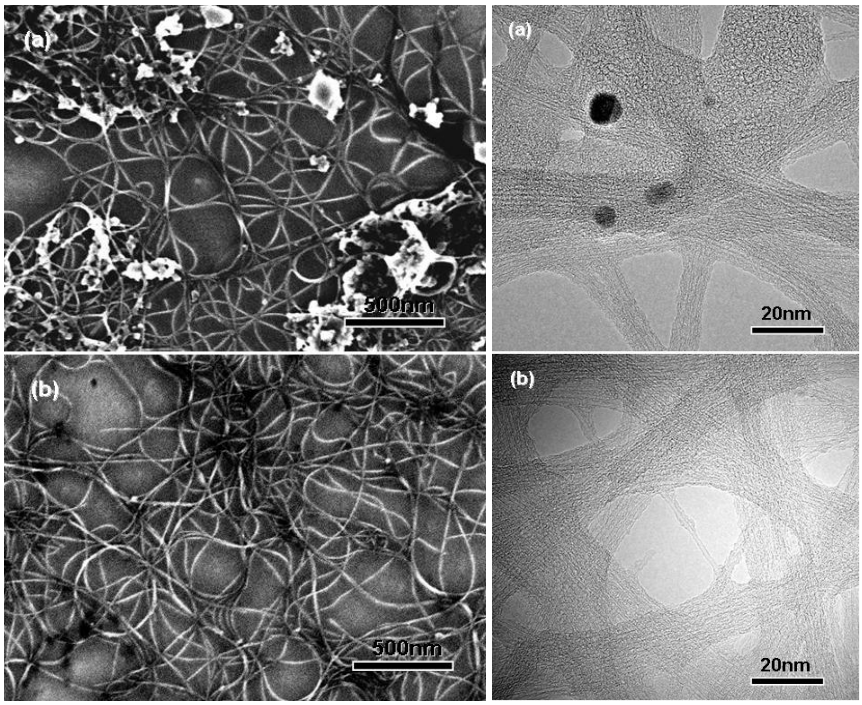

Figure 36. SEM and HRTEM images of SWNT films. (a) Top, as-produced SWNTs showing aggregates, catalyst nanoparticles, and nanotube bundles. (b) Centrifuged material (8800 g for 2 hours) showing SWNT bundles relatively free from catalyst nanoparticles and large aggregates.

material. The amount of material recovered from centrifugation of pre-purified material is greater than the amount recovered from centrifugation of raw material. Assuming a Beer's Law dependence of the visible-spectrum absorbance on the amount of SWNT per area of a film, the percent yield of pure nanotubes was calculated from the purification procedure, by comparing optical densities of each film.

The mass per unit volume of SWNT in the prepared solution is known. The ratio of the weight of this starting material to the weight of the centrifuged material will be equal to the ratio of the absorbance of starting material to the absorbance of the centrifuged material. From the known

volumes of solution that comprised each sample, the total yield of SWNT in each aliquot can be calculated (see Figure 37).

This means at a purity of 0.26, 3% of the as-produced material remains after centrifugation, and 48% of the pre-purified SWNT remain after centrifugation. However, considering that the chemical purification process yielded 10.7% of the starting material, this means that upon completion of chemical treatment and subsequent centrifugation, only 5% of the as-grown material remains. This is attributed to the loss of greater amounts of non-nanotube material during the centrifugation process of as-grown tubes over chemically treated tubes, due to the starting material having greater amounts of amorphous carbon and catalyst.

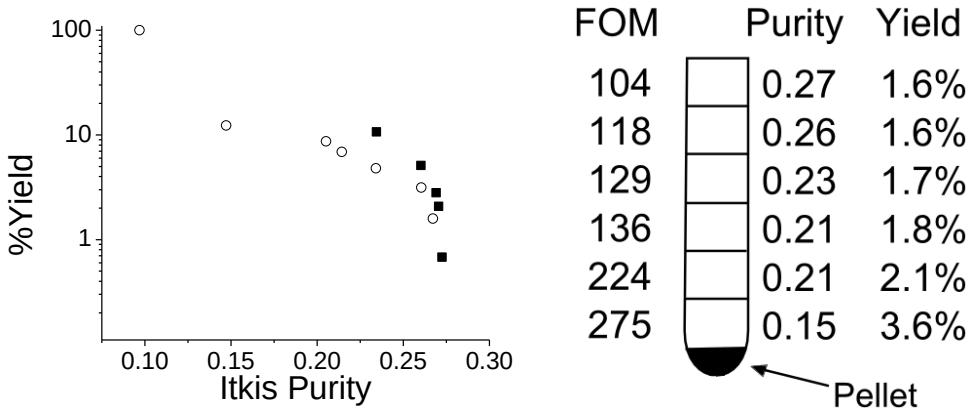

Figure 37 Yield of material available at a given purity after centrifugation, for two different qualities of starting solution. Closed squares are pre-purified material, open circles are as-grown material. The purity of the starting material are the 100%yield (as-produced) and 10.7% yield (pre-purified) data points. The diagram shows the percent of material available at a given point in the centrifuge tube for as-grown SWNT, and the corresponding purity and FOM of the film created from each aliquot.

4.3 Multi-step purification

SWNT material purified by centrifugation can be redispersed and recentrifuged in order to achieve a higher level of purity than attainable in a single step.

A 5μg/g solution of as-prepared SWNT in 1% SDS/H_2O was sonicated until uniform to the eye and then spun at 9000rpm, as in the previously described single-step centrifugation process. The top 2/3 was removed from the centrifuge tubes, and resonicated for 1hr. A film was made with this material, and the remainder of the separated solution was recentrifuged for 2¼ hr at 9000rpm. Films were made by dividing the solution into aliquots, from the top to bottom of the centrifuge tube.

The purity of films made from solution that underwent resonication and recentrifugation was purer than the film made from a single centrifugation. As expected from the higher purity, the FOM was notably improved over single-step centrifugation results (Figure 38).

Except for the bottommost part of the supernatant, which included much aggregated material, the purity of purity of the entirety of the double-centrifuged supernatant was grater than the purity of the single-single-centrifuged starting material. Inconsistencies in the purity gradient are due to mixing during the during the siphoning of solution from the centrifuge. While the purity of 0.21 is not higher than purities that purities that have been achieved by single-step purification, the achieved resistance of 360 Ohm/Sq at 87%T Ohm/Sq at 87%T was much better than films from other purification methods, even from single-step step centrifugation of pre-purified material (see

Table 1). This is likely due to the removal of

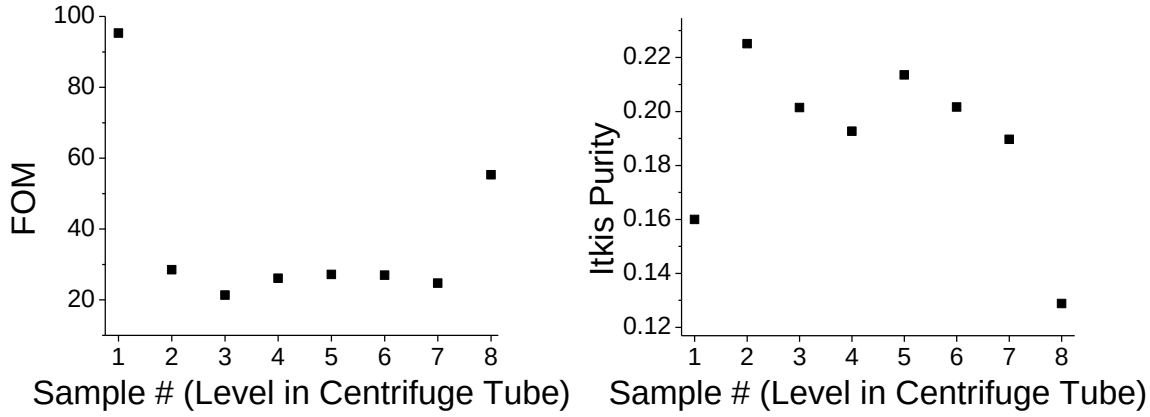

Figure 38 Multi-step centrifugation shows the best FOM of any purification procedure studied. Sample #1 is made from a single centrifugation. Samples #2-#8 are aliquots taken from descending levels of the re-centrifuged supernatant.

highly aggregated nanotubes that do not make contribution to the conductivity, but detract from the transmittance.

It was also shown that even the typically discarded bottom portion of the supernatant can be redispersed and recentrifuged to increase the quality of a film as in Figure 39. A solution of as-prepared SWNT in 1% SDS/H_2O was dispersed and centrifuged according to the standard procedure, and the top and bottom halves of the supernatant separated. The bottom portion was resonicated for an hour. One film was made with a portion of this resonicated material, and then the remainder centrifuged for 2.5 hours. The recentrifuged material was divided into aliquots corresponding to levels of the centrifuge tube, and a film made with each aliquot.

The resonicated portion without recentrifugation yielded an 1800 Ohm/Sq film with 71%T. All films made from the recentrifuged material were higher quality than this, with resistances as low as 740 Ohm/Sq at 89%T. The resistances and transmittances were consistent along the axis of

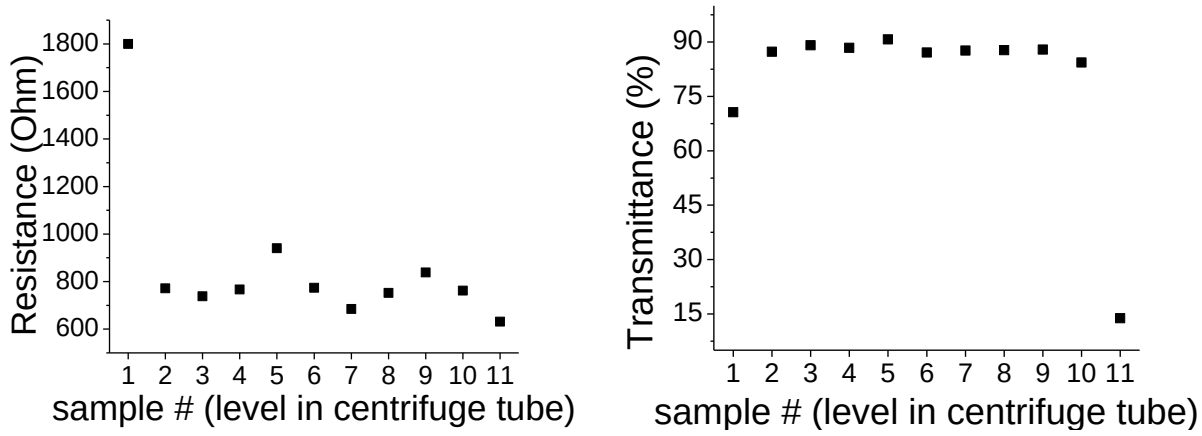

Figure 39 Recentrifugation of the bottom half of the supernatant shows an improvement in film quality also. Sample #1 is with no recentrifugation, samples 2-11 are equal volumes from the topmost (#2) to bottommost (#11) portion of the supernatant.

the centrifuge tube, with all films having a FOM of around 45, corresponding to a purity of about 0.17, as 0.17, as compared to the uncentrifuged material in

Table 1. The bottommost portion was the only exception, which had a FOM of 540 and purity 0.05. The resistance of this last film was still 630 Ohm/Sq, but the transmittance was only 14%. This shows that even recentrifugation of very low quality material can produce a film of higher quality than without centrifugation.

4.4 Purification by filtration

Filtration has also been investigated as a method to remove aggregates and purify solutions for nanotube films. Figure 40 shows a 5μg/g solution of pre-purified SWNT dispersed in 1%SDS/H_2O. This solution has been made into films after different purification methods described in Table 2.

Table 2 Sample preparation methods for Figure 40.

Sample 1	No further processing (solution as prepared)
Sample 2	filtration through a 5μm-pore filter
Sample 3	filtration through a 1.2μm-pore filter
Sample 4	centrifugation at 9000rpm, 3hr

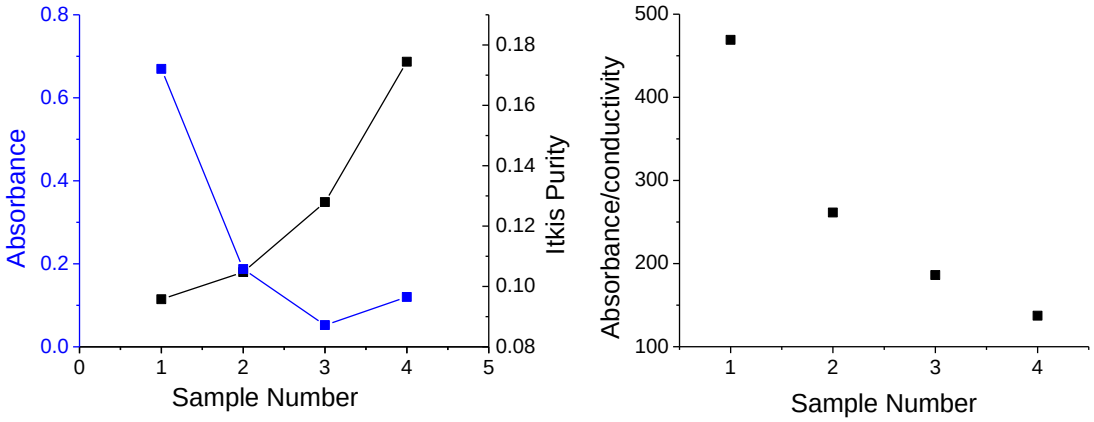

Figure 40 Change in FOM and purity due to filtration and centrifugation (see Table 2).

The solution was sonicated until visually uniform (2.5 hr), and then divided into four parts, 10ml each. The first part was made immediately into a film (sample 1). The second and third parts were filtered through a 5μm and a 1.2 μm pore filter, respectively, and then made into films (samples 2 and 3). The last part was centrifuged at 9000rpm for 3 hr, and the top 1/3 made into a film (sample 4).

Similar filtration experiments were undertaken with as-produced material, and showed no improvement in purity. A 1μm pore filtration of 5μg/g as-grown SWNT in 1% SDS/H2O yielded a film of 4.6kOhm/Sq at 36%T, whereas the parent solution formed a film of 10.9kOhm/Sq at 58%T. This is a drop in FOM from 600 to 480, both corresponding to Itkis purity of 0.08.

It was found that filtration can purify SWNT solutions and improve film quality, but only if the starting material is already sufficiently pure. However, the degree of improvement was not comparable to centrifugation, which results in greater purity than all filtered material and a greater yield (as judged by absorbance) than the smaller pore-size filtration.

4.5 Swinging-bucket rotor

Due to the solid material accumulating on the walls of the centrifuge tubes rather than the bottom, it was considered that a swinging bucket rotor would be beneficial to the purification process. A swinging bucket rotor has the advantage over a fixed angle rotor in that the centrifugal force vector points along the tube axis rather than at an angle with it. Material would therefore be pulled only to the bottom of the container, rather than into the container walls.

A uniformly dispersed 5μg/g solution of as-grown SWNT in 1% SDS was spun at 13000xg for one hour, and another for two hours in a centrifuge with a swinging bucket rotor. Two films were made from each centrifugation condition, using the top half of the supernatant: one film from the top ¼, and another from the second ¼. In Figure 41, samples 1 and 2 are from the one hour centrifugation, samples 3 and 4 are from the two hour centrifugation. Sample 5 is from the original solution, with no centrifugation. The best result from this experiment was a film with 410Ohm/Sq resistance at 84%T, in comparison to the film made from the portion of the solution which was uncentrifuged, which had 2050 Ohm/Sq at 71%T. This corresponded to an improvement in Itkis purity to 0.21 from 0.10. While not as high of an Itkis purity, this is a

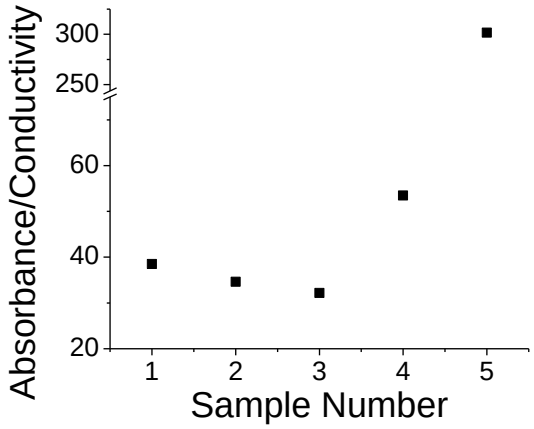

Figure 41 Figure of Merit from centrifugation with a swinging bucket rotor. Samples 1 and 2 are from the one hour centrifugation, samples 3 and 4 are from the two hour centrifugation. Sample 5 is the original uncentrifuged solution.

notably higher film quality in terms of FOM, as compared to the values in
Table 1, and is only comparable to the better R and T values achieved through multi-step purification with a fixed-angle rotor. It is clear from this that better results would be achieved from our standard procedure by implementing a higher RCF and using a swinging bucket rotor.

4.6 Crown Ether Modified SWNT

A solution of water-dispersed SWNT modified by exposure to crown ether was also subjected to a centrifugation procedure. CE-modified SWNT were found to be stable in water over a period of many months, and this solution was used in the OLED/OPV devices by adding it to polymer. The stable, already-prepared solution was diluted to a 2μg/g concentration, and sonicated for ten minutes. The sonication was shown to increase the absorbance purity from 0.10 to 0.20, by more uniformly dispersing the SWNT. Centrifugation at 5000, 8000, and then 10000 rpm for 20minutes at each speed caused no increase in purity over sonicated material which had undergone no centrifugation. The FOM also remained unchanged around 1300. Separating the

top and bottom halves of the supernatant and re-centrifuging for 30 minutes did not improve film quality. All samples from the re-centrifuged material actually yielded a purity lower than the material which was sonicated but not centrifuged, but was still higher quality than the suspended SWNT that was not sonicated. This lower purity is possibly due to re-aggregation. Centrifugation therefore has no benefit when working with CE-modified SWNT in water solution.

4.7 Conclusions

Removal of aggregates and impurities by filtration improves films only if the starting material is sufficiently pure, and in no case exhibits any advantage over centrifugation techniques. Chemical purification as extensively studied in the literature alone has no advantage over simple centrifugation for preparation of SWNT films, although when combined with the centrifugation technique, results in a higher quality film than centrifugation alone. Higher spin speeds (>10000rpm) and a swinging bucket rotor proved advantageous over a fixed angle rotor, making the supernatant easier to remove and the resultant film less aggregated. Two-step centrifugation gives higher purity material than single-step centrifugation, and purification with multiple centrifugations of as-grown material has been shown to give better FOM films than single centrifugation of chemically pre-purified material.

The process we have developed for purification by centrifugation has been shown to be the most effective method of purifying SWNT for use in thin film applications. The resultant pure-SWNT solution can be made directly into a film, while most other purification techniques require redispersion into solution which induces damage to the nanotubes, partially reversing the

achieved purification. It can be applied to multiple dispersants and does not require the use of harsh chemicals or time consuming multi-step processes. It can even be used to improve the quality of films made from varying levels of high and low purity, with higher purity starting solution having a higher yield. We have shown that using this procedure, by simple centrifugation films produced from raw SWNT can, be made to the same purity as SWNT purified by extensive acid-oxidation treatment methods, and with a comparable yield.

CHAPTER 5 IMPEDANCE SPECTROSCOPY ANALYSIS OF SWNT NETWORKS

5.1 Relation between two-probe and four-probe measurements

In order to determine the contribution of probe-tip to film contact resistance, two-probe and four-probe resistance measurements were compared. The four-probe measurements were DC resistance with the Keithley 6430 source-ohm-meter. For the two probe measurements, the low frequency values attained with impedance spectroscopy were used. This was done based on the experimentally verified assumption that low frequency AC impedance is the same as DC resistance. These techniques are described in chapters 2.1 and 5.2. From equation 2.10, we have the direct relation of four-probe and two-probe resistance for any sample, so that

$$R_{4\,probe} = AR_{2\,probe} \tag{5.1}$$

with equation 2.12, $A = \frac{\ln 2}{\ln s}$. For the tip spacing we have, s=15.9, measured in units of tip radii [102, 103], since for our setup, the tip-to-tip spacing is 1.59mm and the tip radius is 0.1mm. Therefore we expect that A=0.25.

Experimentally, four-probe resistance is found to be 0.22 times the two-probe resistance, for a constant distance between probes (Figure 42). This is very close to the expected value of 0.25. If the contact resistance was a contributor to the two probe resistance, the experimental value of A would be expected to be smaller than the calculated value, as observed.

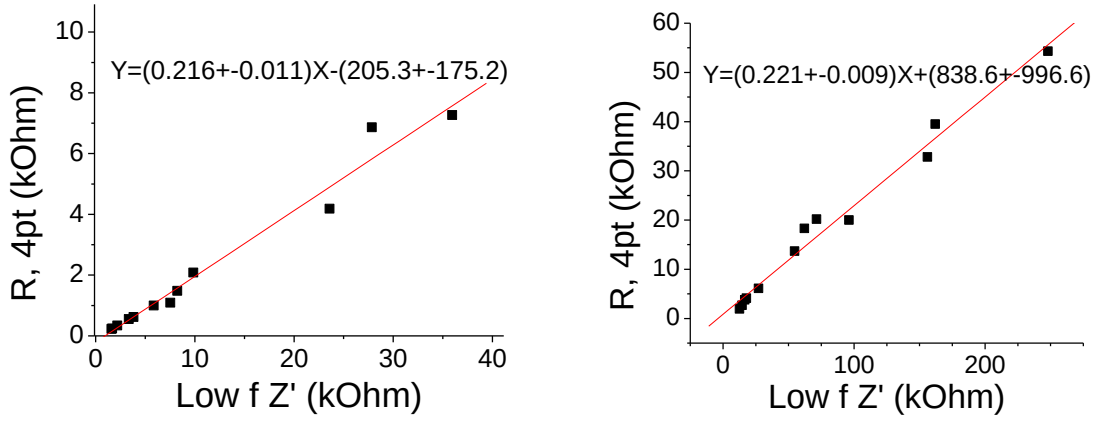

Figure 42 Four-probe DC resistance of a series of SDS-dispersed (left) and Triton X-100 dispersed (right) films as a function of two-probe low-frequency AC resistance. The values of both are linearly related by a slope of 0.22.

This "contact resistance" is often interpreted as the probe tip being in less than complete contact with the surface, and is perhaps better referred to as a "constriction resistance" [102]. Neither the film nor the probe tip is uniformly smooth, so only a certain percentage of the surface area will be in contact. The resistance arises from the current being constricted to certain areas of the probe-film contact, rather than from the tip-film interface itself. A value of A=0.22 rather than A=0.25 gives, from $A = \frac{\ln 2}{\ln s}$, an effective tip radius of 0.07mm rather than 0.1mm, which implies that 50% of the tip is in contact with the film.

The comparison between two and four probe measurements can be done by simple multiplication since this factor of 0.22 is universal among nanotube films, and this effective tip radius should be used when determining film properties from spreading resistance calculations. It is important to note that this calculation holds true for the probe tip setup used in these experiments, and would have to be repeated for any other set of probes.

5.2 Impedance Spectroscopy

While four-probe DC measurements are sufficient to give the sheet resistance of a sample, AC measurements can give much more information about the response of individual parts of the network that would not otherwise be attainable. By viewing each part of the network as an idealized circuitry component, the contribution of network features to overall electrical properties can be determined from AC impedance.

The AC Spectroscopy system works by sourcing an alternating potential of the form

$$V(t) = V_0 e^{i(\omega t)} \tag{5.2}$$

The response signal is a current, shifted by a phase factor

$$I(t) = I_0 e^{i(\omega t - \varphi)} \tag{5.3}$$

The impedance of the system is therefore expressed in the complex polar form of impedance magnitude Z_0 and phase angle φ

$$Z(t) = \frac{V_0 e^{i(\omega t)}}{I_0 e^{i(\omega t - \varphi)}} = Z_0 e^{i\varphi} = Z_0 \cos\varphi + iZ_0 \sin\varphi \tag{5.4}$$

For purely resistive behavior, φ=0, and the impedance consists entirely of a real term, Z'. When inductive and/or capacitive elements are introduced, the phase is shifted, and an imaginary component of impedance, Z", appears. At sufficiently low frequency, ω, the imaginary part of admittance and impedance approaches zero, and the real part of the complex impedance, Z', is equivalent to the DC resistance of the system. The direction of the phase shift (the sign of φ) depends on whether the circuit is dominated by inductance or capacitance. A capacitive circuit has negative phase angle, whereas an inductive circuit has positive phase angle.

Impedance spectroscopy, along with a knowledge of RCL circuitry, therefore allows us to determine which combination of R, L, and C appears in network. We know that a capacitor has impedance $Z = 1/i\omega C$, while an inductor has $Z = i\omega L$. This means that at high frequency a capacitor is a closed circuit (invisible to the tester), whereas an inductor is an open circuit. At low frequency, the opposite is true, a capacitive circuit will be open (have a high R) and inductive circuit will be closed (have a low R). Our SWNT networks behave as a capacitive circuit, and since no inductances have been observed in these networks, only capacitance elements will be discussed in depth here.

Impedance data can be modeled as a set of specific circuit elements. Any circuit as seen from a given set of terminals, no matter how complex, behaves as if it consists of only a source and impedance. From the superposition principle of Ohm's law, a complex circuit can be reduced to a simpler set of equivalent circuits. The nature of these equivalent circuits can be deduced from impedance data, independent of any knowledge of the actual elements that make up the circuit.

Modeling of impedance data is done by analysis of the plot of -Z" vs Z', commonly called a Nyquist plot, or a Cole-Cole plot (shown in Figure 43). A simple RC circuit, in series or parallel, will result in a semicircular Nyquist plot.

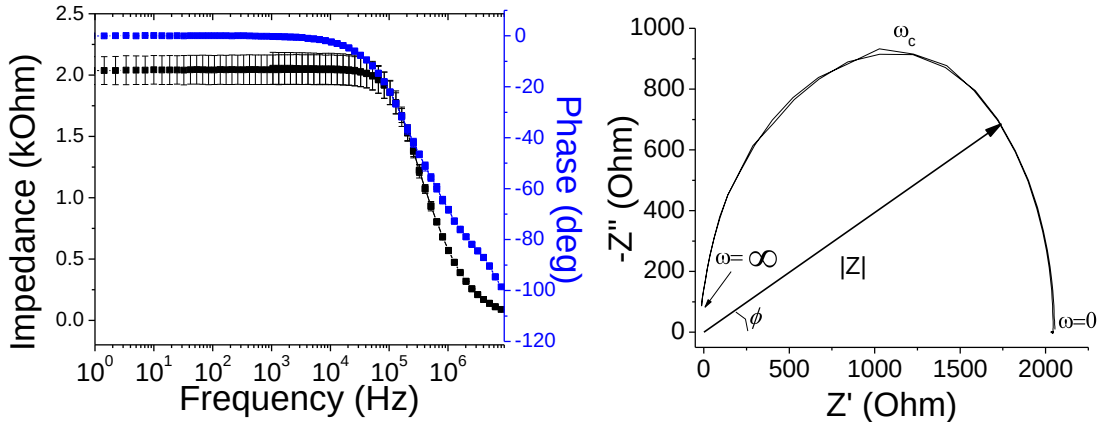

Figure 43 Impedance of a SWNT film. |Z| and phase may be shown as a function of frequency, or broken into components as a Cole-Cole plot.

From the Cole-Cole plot, the value of the circuit resistance is the right-most value, corresponding to ω=0. The highest point in the arc, the Z" maximum, is the circuit's critical frequency. This critical frequency is evident as the sharp falloff of |Z| in the impedance vs frequency plot. The capacitance can then be calculated from $C = 1/\omega_c R$, the well-known critical frequency relationship for RC circuits. This measure of capacitance is based on the assumption that the circuit being studied behaves as a simple RC circuit, and the impedance arc is therefore truly semicircular. However, our networks, like most systems, are not that simple, consisting of multiple superimposed arcs, and require advanced fitting techniques to determine the proper equivalent circuit to describe the sample. Unfortunately, as Figure 44 shows, there are often multiple equivalent circuits which have the same impedance, yet consist of different elements, which complicate choosing a physically meaningful model .

To find the appropriate equivalent circuit model for our data, we have used *EIS Spectrum Analyser* developed by Bondarenko and Ragoisha of Belarusian State University, Belarus. This

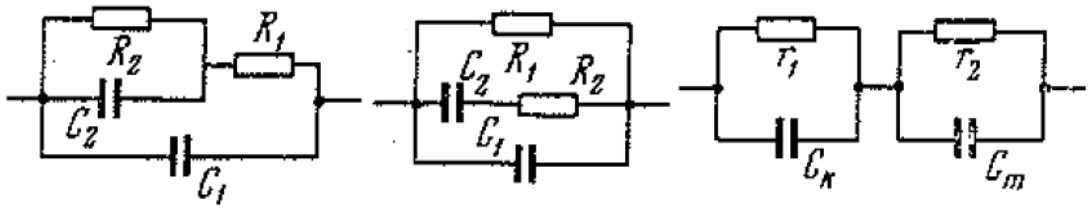

Figure 44 With appropriate choices for each R and C, each of these three equivalent circuits will have the same impedance at all frequencies [104].

allows us to make an educated guess at an equivalent circuit, and through the software, quickly determine if element values can be chosen which fit the Nyquist plot data.

5.3 Complications of electrode setup and frequency dependent measurements

Impedance measurements done in a two-probe configuration will still include effects, if any, from the electrodes and the contact interface. In an ideal case, the polarization and impedance processes of the electrode contact are of distinctly different frequency range than the processes that arise from film properties. The Cole-Cole plot will exhibit distinct arcs, one for the electrode, and the other for the bulk material [105], and the electrode impedance is then easy to separate from film impedance. Unfortunately, while this separation is common for liquid electrolytes, this is often not the case for solid samples, as the grain boundaries are often on the same impedance range as the electrode interface, especially at high frequencies [106]. This would be the case if electrode impedance were to appear in measurements of SWNT films, as the Cole-Cole plots for all of our samples appear as a single arc. With electrodes of sufficiently low impedance, the electrode interface does not appear at all, and all multiple arcs would be due to boundaries within the sample itself [107].

Four probe AC measurements, like DC, should inherently eliminate effects of the film/electrode contact, but the results from such measurements tend to be very limited due to restrictions from instrumentation. Unacceptable errors are introduced when the impedance of the electrode and contact exceeds the internal impedance of the instrument [106], which is expected for the high impedances of solid samples such as SWNT films, and is only considered practical for high-capacitance samples [106], which SWNT films are not. Others have been able to get accurate results with four-probe AC impedance using special amplifiers and sample-specific setups [108]. In cases where the electrode and bulk impedances are easily separable, the low-frequency arc is considered to be from the electrode, and the high-frequency arc from the grain boundary. In the case of SWNT networks, instead of a grain boundary, the impedance results from distances between junctions (or defects) in the nanotubes. For this reason, it is not surprising that the observed effects would occur at a lower frequency (longer length scale).

A comparison of four-probe and two-probe impedance data in Figure 45 shows a difference in the shape of the Cole-Cole plot for each electrode configuration. The inductive loop observed in four-probe measurements is not expected from samples such as SWNT networks, and the low-frequency values of Z' are not in agreement with DC measurements. From this, it is clear that a model based on four-probe impedance spectra would not be reliable, so two-probe spectra were therefore analyzed to determine if the contributions of film elements could be distinguished, in spite of any possible contributions from the probe tips.

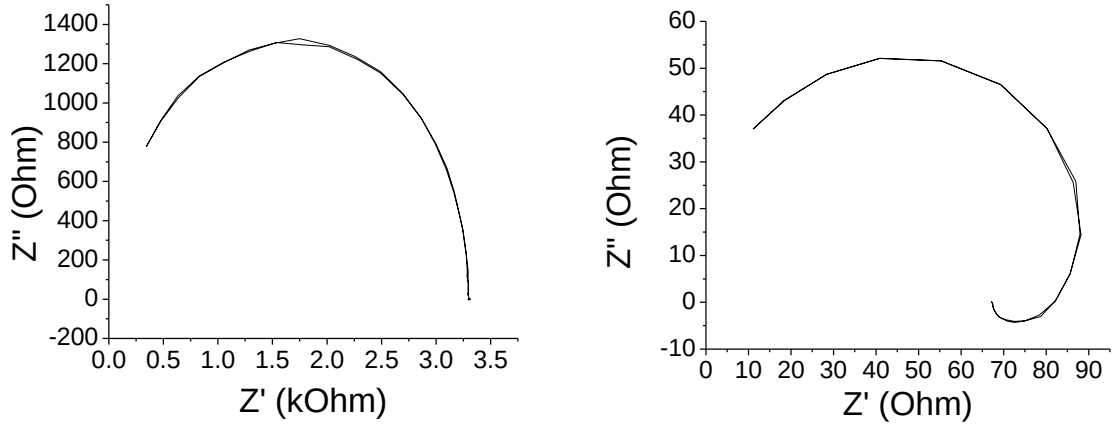

Figure 45 Two-probe (left) and four-probe (right) impedance spectra (10mV bias applied on a film with 4μg/cm^2 SWNT loading). In four-probe configuration, the low-frequency regime (right side of arc) exhibits a negative Z"arc from inductive feedback and a Z' which is lower than expected from the DC resistance results.

5.4 Two-probe impedance results

The impedance response from SWNT films are capacitive rather than inductive in nature, as the impedance trends towards zero at high frequency, a characteristic of RC circuits. It was found that impedance spectra from SWNT films were best modeled by two Voigt elements in series. A Voigt element is a capacitor and resistor in parallel (Figure 46). This model makes physical sense, as every nanotube, but also every junction or defect, serves as a resistor, and each will have its own capacitance. Calculations on single nanotube junctions show this same RC behavior, with the junction resistance inversely proportional to the nanotube contact area and the capacitance directly proportional to the area [109]. The time constant RC, is therefore always independent of the nanotube area. It is also the model favored for impedance of bulk systems, with one element interpreted as the grain boundary and the other as the bulk material [110], and RC elements have been successfully integrated into impedance models of nanotube-polymer composite systems previously [111, 112]. As discussed in chapter 5.3, a bulk material, grain

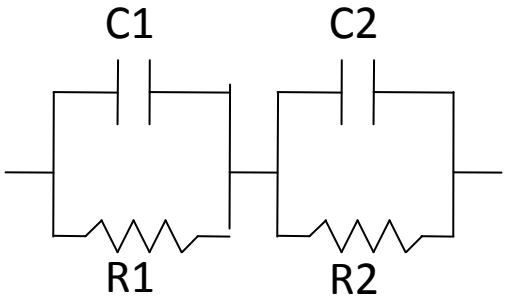

Figure 46 The double Voigt element structure fits SWNT network impedance results well, with one element interperted as inter-bundle junctions, the other as the SWNT bundles themselves.

boundary and electrode interface will each show up as separate circuit elements in the Cole-Cole plot analysis. Only two elements appear in measurements of SWNT films, so one of those three contributions must either not exist or be negligibly small. It will be demonstrated in chapters 5.5 and 5.6 that the electrode interface does not appear in the model, and instead one Voigt element arises from the SWNT bundles and the other from the SWNT junctions. While the elements of the model presented here for SWNT-only films differs from the models presented for nanotube-polymer composites [111, 112], this is in line with those impedance results, in the sense that electrode impedance does not appear in the model.

For a disordered material such as a glass or a polycrystalline solid, as opposed to an ordered system with all boundaries identical, this double-Voigt element still is valid, only the values obtained for R and C represent the mean value of the distribution of impedances for each element [110]. Here, we discuss SWNT network elements as a single time-constant system instead of as a system with a distribution of time constants; that is, as though all SWNT bundles and junctions

are identical, which is not the case. Modeling bulk samples with widely distributed microscopic impedances by only describing the average value is considered to give an adequate description of these systems. This is common for solid-state systems with distributions of phases and grain boundaries, the model which we are borrowing to describe SWNT films [110]. Any further description of the specific distributions of impedance elements is beyond the scope of this work.

The values of R and C for these two series RC circuits were found for films of different thicknesses. The Voigt elements with the lowest R values and highest R values were plotted in their own color, in Figure 47, as it was assumed that particular contribution was caused by the same property for each film. The corresponding values for capacitance were found to be symmetric, with the average capacitance constant for all loadings well above percolation threshold, 0.48 nF for both Triton X-100 and SDS. If the aforementioned $C = 1/\omega_c R$ relationship were to hold true, this constant network capacitance would mean that critical frequency and low-frequency conductivity (or four probe DC conductivity) are linearly related, which we have found to be true, and will be described in chapter 7.10.

A similar dependence on loading has been noted for critical frequency of each circuit element in our model (Figure 48). The critical frequency of both Voigt elements increases with loading. For SDS films, each f_c increases at different rates, while for Triton X-100 films, each f_c increases at the same rate.

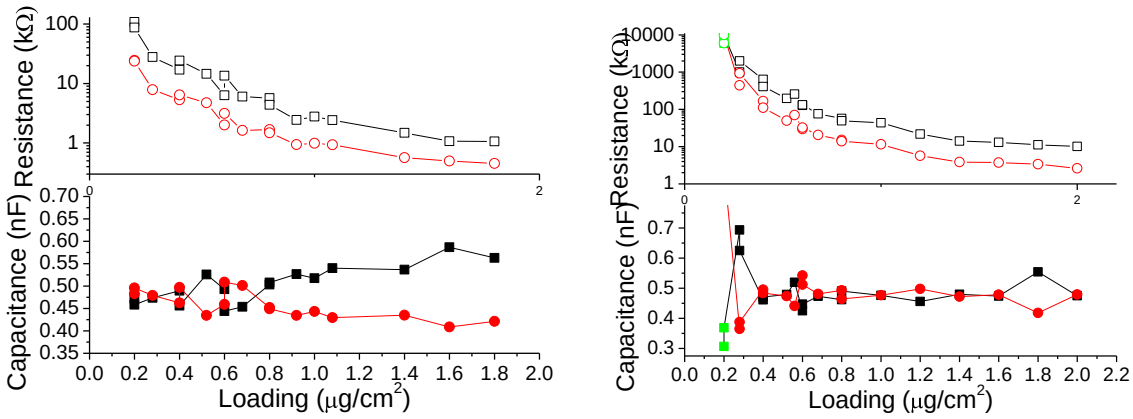

Figure 47 A series of SDS (left) and Triton X-100 (right) dispersed films, showing the results of each C and R in the double Voigt element model. Corresponding R and C elements are shown in the same color. One series of elements arises from junctions between bundles, the other from the SWNT themselves.

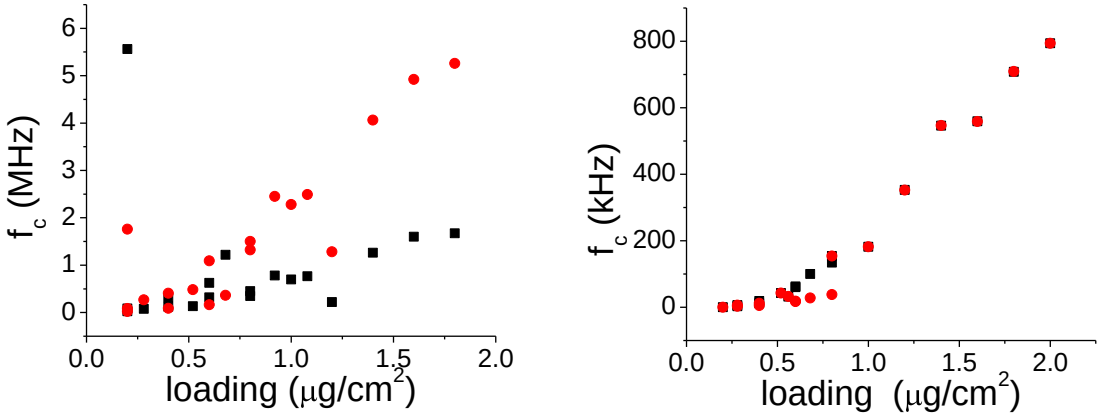

Figure 48 Critical frequencies for each voigt element in Figure 47. Triton X-100 dispersed films on the right, SDS dispersed films on the left.

For Triton X-100 dispersed SWNT, the average capacitance does have notably high values for the lowest loadings, and is constant thereafter. It is speculated that the high capacitance comes from the large spaces between SWNT and the small number of junctions in a network very close to the percolation threshold. Alternately, the capacitance could arise from contact between the probe tips and the film, with the high capacitance coming from the sparsest films with poor contact.

5.5 Tip-spacing dependence

If either of the Voigt elements in our model was due to contributions of the probe tip, then there would be no change in the values for that element as the tip spacing changed. Impedance data taken from the same setup with double the probe-tip spacing yields an overall higher impedance, as expected from point measurements taken farther apart. For the Voigt element with larger resistance, Figure 49 shows that the 2s spacing was found to have a consistently higher value of R, but the value of C showed no change. For the other Voigt element, the 2s spacing had a higher capacitance, but only a higher resistance for lower loadings, with the 2s value of R becoming inexplicably lower than the 1s R for loadings above 1.4 $\mu g/cm^2$. The average capacitance of the two Voigt elements was still invariant of thickness for the 2s probe spacing. The value was higher, though: 0.51 nF, instead of 0.48 nF.

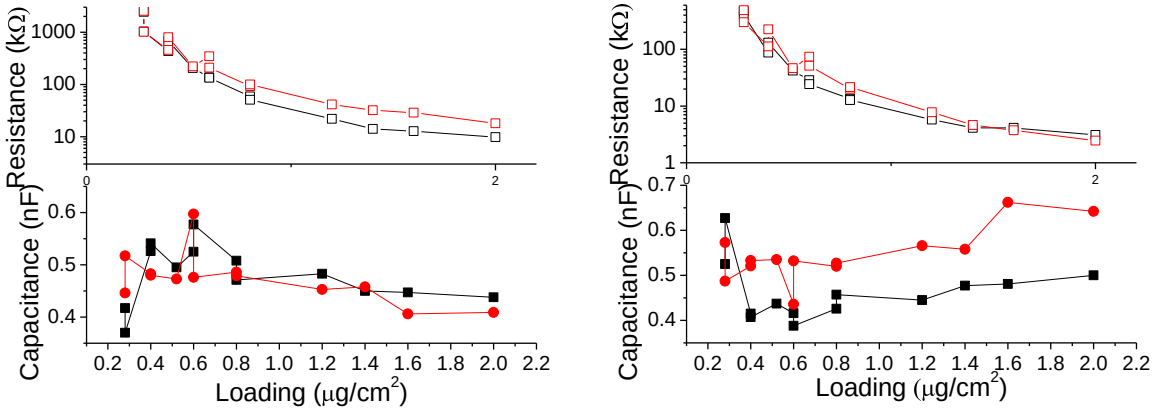

Figure 49 R and C for each Voigt element for Triton X-100 dispersed films, showing how each element changes with two different probe tip separations. Red is 2s tip spacing, black is 1s tip spacing.

Theory predicts that the measured resistance of a thin film between two point terminals should increase by a factor of 1/ln2=1.44 with a doubling of the distance between the tips (see equation 2.5). Upon doubling the tip spacing, the resistance of the first (larger resistance) Voigt element increased by a factor of 1.47, on average, and the resistance of the second (smaller resistance) element increased by a factor of 1.49 on average, excluding the two highest loading points where the inexplicable crossover of resistance between spacings was observed (Figure 49). The overall network resistance between the two spacings was found to differ by a factor of 1.49. The small difference between theory and experiment can be easily accounted for by differences in the contacts between sets of probes. If either of the modeled RC elements were due to the probe-film contact, that element would have values independent of tip spacing. Since all values increase with tip spacing, the RC elements are due to contributions of the film itself, rather than contributions of the probes.

5.6 Effect of doping on frequency dependent impedance

For doped films of the similar thickness and method of preparation, the relation between critical frequency and low frequency (DC) conductivity also exhibits a linear dependence (Figure 50). The position on the line depends on the degree of doping, and can be determined based on choice of dopant and method of doping. This means that, just like conductivity can be selectively determined by doping, so can f_c. In-situ control of f_c during doping would also be possible by monitoring DC conductivity, which is experimentally much more easily determined in real time, as a sweep of many frequencies is not necessary.

The model applied to undoped films is still valid for doped films. The equivalent circuit model of chapter 5.2 has been applied to the doped films of Figure 50 as well, and the results are shown in Table 3. As before, one R and C combination arises from the SWNT bundles, while the other element describes the junctions between bundles. When analyzing these circuits, it is important to note that while for each individual doping, the R_n and C_n values correspond to one another, each R_n and C_n does not necessarily correspond between samples. That is, if the C_1 from the undoped sample is due to nanotube junctions, the C_1 value from the HNO_3 doped sample still could be from the junctions or from the SWNT bundles. However, if the C_1 from the undoped sample is due the junctions, then the R_1 from the undoped sample must be due to the junctions as well. Since the model assigns each R_n and C_n arbitrarily between samples, to determine the effects of a dopant on the individual circuit elements, one must use other information aside from the element values alone.

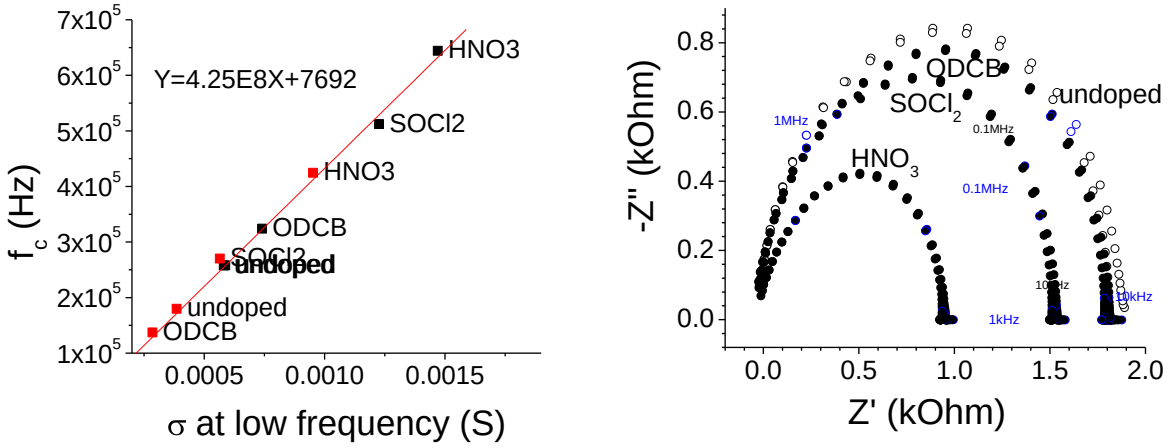

Figure 50 Left: the dependence of critical frequency on low frequency admittance (DC conductivity). Vapor-doped are shown in red, liquid-doped in black. Right: Nyquist plot of SWNT films with exposure to the vapor of various dopants.

Table 3 Values of RC circuit elements for different dopants, arrived at by modeling Figure 50.

undoped	Value	% error
C_1 (junction)	724(pF)	0.79384
C_2 (SWNT)	331(pF)	0.66566
R_1 (junction)	988.38(Ω)	0.73036
R_2 (SWNT)	872.98(Ω)	0.49034
$SOCl_2$	Value	% error
C_1 (junction)	537(pF)	13.833
C_2 (SWNT)	349(pF)	12.095
R_1 (junction)	988.63(Ω)	1.5139
R_2 (SWNT)	572.63(Ω)	2.3396

ODCB	value	% error
C_1 (SWNT)	306(pF)	1.1337
C_2 (junction)	980(pF)	1.5752
R_1 (SWNT)	925.16(Ω)	0.55779
R_2 (junction)	910.32(Ω)	0.92567
HNO_3	value	% error
C_1 (junction)	811(pF)	0.99251
C_2 (SWNT)	530(pF)	2.5056
R_1 (junction)	688.43(Ω)	0.53673
R_2 (SWNT)	273.93(Ω)	0.72701

For doping with $SOCl_2$, there are two possibilities as to what happens to each element upon doping: The value of one resistance element remains unchanged, and one falls to 66% of the original value; or the value of one resistance element rises by 13%, and the other falls to 58% of the original value. The first option is more believable for several reasons. First, it is hard to believe that the same value would arise in two circuit elements before and after doping, unless they arise from the same element of the network. Also further analysis of this dopant and other dopants will show that the undoped R_1 value is from the junctions and that the undoped R_2 must be due to the SWNT bundles.

From the S_{11} band quelching in the absorbance data as described in chapter 6.2, the SWNT resistance would have to fall upon doping. Thus, the higher value (undoped R_1) must be the junction resistance, since the undoped R_2 value is the only value that falls upon $SOCl_2$ doping. If the elements corresponded to one another in the case where one value fell and the other rose, it would have been the undoped R_2 value that rose. Note that, for both the undoped and $SOCl_2$ doped samples, the C_1 values also have higher capacitance than the C_2 values, which one would expect from a junction between two objects, where the objects might not be in perfect contact with one another.

In the case of ODCB doping, it is clear that for the two RC elements, one value of resistance rises, and the other falls. From the unchanged absorbance spectrum upon doping, this would mean that the value of the junction resistance is the value that falls, which reinforces the idea that the undoped R_1 value is the value of junction resistance. It is less clear which of the doped values corresponds to which undoped value. In fact, the ODCB doped R_1 and R_2 values fall

within the same range, given the percent errors on each value. The C_1 and C_2 values for the two ODCB doped circuit elements are different, though. If the major effect of ODCB doping is on junctions, with little effect on the bundles, then the ODCB-doped C_1 value must correspond to the undoped C_2 value, and be due to the SWNT bundles. This means the ODCB-doped C_2 must correspond to the capacitance of the junctions. The higher field localized at the junctions as suggested by Blackburn[33] would also result in the increased capacitance as observed here.

The HNO_3 doping was the only case where the resistance of both circuit elements fell, indicating a lowering of the resistance of both the junctions and of the SWNT themselves. Again, from the resistance of each element alone, it is not clear which HNO_3-doped R_1 and R_2 correspond to the junctions and SWNT. But by reasoning of the increased capacitance of junctions upon doping used in the previous paragraphs, the HNO_3-doped C_1 (and therefore R_1) must correspond to the junctions. This conclusion is also the only conclusion that makes sense in terms of absorbance band suppression, in that the S_{11} band was removed to a lower absorbance for HNO_3 doping than for $SOCl_2$ doping, which means the HNO_3-doped SWNT should have a lower resistance than $SOCl_2$-doped SWNT. The $SOCl_2$-doped R_2 values correspond to the SWNT, and the HNO_3-doped R_2 is the only HNO_3-doped element value lower than the $SOCl_2$-doped R_2, and must be due to the SWNT also. This means a raised capacitance for both the HNO_3-doped junctions and SWNT over the undoped capacitances. $SOCl_2$-doped junctions and ODCB doped SWNT (C_1 value) are the only circuit elements which show a lower capacitance than the undoped elements, which are also the only elements which did not exhibit a lowering of resistance upon doping.

This contradicts the finding of Geng [22], where the dopant was purported to remove insulating SDS layers and promote transport at junctions, rather than doping the SWNT themselves. This is not surprising, due to the care which was taken to remove SDS on our films prior to doping, with our results agreeing with the more common findings that the chemical doping occurs on SWNT sidewalls [34, 113], in addition to the finding that it increases junction conductivity as well.

5.7 Conclusions

We have found an experimental relationship between two-probe and four-probe measurements that is universal among SWNT films, irregardless of dispersion method or of film thickness. This two probe resistance is 12% higher than expected from calculations, due to the constriction resistance of the probe tips. This 12% difference is dependent on the tips used, and would have to be recalculated for any new experimental setup. This relation allows two-probe spreading resistance measurements to be used to calculate sheet resistance, in spite of contributions from the electrode resistances, without performing additional four-probe measurements.

Two-probe measurements have been shown to be preferable over four-probe measurements for AC impedance spectroscopy of SWNT films. We have proposed a model for separating the resistances of junctions from the bundles themselves, which is also the traditional model used for describing grain boundaries in disordered solids and polycrystalline materials. This circuit model consists of two Voigt elements, one corresponding to transport along the SWNT bundles, another from transport through junctions. The contact resistance does not explicitly appear in this model, despite measurements being done in a two-probe configuration, due to the relatively small contribution of the electrode to the overall impedance. This is confirmed by measurements

taken at different probe spacings, in which each model element show the impedance changes expected from voltage being applied over a larger area of the network, without probe-tip resistance contributions. Also, the comparison between two-probe and four-probe measurements show a constant constriction resistance for all film thicknesses, and since a constant resistance element does not appear in the model, this is further confirmation of the lack of a probe-tip contribution to the impedance spectra.

This model was applied to networks of a single thickness with the dopants HNO_3, $SOCl_2$ and ODCB applied. The measurements on doped networks not only allowed us to determine which circuit element contribution was from the SWNT and which was from the junctions, but also allowed us to separate the effect of doping on the SWNT from the effect of doping on the junctions. For an undoped film, the higher resistance element was found to be due to the junctions between SWNT, while the lower resistance element is due to the SWNT bundles. HNO_3 was found to raise conductivity of the junctions and SWNT, while $SOCl_2$ raised conductivity of the SWNT only. Most interestingly, ODCB increased conductivity at the junctions, but decreased conductivity of the SWNT.

It was found that the critical frequency of a SWNT network can be varied by changing the degree of doping of the network. For a given network, the critical frequency and doped sheet resistance are linearly related, and therefore depend only on the degree of doping, rather than the doping itself. In situ control of doping, as mentioned in chapter 6, could then be applied to controlling the critical frequency of SWNT film of given thickness or transmittance, which would be useful in making frequency dependent devices from a SWNT network. Critical

frequency is also shown to depend on SWNT loading, which is more thoroughly discussed in chapter 7.10.

CHAPTER 6 RESULTS OF DOPING

6.1 Experimental Approach

We have investigated many chemical dopants for their ability to alter the conductivity of SWNT. Rather than attempting to dope the SWNT in their as-grown state or while dispersed in solution, we have chosen to dope the SWNT after their formation into a film. The method of doping used is simply immersion of the completed film in the dopant, or exposure to the dopant's vapors by temporarily enclosing the film in close proximity to the liquid dopant. We have found these methods to be preferable for their ease of use and repeatability. The degree of bundling and dispersion, SWNT purity, or other variations in the network morphology could arise from making a film out of pre-doped material. So most importantly, the approach of doping the SWNT after preparation as a film allows us to investigate the dopant's effects on SWNT properties independent of any changes to network morphology. Once the film is formed, the geometry of the SWNT network cannot be altered by exposure to the dopant, so any change in film properties must be due only to a change in the transport properties of the SWNT themselves.

SWNT films have been prepared by different methods of dispersion and of different thicknesses, and doped by exposure to HNO_3 [22, 24, 113-123], $SOCl_2$ [22, 34, 37, 119], and ortho-dichlorobenzene (ODCB), as described in chapter 1.6. Exposure to both liquid and vapor phases of these chemicals have been the most successful of the dopants investigated. The amount of time that the films were exposed to the dopants does not change the degree of doping, with exposure times of a minute to a few hours showing the same resistance change.

6.2 Effect of doping on the absorbance spectrum

The dopants studied have not altered the film transparency in the visible spectrum. The first semiconducting transition in the absorbance spectrum has been quelched in the doped samples, with the degree of suppression increasing with the effectiveness of the dopant. Figure 51 demonstrates that a smaller lowering of the second semiconducting transition occurs with greater levels of doping, with little observed change in the metallic band. This indicates that the dopants are changing the conductivity of the semiconducting tubes. This effect has been attributed to the filling of the DOS by a change in Fermi-level, with the low-energy transitions filling first, then higher energy transitions filling with a greater degree of doping [24, 34, 113, 116, 118, 120, 122].

Exposure to the liquid and vapors of ODCB, $SOCl_2$ and HNO_3 all cause an increase in conductivity of SWNT films. These chemicals affect the films by changing the conductivity of the semiconducting tubes. This is evidenced by the suppression of the semiconducting bands in the absorbance spectra, especially the S_{11} band. The degree of doping of the s-SWNTs determines the post-doping intensity of both semiconducting peaks, with the stronger dopants showing suppression of both peaks, and the weaker dopants showing suppression of just the first semiconducting transition.

The degree of suppression of the S_{11} ($5834cm^{-1}$) band was found to be directly related to the change in resistance upon doping, as seen in Figure 52. The ratio of undoped to doped film resistance is linearly proportional to the ratio of the S_{11} intensities of the undoped and doped

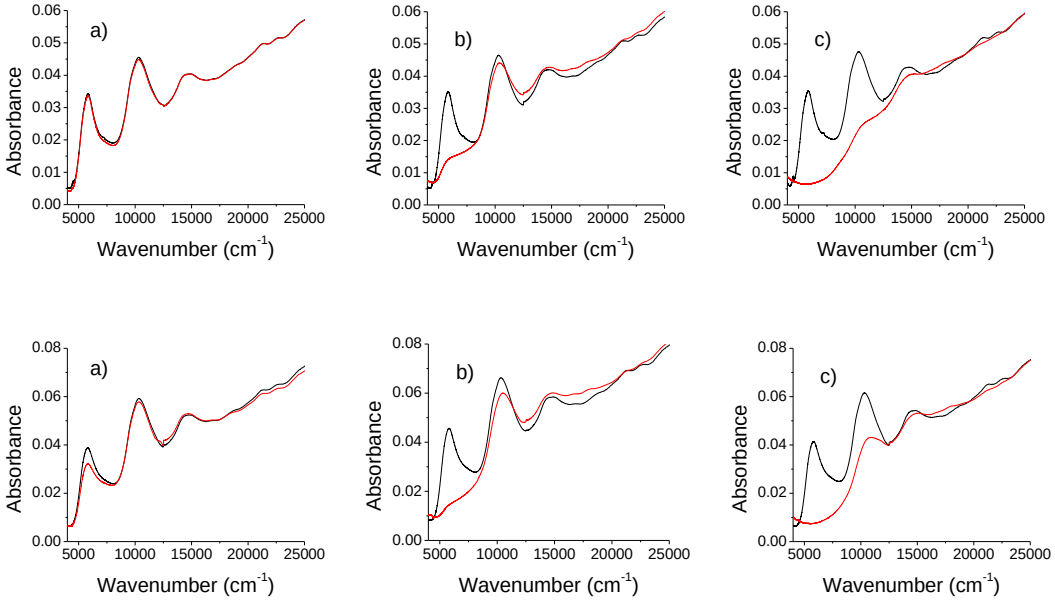

Figure 51 The effect of dopants on the optical absorbance of SDS-dispersed SWNT films. Films were treated by exposure to vapors of the dopant (top) and by immersion in the liquid doapnt (bottom). Each dopant causes different degrees of suppression of the semiconducting transition bands, which corresponds to the change in film resistivity. a) ODCB b) $SOCl_2$ c) HNO_3

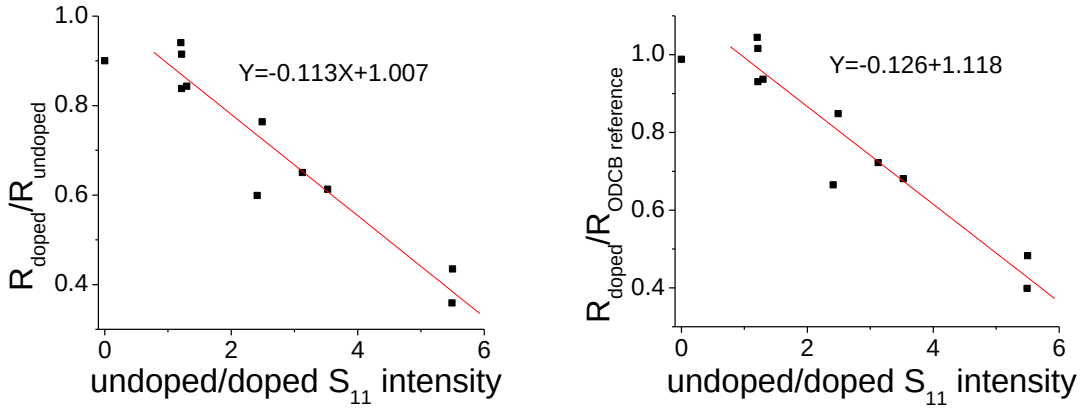

Figure 52 The fractional change in resistance is linearly dependent on the fractional change in intensity of the 5834cm^{-1} absorbance transition. Left plot is SDS dispersed film doped by exposure to various dopants in both liquid and vapor phases. All dopants fall on the same line. Right is the same data, only replacing the reference resistance (resistance with unsuppressed S_{11} band) with the resistance obtained from ODCB vapor doping, where no S_{11} suppression is observed.

films. This relation is independent of the dopant used, and depends only on the degree of doping.

This relationship is important, as it can be used to predict the expected change in conductivity given a change in absorbance. During the doping process, it is easy for films to become damaged, and things like scratches and microscopic tears can cause enough discontinuity in the film to raise resistance, but will not show up on the absorbance spectrum. Similarly, poor electrical connections between measurements would also be evident as significant deviations from the above plot. Most importantly, any dopants which cause a resistance change, but do not suppress the S_{11} band to the predicted amount, must affect that change by a mechanism other than increasing semiconducting SWNT conductivity. Additional mechanisms would include changing the resistance at junctions between tubes, changing the resistance of metallic SWNTs, or adding new connections between SWNT in the network.

Note that when the ratio of doped and undoped S_{11} transitions is unity, the predicted ratio of resistances is less than one (0.89). This means that the mechanism of doping can drop resistance to a degree without any change in the S_{11} band. This effect has been noted on some of our ODCB doped films (see Figure 51a). One possibility is that the dopants cause a conductivity change by a mechanism other than increasing transport through semiconducting-SWNTs. Also, the S_{11} band is already suppressed is SDS dispersed films, so the mildest dopings are not noticeable in the absorbance spectrum, which is supported by the absorbance effects due to heat treatment of films, as discussed in chapter 6.4. A SDS film vapor-doped with ODCB can exhibit a change in conductivity of a factor of 1.11 without any suppression of the S_{11} band. This

factor change in resistance is applied in Figure 52, and the linear fit of the data intersects the point (1,1) exactly, just as expected for a linear dependence of resistance on S_{11} intensity.

6.3 Effect of a single dopant on films prepared with different dispersants

A series of films was made with purified SWNT in three different dispersants: Triton X-100, SDS, and ODCB. Each set of films was prepared from a 2 μg/ml solution, in thicknesses ranging from 0.4μg/cm^2 to 3.2 μg/cm^2. Despite having the same range of SWNT densities, the range of transmittances for each dispersant was different (Figure 53). ODCB had the lowest transmittances, ranging from 46 to 91 %T. SDS was the highest, ranging from 70 to 99 %T, with Triton X-100 having a range of 62 to 93 %T. In the case of ODCB, sonopolymerization of the solvent onto the SWNT accounted for the low transmittances, and this is evident from the dependence of absorbance on sonication time (see chapter 3.4). It is possible incomplete dispersion accounted for much of the difference between transmittances of Triton X-100 and SDS dispersed samples.

Each of these films was doped by immersion in $SOCl_2$. The dopant dropped the resistance by a multiplicative factor. The factor was independent of film thickness but dependent on dispersant. Resistance fell by a factor of 6±1.0, 19±1.5, and 3±0.3 for ODCB, Triton X-100, and SDS dispersed films, respectively. Interestingly, the doped resistances, as a function of transmittance, were the same for all dispersants (Figure 54). As a function of loading, this trend was not observed.

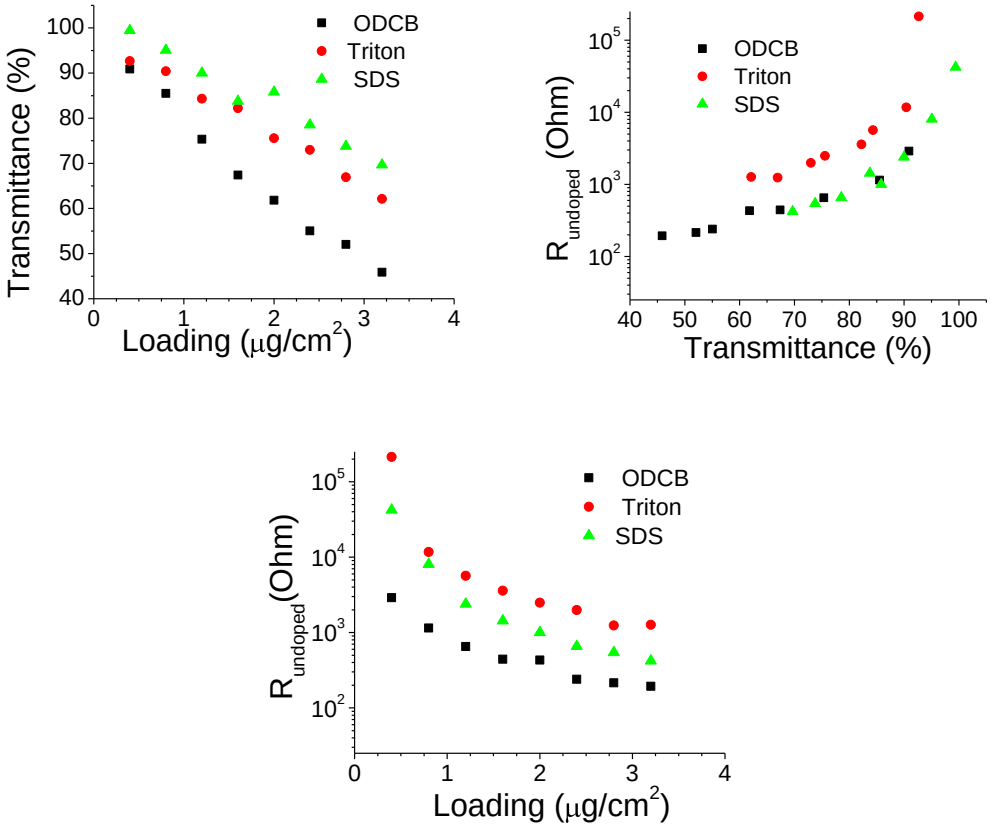

Figure 53 Transmittances and sheet resistances at given loading for SWNT films prepared by different dispersions.

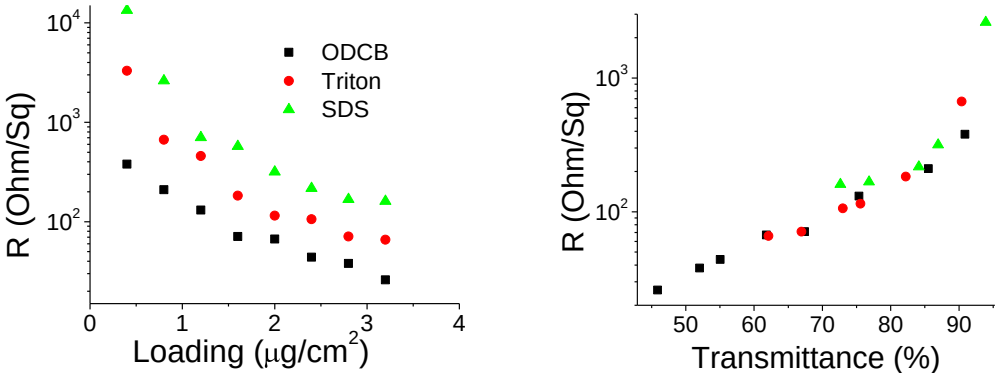

Figure 54 Films dispersed in Triton X-100, SDS, and ODCB which have been doped by immersion in $SOCl_2$. Despite having different values of resistance before doping, the dopant brings films of the same transmittance to the same level of resistance, independent of dispersant.

For films of the same visible-spectrum (550nm) transmittance, the transitions show different magnitudes, dependent upon dispersant (Figure 55). In the case of ODCB dispersed SWNT, the intensity of the S_{11} transition is certainly affected by the doping mechanism we have explored earlier. In the case of SDS dispersed SWNT, the same surfactant binding to tube walls that causes better dispersion is likely also the cause of the smaller S_{11} intensity. The S_{11} intensity of Triton X-100 dispersed films is 2.3±0.6 times higher than SDS dispersed films.

Despite each dispersant having notably different absorbance spectrums, the level of S_{11} suppression upon doping was found to be dependent only upon the dopant used, and not upon the method of dispersion. Films of a given visible-spectrum transmittance may have different S_{11} intensities which depend on the dispersant used to make the film. However, upon exposure to a given dopant, the S_{11} intensity changes to the same level for all dispersants (Figure 56).

6.4 Suppression of the S_{11} band in SDS dispersed SWNT

The idea that bound surfactant is causing the S_{11} suppression in SDS films can be tested by heating the films in inert gas to a temperature which will remove the surfactant but not the SWNT. Thermogravitational analysis (TGA) of SDS surfactant, of the cellulose nitrate filters used to prepare the films, and of SWNT shows that under inert gas, the SDS burns completely by 350C, before the SWNT begin to burn off (Figure 57). This means that baking a SDS-dispersed film at 350C will remove any residual filter and surfactant without removing the SWNT.

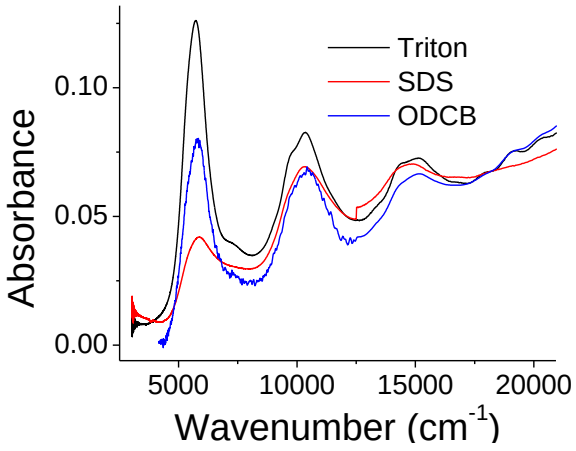

Figure 55 Relative intensities of absorbance transitions from different dispersants. For this set of films, the S_{11} transitions for Triton X-100 and ODCB films is 2.5 and 1.6 times higher than for SDS films.

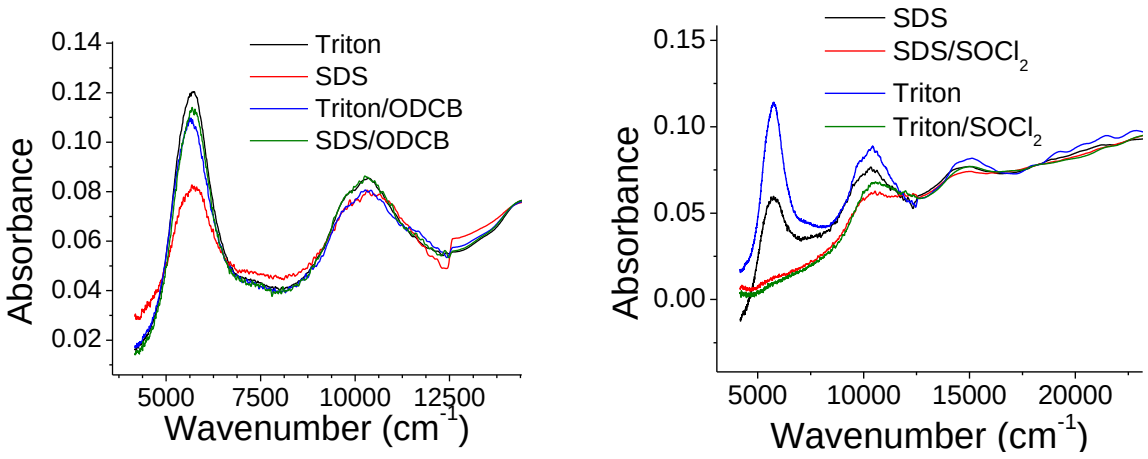

Figure 56 Doping in ODCB (a) and $SOCl_2$ (b) brings the S_{11} intensities to the same level for both SDS and Triton X-100 dispersed films.

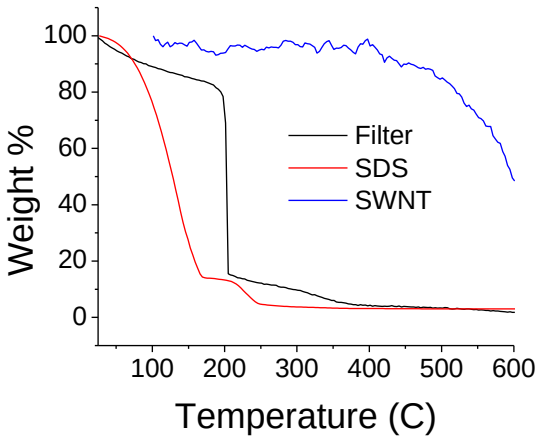

Figure 57 SDS, filter, and SWNT burn temperatures under inert gas. Before 400C all of the filter material and surfactant is removed, but the SWNT remain.

Baking has demonstrated that any residual filter or surfactant remaining after washing and dissolving does not affect the conductivity of the films or change the visible spectrum transmittance. It does however enhance the S_{11} band (Figure 58). The S_{11} enhancement must be due to removal of small amounts of remaining surfactant from the film. The fact that no change in conductivity occurred could be indicative of either a film dominated by transport through metallic nanotubes, or due to the bound surfactant causing a suppression of the optical transition that does not affect the conductivity of the semiconducting SWNT.

6.5 Treatment by more than one dopant

It was found that treatment by multiple dopants changes the resistance only to the level of the stronger dopant. Shown here are results from two Triton X-100 dispersed films with 66 %T. Both measured 1.6 kΩ/Sq before doping (Figure 59). One was doped by immersion in HNO_3 at a temperature of 65C, and then by subsequent immersion in $SOCl_2$ at 45C. The resultant resistances were 480 Ω/Sq and 180 Ω/Sq, respectively. The second was immersed in $SOCl_2$ at

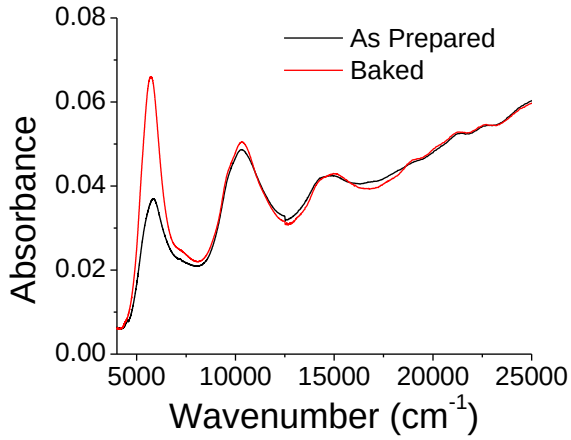

Figure 58 Before and after baking at 350C, the film is 91%T at 550nm and has sheet resistance of 1270Ω/sq. After baking, the S_{11} transition is enhanced by a factor of 1.7 despite exhibiting no change in resistance, due to either the removal of residual surfactant or filter material.

45C only, with a resultant resistance of 150 Ω/Sq. Despite having similar post-doped resistances, the doping from both chemicals suppressed the S_{11} band more than the doping from either of the dopants alone (Figure 59).

6.6 De-doping and re-doping

The degree of doping was found to decrease as time elapsed from the doping of the sample (Figure 60). The resistance of a series of Triton X-100 dispersed films dropped by a factor of 18 upon doping with $SOCl_2$. One month after doping, the resistance was found to be only a factor of 6.6 lower than the undoped resistance, and three months later was found to be a factor of 3.9 lower than the undoped resistance. At that time re-submersion in $SOCl_2$ was able to bring the resistance back to a factor of 6.7 lower than the undoped resistance. This means that a SWNT film can be re-doped, only not to the degree of original doping. Similarly, the resistance of an

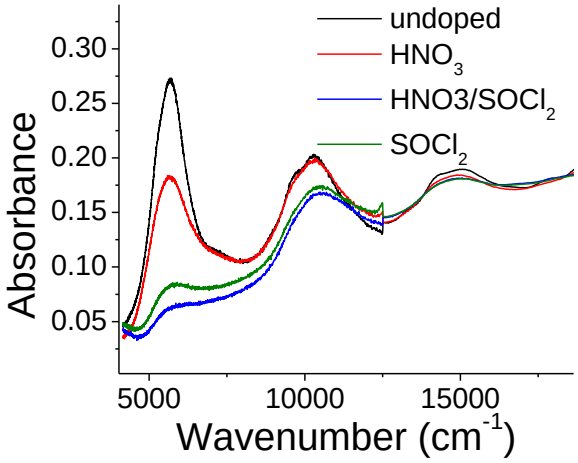

Figure 59 change in absorbance spectra from multiple dopants. The S_{11} peak was 68% ad 31% of the undoped film for exposure to HNO_3 and $SOCl_2$, respectively. After exposure to both dopants, the S_{11} peak was 23% of the original height.

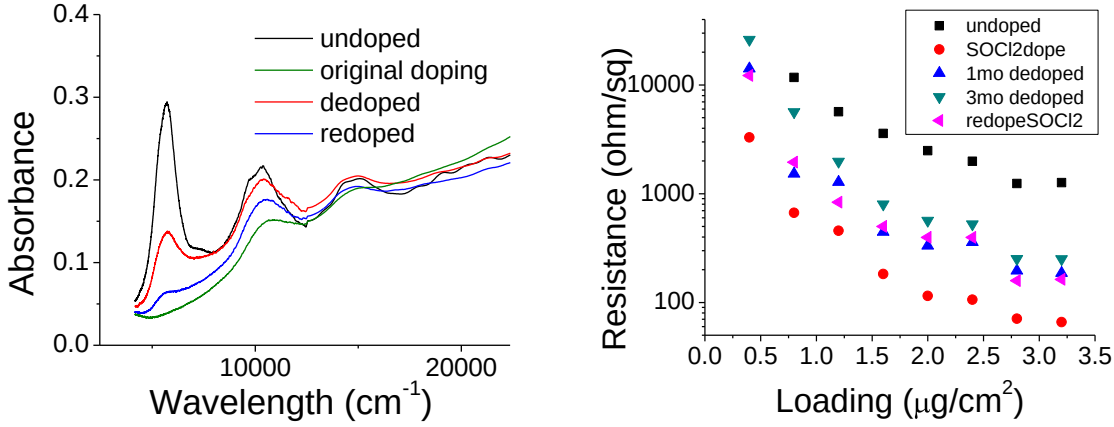

Figure 60 Absorbance and resistance trends upon doping, de-doping and re-doping of SWNT films. There is a loss in the degree of doping as time progresses after the original doping. The film can be re-doped, but not to the same degree as the original doping.

ODCB dispersed film drops by a factor of 6.0 upon $SOCl_2$ doping, and one month later returns to a resistance that is only a factor of 1.8 lower than the undoped film. Interestingly, for both dispersants, the films de-doped at the same rate, with resistance increasing by a factor of 3.0 from the original level of doping after one month.

Figure 60 shows that absorbance follows the expected trend from such resistance behavior, with the semiconducting transitions being most suppressed immediately following the doping, returning as the sample becomes de-doped, and then falling again upon re-doping. The re-doping drops the S_{11} peak to a level intermediate of the original doping and the de-doped film. The peak is a factor of 3.5 higher than the level of suppression observed at the time of the original doping, corresponding to a factor of 3.0 change in resistance. Similarly, the re-doped film has a S_{11} magnitude a factor 1.6 higher than the originally doped film, corresponding to the factor of 1.8 change in resistance.

Doping has been attributed to the intercalation of dopant molecules between bundles, or to the absorption of dopant molecules onto defects in nanotube sidewalls [34, 113, 116]. Such defects can be induced by the dopants themselves, as the dopants are strong oxidizers [114, 115]. The observed de-doping is attributable to desorption of the dopants from the nanotubes. The fact that the de-doped films do not return to their original high resistance even after three months is simply due to the rate of desorption of the dopants, with some of the doping still remaining. The fact that the re-doped films do not return to the lower resistance attained after the original doping is harder to understand. If, indeed, the dopants cause defects to be induced onto the SWNT sidewalls, and upon re-doping, the dopants do not fill all of the defects induced by the original

doping, then those defects could be detracting from the overall conductivity. Also, if the intercalated dopant molecules do indeed spread apart the bundles [113], then inter-tube transport could be reduced when the dopants desorb, negatively affecting the re-doped conductivity.

6.7 Comparison of transport between metallic and doped semiconducting SWNT

From the absorbance data, it is clear that the dopants, at a minimum, serve the purpose to increase the conductivity of semiconducting tubes. Even with many efforts to separate semiconducting from metallic SWNT [13, 33, 119, 124-126], the question remains: is a film more conductive if composed of metallic SWNT or doped semiconducting SWNT?

Taking a simplistic view on the makeup of a nanotube film, the resistivity of a film, R_{film}, can be considered to be comprised of parallel metallic and semiconducting components, such that

$$1/R_{film} = 1/R_S + 1/R_M \tag{6.1}$$

where R_S and R_M are the semiconducting and metallic contributions. Doping of the semiconducting tubes leads to a new, lower, resistance. This new, doped resistance, R_D, is a fraction of the original resistance

$$fR_{film} = R_D \tag{6.2}$$

The doped semiconducting resistance, R_{SD}, is therefore related to the original resistance by

$$1/R_D = 1/fR_{film} = 1/R_{SD} + 1/R_M \tag{6.3}$$

The resistances of metallic and doped and undoped semiconducting SWNT can therefore be related by

$$(f^{-1} - 1) + R_M / fR_S = R_M / R_{SD} \tag{6.4}$$

So if the average resistance of metallic and of semiconducting SWNT is known, the measured resistance change due to a given dopant will tell if the doped semiconducting SWNT are more conducting than the metallic SWNT.

This relation is for the overall contribution of semiconducting and metallic SWNT in a given film. It does not take into account the 2:1 ratio of semiconducting to metallic tubes. To find out if the individual, typical doped semiconducting SWNT is more conductive than the individual typical metallic SWNT, not only must $R_M / R_{SD} > 1$ hold true, but $R_M / R_{SD} > 2$ would have to be satisfied as well. If this condition is met, then a film composed of doped semiconducting SWNT would be more conductive than a film of metallic SWNT.

From the previous studies examined in the introduction, the resistances of semiconducting and metallic SWNT lie in the range of 160-500kΩ and 13-40kΩ, respectively. We can therefore assume $R_M / R_S \approx 0.1$. This means that if $f < 0.54$, then $R_M / R_{SD} > 1$, and if $f < 0.36$, then $R_M / R_{SD} > 2$. Of the dopants we have studied, while $SOCl_2$ and HNO_3 have $f < 0.54$, Chlorosulfonic Acid is the only chemical that gives a fractional resistance change that meets the requirement $f < 0.36$. So by the above reasoning, CSA is the only dopant strong enough to bring a film of semiconducting SWNT to the same conductivity as a film of metallic SWNT.

These calculations do not take into account any possible increase in metallic SWNT conductivity from doping, as it assumes all conductivity change is due to doping of semiconducting SWNT. However, the conclusion reached still holds, as a metallic SWNT conductivity increase would

only mean that semiconducting SWNT have less of a conductivity increase than calculated, so doped semiconducting SWNT are still less conductive than metallic SWNT, with or without any possible effect from the dopant.

6.8 Raman Spectroscopy of doped SWNT

The response of Raman signal to SWNT dopants has also been investigated. A RBM blueshift from both p and n doping has been previously observed by Kavan, attributing the shift in p-doped tubes as a sign of a hole being introduced into the π-band, and also due to the breaking of van der Waals force between tube bundles [127, 128]. The disappearing of the BWF lineshape, characteristic of highly mobile electrons and therefore a sign of metallic tubes, is due to hole-filling of the metallic valence band [127], resulting in a Lorentzian lineshape.

Raman data was taken at an excitation wavelength of 633nm, which from the Kataura plot of Figure 9, excites metallic SWNT. Any change in Raman spectra upon doping is due to a change in the Fermi level of metallic nanotubes. Our doping has shown a blueshift of the G-band and D*-band, corresponding to a lowering of the Fermi level. The RBM was unshifted. In addition, there is a narrowing of the G-band. Our observed blueshift of the G-band confirms that hole doping should always blueshift the spectrum, as others have cited [118, 127].

For films made with SDS as a dispersant in Figure 61, doping with ODCB causes no change in the shape of the Raman spectra for the G, RBM, or D* bands, except for a small decrease in the D* intensity for the sample that was exposed to its vapor. The other dopants, HNO_3 and $SOCl_2$, shifted the G and D* band to higher wavenumber, and narrowed the G-band. The G-band was

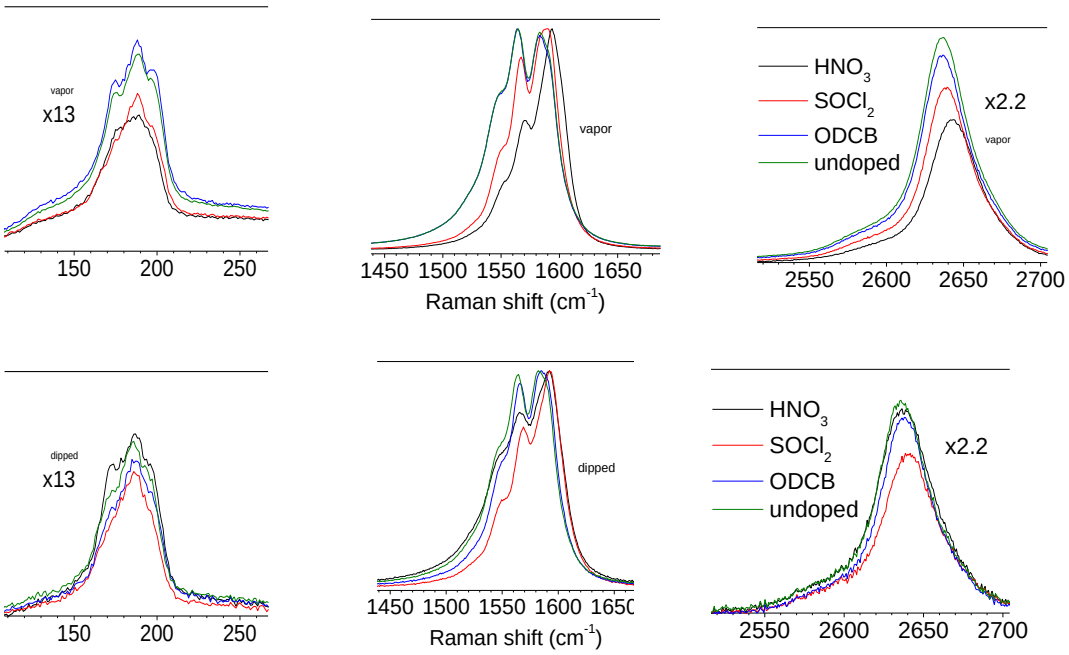

Figure 61 Raman spectra change of SDS-dispersed SWNT films upon exposure to vapor-phase (top) and liquid-phase (bottom) dopants.

narrowed by an equal amount with $SOCl_2$ for immersion and vapor exposure, but only narrowed for HNO_3 for vapor exposure, although it was still shifted.

Doping of a Triton X-100 and a SDS film with $SOCl_2$ brings the G-band to the same shape and position, dependent on the dopant and independent of the dispersant, similar to the effect on the absorbance bands. ODCB doping is different, in that it has only a small narrowing of the Raman peaks, and does not bring them to the same position. Its effect is therefore dependent on dispersant, unlike the other dopants studied (see Figure 62). The RBM intensity was lowered for both these dopants, but no shift was observed. The G-band shift does correspond to the change in film resistance as is shown in Table 4.

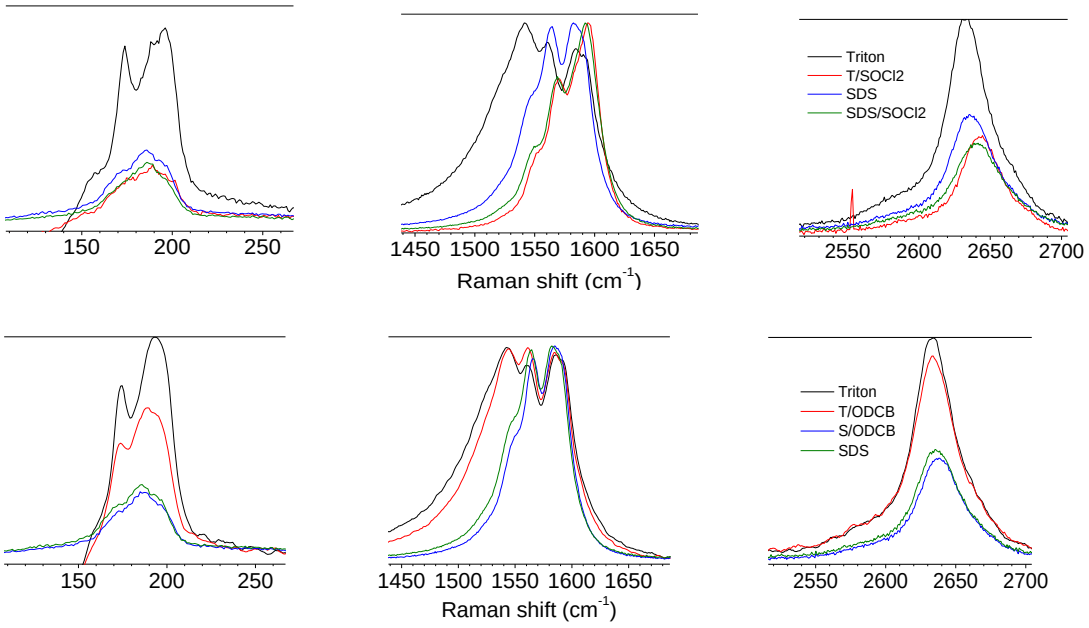

Figure 62 Raman spectra of Triton X-100 and SDS dispersed films upon exposure to the liquid phase dopants $SOCl_2$ (top) and ODCB (bottom).

Table 4 G-band shifts and corresponding resistance changes for SDS-dispersed films exposed to liquid and vapor phases of various dopants.

Vapor exposure	G (cm^{-1}) position	G (cm^{-1}) shift
HNO_3	1594	11
$SOCl_2$	1590	7
ODCB	1583	0
undoped	1583	

Vapor exposure	R (ohm/sq) undoped	R (ohm/sq) doped	%change in R
HNO_3	1159	416	64
$SOCl_2$	1295	989	24
ODCB	1316	1185	10

Liquid exposure	G (cm^{-1}) position	G (cm^{-1}) shift
HNO_3	1592	9
$SOCl_2$	1592	9
ODCB	1584	1
undoped	1583	

Liquid exposure	R (ohm/sq) undoped	R (ohm/sq) doped	%change in R
HNO_3	674	293	57
$SOCl_2$	638	415	35
ODCB	775	729	6

The vapor-doped films have a lowering of the RBM that has been previously observed with the addition of donor molecules to the SWNT but the liquid-doped films show no such trend. The reason for this difference in doping method is unknown, although the rise of the RBM upon doping also corresponds to a widening of the G-band, whereas a narrow G-band is related to metallic (highly conductive) behavior [129].

The shifting of the G-band to higher wavenumber is indicative of p-doping of the SWNT[37, 118, 129, 130], whereas the opposite effect results from n-doping [129, 131]. The fact that ODCB can increase conductivity without introducing a significant shift of the G-band has been attributed to the weak interaction of ODCB with the SWNT sidewalls [132]. This is consistent with the threshold behavior that has been previously reported [37], where hole doping can increase the conductivity up to a certain point without changing the G-band position, at which point a significant position change is observed. For different exposures to HNO_3 and $SOCl_2$, the shift of the G-band is not strictly related to the conductivity change as has been reported by others [37, 133]. This is likely due to the numerous things that affect the G-band position, such as nanotube-surfactant interactions, hole addition to the nanotube sidewalls, and spacings between SWNT in a bundle. For example, in the case of intercalation of dopant molecules inside of bundles, the additional space created between the SWNT will cause an upshift of the G-band, which could be differently related to conductivity than from an upshift incurred by addition of the molecule into a SWNT sidewall. This spreading apart of bundles by dopant intercalation has previously been associated with a RBM shift to lower wavenumber, and no RBM shifting has been observed in our films [134]. These conflicting findings demonstrate that Raman

spectroscopy is not as sensitive a tool to determine SWNT charge transport (and therefore film conductivity) as absorbance spectroscopy.

6.9 Change in Raman spectra from baking of an SDS-dispersed film

It was found that baking at 350C decreases the G/D ratio, although, as Figure 63 shows, it does not alter the conductivity or transmittance of the films. This was surprising, as it shows that tube defects, as measured by G/D ratio, is not alone a significant indicator of conductivity in our films. If G/D ratio is indicative of the number of SWNT defects, one would have expected the increased number of defects to lower the conductivity of the network. D-band intensity (and therefore G/D ratio) is also affected by sidewall functionalization [133], but removal of SDS (de-functionalizing the SWNT) should decrease the D band intensity, where instead an increase is observed. Baking also widens the G–band. A narrow G-band and relatively low D-band are characteristics of SDS dispersed films; dispersants such as Triton X-100 exhibit features similar to the SDS film after baking, although those have a higher resistance than SDS-dispersed films, and an increase in resistance did not occur upon baking.

6.10 Other Dopants

It was found that Hexafluoroisopropanol (HFI) has a small doping effect on SWNT films. Immersion of an ODCB-dispersed film in HFI at 45C was found to cause a resistance drop of 290 Ohm/Sq to 244 Ohm/Sq, along with no Raman signal change and the expected small drop in the S_{11} band intensity.

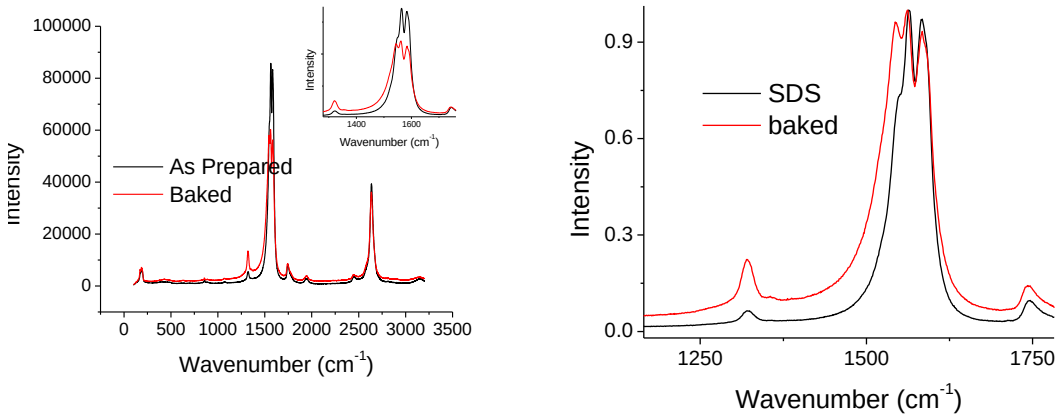

Figure 63 Film 91%T, 1270ohm/sq before and after baking at 350C in inert gas. Baking shows an increase in D-band intensity, and also a widening of the G-band.

It is known that Tetracyanoquinodimethane (TCNQ) causes a resistance drop when intercalated into the middle of SWNT. To investigate its use as a wall dopant, the TCNQ was dissolved in DMF, and films dipped in the resulting solution. The green residue from the TCNQ/DMF solution was washed off with fresh DMF. A resistance increase was observed, from 4 kohm/sq to 11.6 kohm/sq, and there was no change in the S_{11} band. Redoping at elevated temperature dropped the resistance to 6.1 kohm/sq. Doping a similar film with TCNQ/DCE at 70C dropped the resistance from 650 to 600 ohm/sq. The substrates for all TCNQ turned light green/ dark yellow upon doping, and therefore had an increase in the visible spectrum absorbance. TCNQ doping was not further pursued.

Chlorosulfonic acid (CSA) was also explored as a dopant, and did cause a notable decrease in resistance, from 832 to 260 ohm/sq, 320% increase in conductivity. It was, however, found very hard to use, in that the films had a tendency to detach from the substrate upon exposure. Doping with CSA was not explored in depth for this reason.

Also, an attempt to change the conductivity with applied pressure was also undertaken, using films made with different dispersants. It was hypothesized that pressure would bring the SWNT into more intimate contact with one another, lowering film resistance. With modest amount of pressure, up to 6.6 kg/in^2, no change in resistance was observed. However, by applying a large amount of pressure with a C-clamp, an increase in resistance was observed (see Table 5). This new, higher resistance remains even after pressure on the film is released. It is not understood why this resistance increase occurs.

6.11 Conclusions

We have shown that doping of SWNT can be carried out after deposition into film form, rather than as grown in powder form or in solution. Proton donors such as strong acids increase film conductivity by sidewall attachment to the SWNT, rather than changing the degree of bundling or connections between SWNT. The shift in Raman G-band shows a change in Fermi level of metallic SWNT upon doping, while absorbance spectroscopy shows significant changes to the semiconducting band structure. The linear relation we have found between the degree of doping and the drop in S_{11} intensity in the absorbance spectrum shows that the major effect of dopants is to increase the conductivity of semiconducting SWNT. Even so, the conductivity of semiconducting SWNT cannot be raised to the level conductivity of metallic SWNT, with the possible exception of Chlorosulfonic Acid.

Doping can be instigated by exposure to both liquid and vapor phases of the dopant. The degree of doping does reverse over time, but films can be redoped, albeit not to the same degree as the

Table 5 Changes in film resistance upon applying pressure to the film surface

Dispersant	loading ($\mu g/cm^2$)	original R (Ω/Sq)	R with pressure (Ω/Sq)	Resistance change (%)
ODCB	6	59000	76000	29
SDS	1.6	1000	1080	8
Triton X-100	4	610	660	8

original doping. If films are exposed to multiple dopants, the degree of doping only falls to the resistance level of the stronger dopant.

Doping has been investigated for films made from multiple dispersants, and for the strong proton donors, the resultant Raman and absorbance spectra depend only upon the dopant, not the dispersant, despite having different shape spectra before doping. The presence of residual surfactant in a film does not change the position of Raman peaks, although does change their widths. Similarly, residual surfactant can suppress the S_{11} absorbance peak, and the Raman D-band, although its removal through baking does not alter the film conductivity.

CHAPTER 7 PERCOLATION IN SWNT NETWORKS

7.1 The percolation threshold

A percolative network is a distribution of objects in which no continuous path forms between objects until a certain critical density is reached. If the network is a series of conductive objects, below this threshold the network will never be conductive, while above it, the network will be. A thin film of carbon nanotubes can be viewed as a two-dimensional percolative network of "conducting sticks" [135-138]. As one begins to deposit nanotubes onto a substrate, at first not enough will be present to make the network continuous. That is, the network will have infinite resistance on a macroscopic scale. As one continues to add nanotubes, a critical loading will be reached, and the now-continuous network will be conductive. Figure 64 shows a SWNT network very near percolation threshold. This is the percolation threshold [139, 140]. As more nanotubes are added, the conductivity continues to increase, along with the density of SWNT in the network.

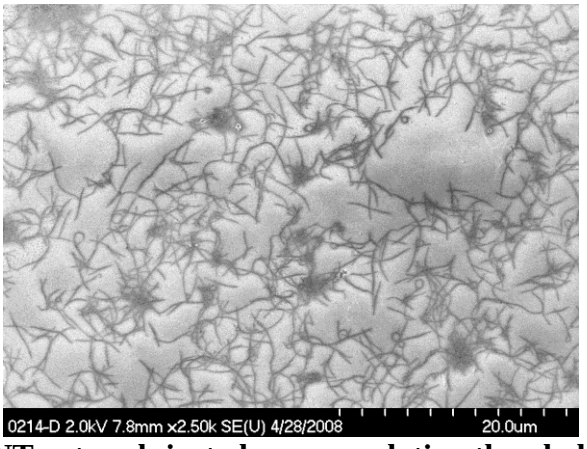

Figure 64 SEM of a SWNT network just above percolation threshold. There is a continuous network, but removal of only a few nanotubes would leave isolated clusters.

Charge transport in polymer-embedded nanotube networks has been studied extensively, and models for percolation in these nanotube polymer networks have been proposed [141, 142]. Even at nanotube densities below percolation, though, the polymer matrix still has a current carrying capacity [143-147]. Networks of only nanotubes differ in this regard, as there is no medium to transport charge once the nanotube density falls below the percolation threshold. Different methods are therefore necessary to experimentally determine percolation in these networks, since large-scale electrical properties cannot be studied below percolation threshold.

Due to the 1:2 metallic: semiconducting ratio of nanotubes, metallic nanotubes are expected to form a continuous network after the overall formation of the network. This is thought to be of importance, as the junctions between metallic nanotubes have better transport properties than junctions involving semiconducting nanotubes. A rise in conductivity would be expected once a continuous network of metallic nanotubes is formed. This metallic threshold has been determined to exist at around 80%T [135, 148, 149]. However, it has been shown that continuous networks below the metallic threshold are desirable for some applications [136, 148, 150]. Therefore, a study of the "real" percolation threshold of a nanotube network is warranted.

7.2 Lattice percolation and universal parameters

The onset of percolation in a network is dependent on the aspect ratio of the objects which comprise the network. If each stick has a length 2a and diameter 2b, then the percolation threshold is

$$p_c \propto b/a. \tag{7.1}$$

Thus, the greater the aspect ratio, the lower the threshold.

As we are interested in understanding the role that junctions between bundles play in the networks in addition to the role of the SWNT bundles themselves, it is important to know how the number of intersections scales with the number of sticks. From assuming all sticks to be randomly oriented to one another, and have a soft-core interaction, the average number of intersections per stick, N, is linearly proportional to the number of sticks, p [151] :

$$N = (4/\pi)(a/b)p \tag{7.2}$$

The percolation threshold, p_c, therefore corresponds to a critical number of intersections, N_c, where a continuous network forms on a large scale,

$$p_c = (\pi/4)(b/a)N_c \tag{7.3}$$

The value of N_c is invariant, independent of aspect ratio, and found to be about 3.64 [31], or one [151], depending on the author. Is not invariant, however, when the size of the objects are widely distributed [152]. The total number of intersections in the network, N_{tot}, is quadratically dependent on the total number of sticks, by algebra from equation 7.3 can be determined simply to be

$$N_{tot} = (4/\pi)(a/b)p^2 \tag{7.4}$$

A percolation network can be generally described as an array of sites, a lattice, where sites are either occupied or unoccupied. If two occupied sites are adjacent to one another, they are said to be connected, bound to one another. In the case of conducting sticks, a point where a stick exists can be considered to be an occupied site, and the intersection of two sticks can be considered bound sites [31]. A network below percolation threshold is composed of isolated clusters of connected sticks, and as p_c is approached, the clusters become interconnected until a connected

cluster spans the entire network. Eventually, far enough above p_c, there are no isolated clusters, and all sticks are connected. The strength of this network, that is, the probability that a given site belongs to the infinite network, scales in the form [153]

$$P \propto (p - p_c)^{\beta} \tag{7.5}$$

Note this scaling law is independent of the lattice; the shape and size of the objects and the number of dimensions occupied changes only the values of p_c and β, with the law retaining the same form.

From this percolation behavior, it becomes apparent that a given network has an associated length scale, a correlation length,

$$\zeta \propto |p - p_c|^{-\nu} \tag{7.6}$$

This is the average distance between two sites in the same cluster, or the average radius of a cluster. Beyond this length, it becomes improbable to find objects belonging to the same cluster [153]. From this equation it is clear that this interpretation of length scale only applies for $p<p_c$. For $p>p_c$, ζ would decrease as p increases, while the radius of clusters clearly does not get smaller. This does not necessarily mean that ζ is not a useful quantity for $p>p_c$, only that it must be interpreted differently. Any quantity, X, related to network connectivity should scale in the form

$$X \propto \zeta^{x/\upsilon} \tag{7.7}$$

so long as the sample size $L>>\zeta$. This includes network conductivity, for which a theoretical framework is well developed, and also frequency-dependent response of the network, which we will demonstrate experimentally.

The conductivity of a network of conducting sticks will have the relation

$$\sigma = \alpha(p - p_c)^t \tag{7.8}$$

where p is the density of conducting sticks, and p_c is the percolation threshold. The critical exponent, t, depends on the fractal dimensionality of the sample, and α is related to the conductivity of a single stick [14, 154].

It is important to note that despite obeying a scaling law of the same form, the conductivity exponent t is not necessarily required to be the same as the critical exponent β. Many of the occupied sites that are connected to the infinite lattice are dead ends, and do not lead to another part of the network. The values obtained by examining the current-carrying lattice sites would therefore not be the same as the values obtained by examining all occupied lattice sites. This is especially true for a network of conducting sticks, as the objects that comprise the network are different from the parts of the network that actually carry current. Such a network has many dead ends, and current is only carried through the parts of sticks which lie between two intersections.

It has been asserted that for transport in two dimensions t=1.3, for three dimensions t=1.94 [14, 15, 155], based on theoretical calculations [153]. Deviations from this in nanotube films have been observed, and reasons for that will be discussed later in this chapter.

7.3 Continuum percolation and non-universal parameters

The calculations of percolation on the lattice model do not take into account the fact that in these networks each object and each bond does not lie upon a prearranged set of points. More importantly, lattice percolation does not take into account that the strengths (conductivities) of the bonds are widely distributed. A continuum percolation model will account for both of these assumptions. While many of the properties of our films can be accounted for by the simpler lattice model, there are some important differences in results between the two models.

It is usually assumed that the distribution of bond strengths obey a power law distribution, [153]

$$f(\sigma) \propto \sigma^{-w} \tag{7.9}$$

This type of distribution arises from any continuum model where bonds are widely distributed [156], and is independent of the shape of the objects comprising the network, and of the dimension of the network. With *w*=1, $f(\sigma) = 1/\Lambda\sigma$, which is the case for bond conductance of the form

$$\sigma = \sigma_0 e^{-\Lambda\rho} \ (0<\rho<1) \tag{7.10}$$

such as a thermal hopping or quantum tunneling mechanism. This means that by integration of the distribution function, *f(σ)*, that

$$p - p_c = \frac{1}{\Lambda} \ln \frac{\sigma_c}{\sigma_1} \tag{7.11}$$

for $p>p_c$ [153]. Thus at percolation threshold is $\sigma_c = \sigma_0 e^{-\Lambda p_c}$, and $\sigma_1 = \sigma_0 e^{-\Lambda p}$ is the expected bond conductance at or above p_c. From this reasoning alone, given only the assumed distribution of bonds described by equation 7.9, there is not a general expression for the overall network

conductance. This does mean, however, that the conductance of the sample is limited by the bond conductance, as described below. The upper limit on conductivity, σ_{max}, of a two dimensional network would be

$$\sigma_{\max} \propto \sigma_c = \sigma_0 e^{-\Lambda p_c} \tag{7.12}$$

A network at percolation threshold has a certain number of bonds, N_{tot}, whose conductances vary according to the distribution $f(\sigma)$. Since there are only a few continuous channels that span the network, the flow of current is very limited in where it is permitted to travel. As the density of the network increases above percolation threshold, there are more bonds, with more choices for current to flow, and with most of the current flowing through the most conductive bonds. For this reason, the number of bonds, N_{tot}, with the highest conductances determines the conductance of the network [154, 157]. That is, the conductance of a network above percolation threshold with bond distribution $f(\sigma)$ is the same as a network at percolation threshold, except including only the highest-conductivity subset of $f(\sigma)$ that has the number of bonds that occur at p_c. This also corresponds to a minimum conductivity value, σ_c, in this subset. This critical value σ_c is the limiting conductivity of the network.

In the general case, once can write a distribution function as

$$f(\sigma) = (1-w)\sigma^{-w} \tag{7.13}$$

where $0<w<1$ and $0<\sigma<1$ (with arbitrary units for conductivity, σ). For the single-stick conductivity prefactor α in equation 7.8, there is instead an expectation value of the conductivity, such that

$$\sigma = < \alpha^{-1} >^{-1} (p - p_c)^t \tag{7.14}$$

$$< \alpha^{-1} > = \int_{\sigma_c}^{1} f(\sigma)\sigma^{-1} d\sigma \tag{7.15}$$

The limits take into account the maximum allowable value of σ=1 and the critical conductivity described in the previous paragraphs. Therefore,

$$< \alpha^{-1} >^{-1} = w(1-w)\sigma_c^w \tag{7.16}$$

By finding the occupation probability of this subset $p_c = p\int_{\sigma_c}^{1} f(\sigma)d\sigma$, the relation $\sigma_c = ((p - p_c)/p)^{1/(1-w)}$ is found. This gives the important result

$$\sigma \propto (p - p_c)^{t+w/(1-w)} \tag{7.17}$$

with *p* near p_c. This means that the critical exponent depends on the width of the distribution, and also the conductivities of the bonds. Smaller conductivities are associated with a higher value of *w/(1-w)*, and therefore a larger critical exponent [157]. As conductivities become sufficiently large and the distribution narrows, then the critical exponent becomes the dimensionally dependent value of *t*. Similarly, the conductivity prefactor depends on the width of the distribution, and is not simply the mean value of the bond conductivity. Despite the number of experiments which determine and discuss the critical exponent for different types of nanotube networks [14, 15, 138, 158, 159], and the disagreement of these experimentally determined values with the predicted values from lattice percolation theory, these two important results from continuum percolation theory have not been applied to nanotube networks until now.

7.4 Expression and units of percolation threshold

Percolation threshold can be expressed in any unit that is directly representative of the quantity of conducting sticks present. This can be the actual number of sticks, or the volume or mass of sticks, or even the Beer's-law optical absorbance of the sticks, among other things. For our nanotube networks, we typically use the mass of SWNT (in μg) per unit area (in cm^2) to express percolation threshold and density of SWNT present. However, from equation 7.8, it is clear that if one chooses the appropriate arbitrary unit for *p*, then α becomes the actual conductivity of the conducting stick.

Unlan [15] has asserted that α is the actual stick conductivity, σ_0, if *p* is expressed as a ratio of the volume occupied by sticks, V_{NT}, and the total volume of the network, *V*. That is,

$$\sigma = \sigma_0 (\Phi - \Phi_c)^t \tag{7.18}$$

where $\Phi = V_{NT} / V$. This can be calculated from *p* in μg/cm^2 by dividing by the thickness of the film to get the volume density of SWNT in μg/cm^3, and then using the SWNT specific gravity, 1.3, to find the excluded volume of the network. Near percolation threshold, the effective thickness is constant, equal to the average diameter of a bundle. From SEM images, this is approximately 20nm for SWNT dispersed in Triton X-100, respectively. For a film at percolation threshold, 0.15 μg/cm^2, and a thickness of 20nm (the effective thickness of a monolayer or less), this yields films that are 5.8% occupied by nanotubes.

Once the network is sufficiently thick, the thickness increases linearly with the amount of sticks present, and Φ is constant. Oddly, that would mean that this "universal" equation would only apply near the percolation threshold, since σ is not constant as a function of thickness, even for

the thickest of films. This is not a fundamental restriction of the equation 7.8 with other units for p such as $\mu g/cm^2$, or sticks per square area. However, the soft-core percolation model assumes that the objects truly intersect one another. That is, they are considered to occupy the same space in two dimensions, rather than overlap into a third dimension. By this reasoning, even for multi-layer films, the effective thickness would still be that of a single bundle, and Φ would increase at the same rate as other p units.

7.5 Determination of percolation threshold as a function of dispersant and purity

Films varying from 86% to 99% transmittance were prepared be sonicating SWNT in 1% SDS solution. Two such sets were made, one with as-grown SWNT, and the other with chemically purified SWNT. Another set was made with purified SWNT dispersed in Triton X-100. This is a very wide range of nanotube loadings, and covers a range of transmittances much lower than a monolayer (see Figure 65). SWNT films have not before been prepared by a single method of preparation up to such high transmittances for study of percolation threshold.

The percolation threshold and critical exponent were determined for each set of films by plotting equation 7.8 as $y' = \log(\sigma)$ vs $x' = \log(p - p_c)$. The value of p_c was varied manually, and the plot fit linearly in Figure 66. The linear fit with the lowest R^2 value was chosen as having the correct value of p_c. The conductivity coefficient and critical exponent was extracted from the best fit equation $y' = mx' + b$, where $t = m$ and $\alpha = 10^b$. These values are given in Table 6.

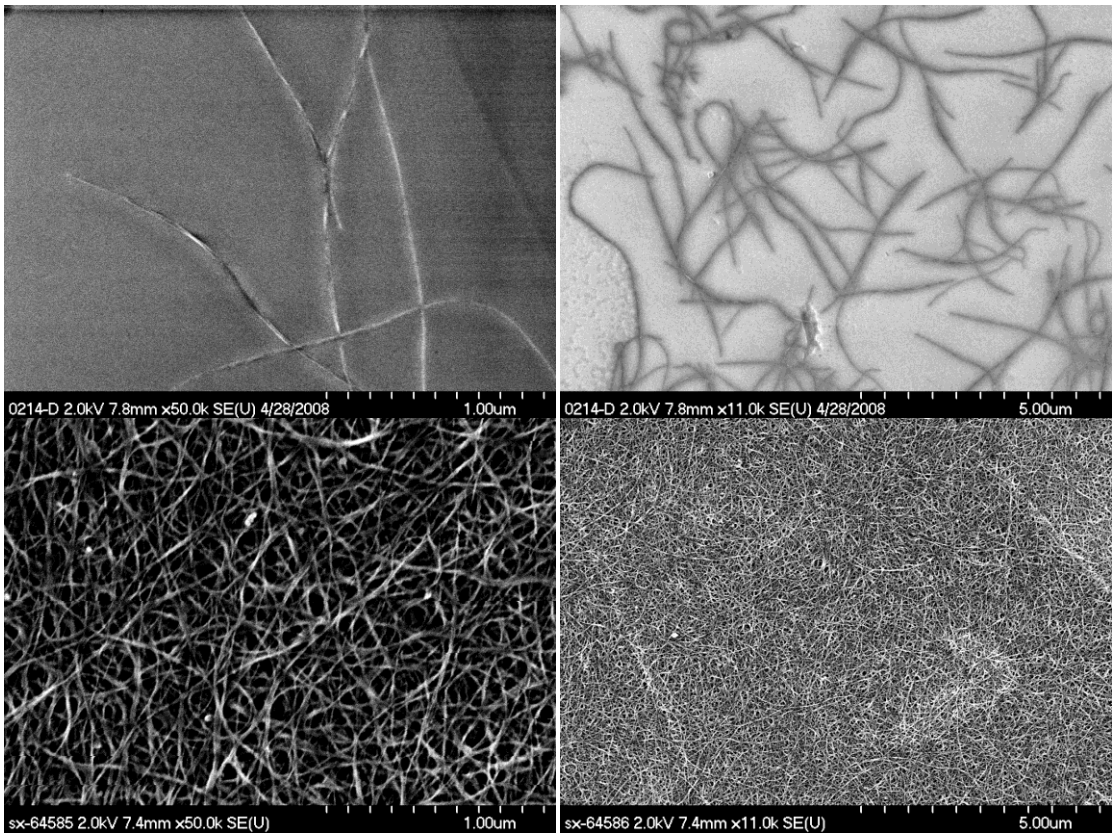

Figure 65 A dense SWNT network (bottom), well above percolation threshold, and a sparse SWNT network at percolation threshold (top). For the thicker network, many conduction paths form, with many junctions between each bundle. For the thinner network, there are very few conduction paths.

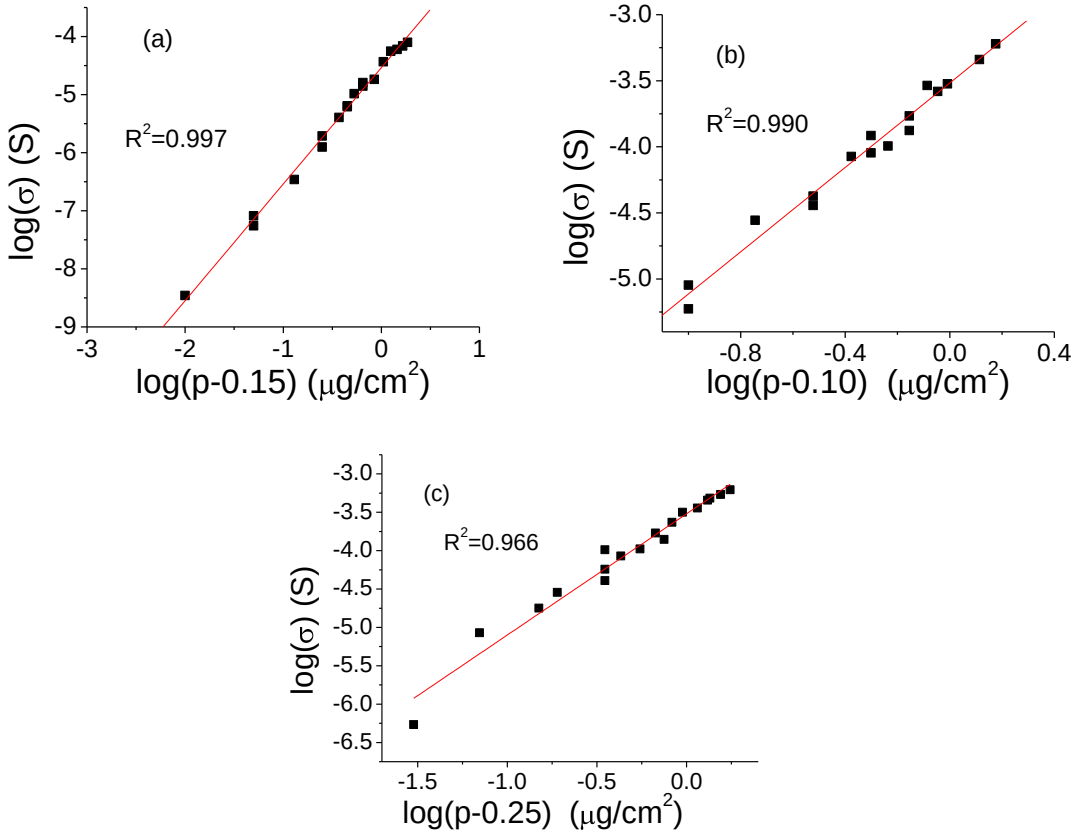

Figure 66 (a) Fit of pure SWNT dispersed in Triton X-100 using equation 7.18, yielding a best-fit of $y' = (2.006 \pm 0.036)x' - (4.535 \pm 0.027)$. (b) Fit of pure SWNT dispersed in SDS, yielding a fit of $y' = (1.596 \pm 0.060)x' - (3.517 \pm 0.028)$. (c) Fit of as-grown SWNT dispersed in SDS, yielding $y' = (1.580 \pm 0.072)x' - (3.519 \pm 0.041)$.

Table 6 Values of $\sigma = \alpha(p - p_c)^t$ with corresponding G/D ratios and Itkis purities for different dispersants.

Dispersant	SWNT type	Absorbance Purity	G/D Ratio	p_c	t	α
SDS	As-grown	0.10	4.6	0.25	1.42	3.6E-5
Triton X-100	purified	0.26	4.8	0.15	2.00	2.9E-5
SDS	purified	0.25	12.3	0.10	1.60	3.0E-4

As expected, the percolation threshold for purified SWNT (p_c=0.10 μg/cm^2) occurs at lower loadings than for as-grown SWNT (p_c =0.25 μg/cm^2). This is due to the higher average aspect ratio of the purified sample, with fewer non-nanotube inclusions. The values of p_c are highest for the lowest absorbance purity, which is expected for samples with a high content of non-nanotube (low aspect ratio) material. The network conductivity for all loadings was also higher for purified SWNT, in line with the higher value of α (3.0E-4 for pure SWNT, 3.6E-5 for as-grown SWNT). An examination of Raman and absorbance purity assessments for each set of films shows that the high value of α corresponds to a high G/D ratio, and is due to the lower number of defects, making the bundles more conductive (see Table 6).

The value of *t* for both as-prepared and purified SDS-dispersed SWNT was found to lie between the expected values of 1.3-1.94, near the theoretically derived value for transport in two dimensions (1.3), similar to the results of Unlan [15], Hu [14], and Kilbride [160]. However, Triton X-100 dispersed samples have a critical exponent characteristic of a three dimensional network. The value of *t* for all dispersants was higher than expected for a two-dimensional system, but the Triton X-100 dispersed SWNT was higher than expected for even a three-dimensional system, if equation 7.8 were to be completely accurate.

Since the percolation scaling law is derived for values near p_c, the use of nanotube densities away from p_c could be attributed to variations from these expected values of *t*. This is not a plausible explanation; the scaling law holds for loadings far above percolation threshold, as will be shown below. In fitting the percolation model to our data, the experiments give values of *t* higher than 1.3 in all cases, with Triton X-100 dispersed films having the highest value of *t*=2.

From the predictions of Keblinski [161], it would be reasonable to assume that the higher exponents are actually due to an observation in the breakdown in percolation law, due to the fitting of data far above percolation threshold. To examine this, the same fitting procedure was carried out using only the data from thinner networks. The original data set included nanotube loadings from 0.15-2.0 $\mu g/cm^2$. These second fits were carried out using only loadings below 0.6 $\mu g/cm^2$, and were done again using loadings only below 0.4 $\mu g/cm^2$. Using only even lower loadings was not possible, due to the lack of data in that regime. In all cases, for both dispersants, the critical exponent did not change. This means that the scaling law observed is universal among different density networks, for densities much higher than previously predicted, and is dependent only on the method of preparation of the network.

The mechanism for the high values of *t* cannot be completely understood within the lattice percolation model, but it was first considered that this could be explained by the dimensionality varying from a strictly 2D network, allowing some transport in the third dimension between layers for thicker samples. This would occur more in films with a high number of defects within individual bundles, as more transport would occur through the connections between bundles, bypassing those defects. This three dimensional behavior would translate into higher values of *t*, as observed for the Triton X-100 dispersed networks, which have higher number of defects. This does not appear to be the case, though.

The continuum percolation model allows for widely distributed bond conductances, which is expected for a expected for a SWNT network, where the SWNT can occur in both semiconducting and metallic form, and in form, and in a wide range of bundle sizes. In the continuum case, conductivity scales in the form

$\sigma \propto (p - p_c)^{t+w/(1-w)}$ **(equation 7.17), with the conductivities distributed by the function** $f(\sigma) = (1-w)\sigma^{-w}$ **(equation 7.13). With the dimensionally dependent t=1.3, the values of *w* are given for given for our various dispersants in**

Table 7. Note that the values of *w* are always positive, but less than 1. Smaller values of *w* correspond to a smaller range of $f(\sigma)$ values. This means that higher values of the percolation exponent are attributable to a larger distribution of conductivities. As-grown SWNT become uniformly dispersed more quickly than purified SWNT, and SDS disperses SWNT more readily that Triton X-100. That is, the ease of dispersibility translates into a network with a narrower range of bundle and junction conductivities, as would be expected from a uniformly dispersed solution. Thus, conductivity exponent could also be used as an indicator of a good dispersant.

7.6 Bulk and interface conductivities

There are two contributors to the resistance of a nanotube network: the resistance of the nanotubes, and the resistance of the connections between nanotubes. Depending on the strength of the connections between bundles, it is possible that either the junctions or the bundles themselves could dominate the resistance. A theoretical study of the relation between relative network resistances of conducting sticks and their connections predict different critical exponents for each case of dominance [161]. In two dimensions, t=1.3 in both cases, for values of p near p_c. For values of $p >> p_c$, the critical exponent was predicted to change from 1.3 to 1 for the bulk-dominated case, and from 1.3 to 2 for the contact-dominated case.

Table 7 Values of the conductivity distribution exponent (equation 7.17) for various dispersants.

	SDS as-grown	Triton X-100 purified	SDS purified
$w/(1-w)$	0.09	0.67	0.27
w	0.08	0.4	0.21

It was also predicted that in three dimensions the percolation scaling law should only hold true for $p<2p_c$ for bulk-dominated conductivity, but for $p<5\ p_c$ for contact-dominated conductivities. Deviations from the two-dimensional percolation scaling law for high values of p should also occur for both bulk and contact dominated resistances, although it was not predicted at how far above p_c this should occur. It was noted that experiments have not confirmed this breakdown in the scaling law at high loadings, in large part because two dimensional networks formed from most materials have an occupied volume fraction of $p_c>50\%$. But for our SWNT networks, percolation occurs at loadings lower than 6% occupied volume fraction. The fit in Figure 66 shows that the percolation scaling law in two dimensions holds for an entire range of loadings through 100% occupied volume fraction, well past the predicted breakdown in the scaling law.

In this view, the higher value of t for triton than from SDS could also suggest that Triton films have a higher contact resistance than SDS films. The role of defects in bundle resistance is not major contributor in the high exponent, since as-grown SWNT dispersed in SDS have similar G/D ratios as purified SWNT dispersed in Triton X-100, while giving a lower value of t.

7.7 Approximation for small p_c values with $p>>p_c$

The relationship $R = R_0\Phi^{-t}$, Archie's Law, was first stated as experimental observations of the relationship between resistance and porosity of rocks saturated with brine [162], and has been the standard relationship for determining rock resistance ever since. In this law, Φ is the volume proportion of the rock occupied by pores, R_0 the conductivity of the brine. This can be explained under the auspices of percolation theory and is consistent with a simplification of the percolation model when $\Phi>>\Phi_c$. For this reason it as been discussed as applicable to percolation problems with sufficiently small values of p_c with $p>> p_c$ [154].

Similarly, SWNT films have an extremely small percolation threshold, and it has now been established that the critical exponent is valid for thickness ranges far away from percolation threshold. If this were to be true, t and R_0 would be calculable by this approximation without knowing p_c. This is especially important since it would eliminate the need to make films in the thickness range near percolation threshold, which are the hardest films to make and measure. This approximation was tested, both for the entire range of loading values and only for the higher loadings (0.8-2.0$\mu g/cm^2$), and the values of t that were found did not agree with the correct values determined by the percolation scaling law. The Archie's Law approximation is not valid for SWNT networks.

7.8 Approximations of bundle and junction conductivity

It is important to determine the reasonableness of relating measurements of bulk networks, as described by the percolation scaling law, to conductivities of individual SWNT and junctions.

This can be done by using general properties of SWNT from measurement and theory, as described in chapter 1.

Assuming a SWNT average diameter of 1.5nm, and a closest packed arrangement of tubes within the bundle, a 20nm bundle would have a cross-section of 40 SWNT. The resistance, R_B, of the series of SWNT in such a bundle could be given by $\frac{1}{R_B} = \frac{40/3}{R_M} + \frac{80/3}{R_S}$, taking into account the 33%/67% makeup of metallic/semiconducting SWNT. Taking R_M=40kΩ and R_S=330kΩ, the median resistance of a metallic and semiconducting SWNT as described in the introduction gives a bundle resistance of 2.4 kΩ.

A similar calculation can be done using the median tube-tube contact resistance values and the expected ratios of different semiconducting/metallic contacts. From SEM and TEM images of films it is safe to assume an average bundle diameter of 20nm and a SWNT diameter of 1.5nm. Across that diameter, there would be 13 SWNT from each of two bundles in contact with one another, and 169 tube-tube junctions. 1/6, 1/2, and 1/3 of these junctions will be metallic-metallic, semiconducting-semiconducting and semiconducting-metallic, respectively. The parallel resistance of all these junctions would be 3.9 kΩ, using values of 250, 1200, and 750 kΩ for each junction type, as described in the introduction.

Using the relationship p=Φ*20nm*1.3 g/cm^3, as described in chapter 7.4, for triton X-100 dispersed SWNT, and taking t and p_c as derived from the fitting procedure, this gives a value of 5.1kΩ for σ_0 in equation 7.18. The approximate series resistance of the bundle (2.4 kΩ) and

intersection (3.9 kΩ) described in the previous two paragraphs would be around 6 kΩ, definitely comparable to the measured value of σ_0=5.1 kΩ calculated from equation 7.18.

7.9 Doping and percolation properties

Doping of films increases overall film conductivity by the same multiplicative amount, independent on thickness, and is shown in Figure 67. It is clear from equation 7.8 that this multiplicative change in σ only affects the value of α, and not p_c or t. This is the theoretically expected result from a mechanism which increases conductivity of individual bundles (or junctions), without adding any connections or conductive paths. All of our dopants exhibit this behavior. Unfortunately, due to the derived scaling relationship with thickness and the number of junctions with the number of bundles, equation 7.3, it is not possible to determine from this multiplicative effect whether the dopants affect transport through junctions as well as through bundles.

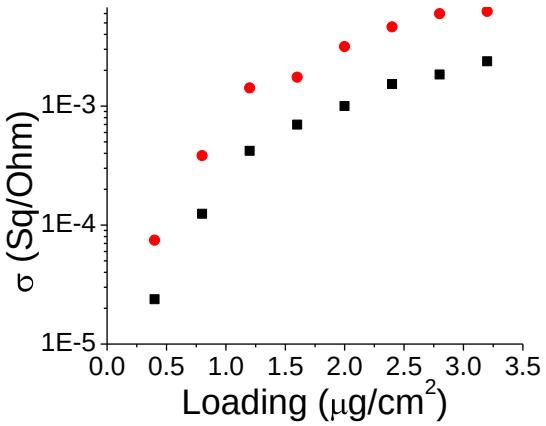

Figure 67 Immersion of a set of SDS-dispersed films in $SOCl_2$ causes a factor of three increase in conducitivity for each film, independent of nanotube loading.

7.10 Percolation from a frequency-dependent perspective

In addition to four-probe DC measurements, impedance spectroscopy was done on all the samples to determine AC conductivity and frequency response based on film thickness and on sample purity. AC measurements were done in a two-probe configuration, as described in chapter 5.3.

In contrast to DC measurements, each frequency, *f*, of an AC impedance measurement probes a certain length scale, *L*, of the network, such that [160]

$$L \propto f^{-a} \tag{7.19}$$

At low frequencies, the length scale is large and approaches the value of DC measurements. At sufficiently high frequencies, the length scale will be smaller than the distance between "nodes" in the sample, and the impedance will have values characteristic of the microscopic network properties. The correlation length of the sample, ξ, described by the scaling law of equation 7.6 is the characteristic length scale which probes the distance between nodes in a sample [160].

In the case of a nanotube network, one would expect this characteristic length to be either the distance between tube defects, or between tube connections, such as junctions within a bundle, or junctions between bundles [30, 160]. As defects and junctions have a higher resistance than the SWNT themselves, the measured conductivity will rise once *L* falls below ξ, as the length scale is no longer related to the conductivity of the whole network, but of the SWNT themselves. The critical frequency, f_c, at which this expected rise in σ occurs, is obvious in our impedance spectra

as a falloff in Z'. This drop in Z' also corresponds to a peak in the plot of -Z", shown in Figure 68. This peak is used to determine f_c, and therefore ξ, since

$$\xi \propto f_c^{-a} \tag{7.20}$$

It has been asserted that the exponent, a, is determined by the randomness of the movement of the charge carriers moving throughout the sample. Experimentally, that means a is determined by an applied electric field on the sample [160]. For no applied field, it is expected that the carriers move randomly through the sample, and a=½. For a large field, where the carriers move in a completely nonrandom way, it is expected that a=1. So ½<a<1 should always hold true.

We have found f_c occurs at higher values for higher loadings, and is linearly related to the DC conductivity of the sample (Figure 69), in agreement to the findings of Xu [163].

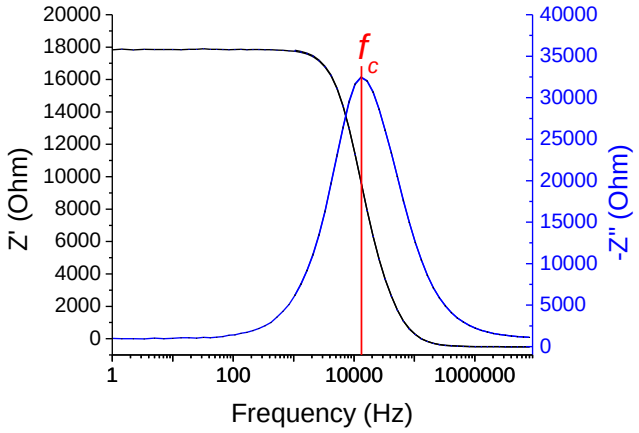

Figure 68 The critical frequency, f_c, is the point where the sharp drop in real impedance (AC resistance), Z' occurs. This corresponds to a peak in the imaginary impedance, Z".

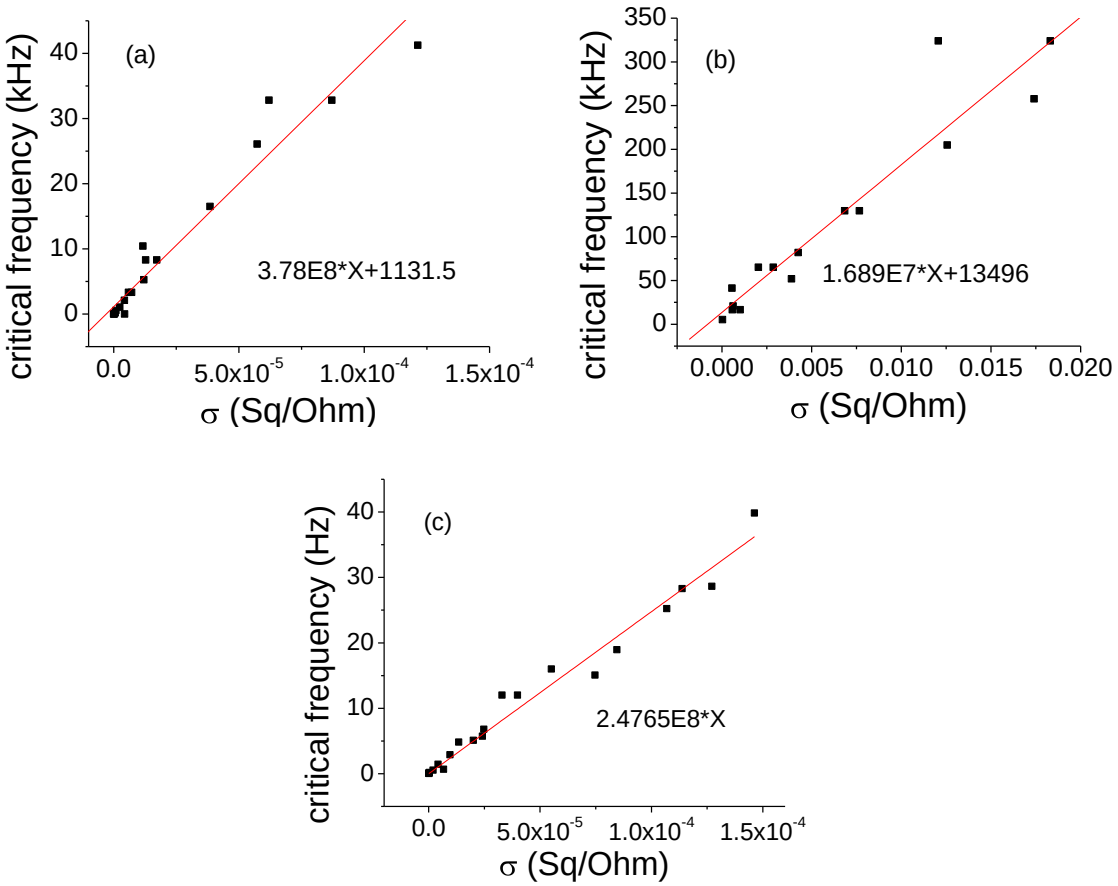

Figure 69 Films of varying thicknesses made from purified SWNT dispersed in Triton X-100 (a) and SDS (b) and a film of raw SWNT dispersed in SDS (c). DC conductivity is directly proportional to f_c.

This means that just as σ displays a percolation behavior as a function of loading, f_c must as well, from the scaling law of equation 7.7. So from $\xi \propto f_c^{-a}$ (equation 7.1), and the linear relation between σ and f_c, we have the percolation equations [153, 164]

$$\xi \propto (p - p_c)^{-\upsilon} \tag{7.21}$$

$$f_c \propto (p - p_c)^{\nu/a} \tag{7.22}$$

In these equations, the value of ν/a is the critical exponent, can be experimentally determined in a manner similar to *t*, and is expected have the same value as *t*.

Figure 70 is a fit of the critical frequencies by the same method as in Figure 66, and gives an almost identical percolation threshold for Triton X-100 films, 0.145 vs 0.15 μg/cm^2, and a slightly higher threshold for SDS films, 0.12 vs 0.10 μg/cm^2. The critical exponents using f_c to fit each set of films was similar to the critical exponents found from four-probe DC data. ν/a was found to be 2.1 vs t= 2.0 for Triton X-100 films, and ν/a =1.4 vs t=1.6 for SDS films (Figure 70).

Taking into account this expected field dependence of mobility and the experimental information from frequency, the expected value for ν, instead of *t*, would be 1.33 for two-dimensional networks of sticks, according to Kilbride [160]. Given the relation $f_c \propto (p - p_c)^{\nu/a}$ (equation 7.22), and the experimental verification that $f_c \propto \sigma$, then the high experimental value of *t* for Triton X-100 dispersed films could be accounted for as smaller amounts of inter-bundle transport, and correspondingly lower values of *a*. The experimentally determined critical

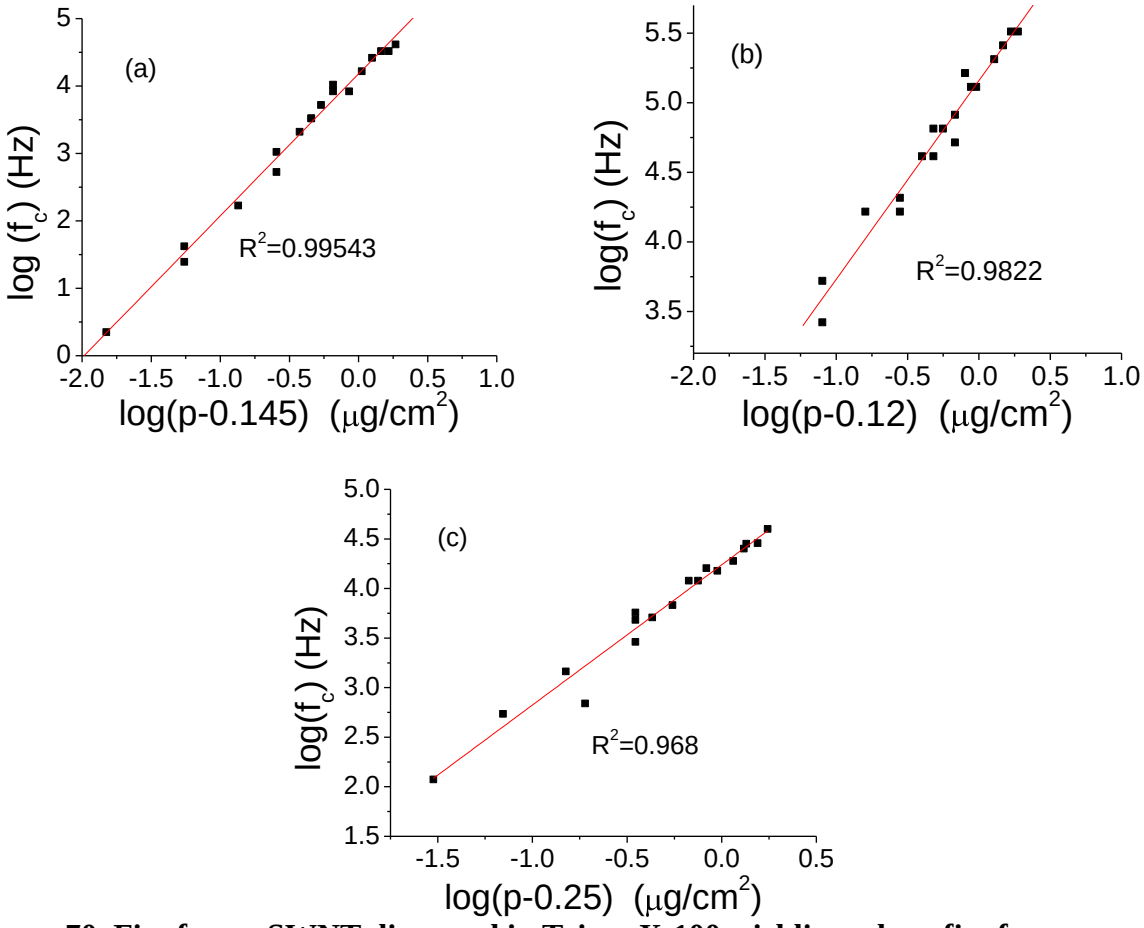

Figure 70 Fit of pure SWNT dispersed in Triton X-100, yielding a best-fit of $y' = (2.105 \pm 0.050)x' + (4.180 \pm 0.035)$ **(a), and for pure SWNT dispersed in SDS, yielding a fit of** $y' = (1.427 \pm 0.068)x' + (5.159 \pm 0.033)$ **(b). An SDS-dispersed raw SWNT film gives** $y' = (1.414 \pm 0.062)x' + (4.239 \pm 0.035)$ **(c).**

exponent υ/a will always have the same value as the previously determined value of *t*, as f_c and σ are linearly are linearly proportional to one another. The values of *a* are given in

Table 8.

It was previously stated that $\xi \propto (p - p_c)^{-\upsilon} \propto f_c^{-a}$ (equations 7.20 and 7.21), but no assumptions were made concerning the constants of proportionality in that relationship. Since it has been shown that υ/a, p_c, and f_c can be determined experimentally from impedance data, we can now write

$$\xi = \beta(p - p_c)^{-\upsilon} \tag{7.23}$$

$$\xi = \chi f_c^{-a} \tag{7.24}$$

and learn more about χ and β from the same fit that was used to extract υ/a. The linear equation from the from the fit in Figure 70 is therefore written as $\log(f_c) = \frac{\upsilon}{a}\log(p - p_c) + \frac{\upsilon}{a}\log(\beta/\chi)$, with the independent and dependent variables $x' = \log(p - p_c)$ and $y' = \log(f_c)$.

Table 8 gives the values found from the data in Figure 70, and it is clear that the constants χ and β are not universal. It is apparent this ratio is related to the conductivity of a nanotube bundle, from the linear relationship between σ and f_c.

By writing $f_c = u\sigma$ and given that $\xi = \chi f_c^{-a}$ (equation 7.23), it is apparent that

$$\xi = \chi u^{-a}\sigma^{-a} = \chi(u\alpha)^{-a}(p - p_c)^{-at} \tag{7.25}$$

By the definition of equation 7.22 that $\xi = \beta(p - p_c)^{-\upsilon}$, then $\beta(p - p_c)^{-\upsilon} = \chi(u\alpha)^{-a}(p - p_c)^{-at}$

Since p_c is an inherent property of the network, and it has already been shown that $t = \upsilon/a$, then

$$\beta / \chi = (u\alpha)^{-a} \tag{7.26}$$

Table 8 Values of critical constants for different types of SWNT networks.

	pure SWNT Triton X-100	pure SWNT SDS	Raw SWNT SDS
t [Figure 66]	2.01	1.6	1.42
$s=\nu/a$ [Figure 70]	2.105	1.427	1.414
a (assume ν=1.33)	0.631829	0.932025	0.940594
b=-(1/a)*log(β/χ) [Figure 70]	4.18	5.16	4.24
β/χ=10^-ab	0.002285	1.55E-05	0.000103
$u=fc/\sigma$ [Figure 69]	3.94E+08	1.80E+07	2.48E+08
α_{DC}	2.90E-05	3.00E-04	3.60E-05
(β/χ)^-(1/a)=u*α_{DC}	11426	5400	8928
(β/χ)^-(1/a)=10^b	15136	144544	17378
α_{AC}=(1/u)(10^b)	3.84E-05	8.03E-03	7.01E-05
a_{calc}=-log(β/χ)/log(u*α_{AC})	0.650841	1.288516	1.009458
$\nu_{calc}=s*a_{calc}$	1.370021	1.838713	1.427373

The values of u are the slopes in Figure 69. From the aforementioned values of β/χ, and the values of a found under the assumption that ν=1.33, then a value of α can be calculated from critical frequency data, and is given as α_{AC} in

Table 8. The percent difference between these calculated values and the values obtained directly from DC measurements vary between 28% and 186%, depending on the dataset.

The constant a can also be determined from β/χ and the calculated α_{AC} values. This gives a value of ν that value of ν that arises from the combined AC and DC experimental data, rather than using the assumed value assumed value of 1.33 based on mathematical predictions of dimensionality. These values are listed as ν_{calc} listed as ν_{calc} and a_{calc} in

Table 8. For the different methods of arriving at these a values, the percent difference is highest for films of pure SWNT in SDS, 32%. For pure SWNT in Triton X-100 and raw SWNT in SDS, the percent difference is only 3% and 7%, respectively. In all instance a_{calc} is higher than a, and for the SDS films, a_{calc} is greater than 1, a condition not allowed in the previously described interpretation of a.

The interpretation of the AC critical exponent which sets ν as a dimensionally dependent constant is preferential to using values of β/χ to determine ν and a, as it gives values within the expected range $\frac{1}{2}<a<1$. This AC values of critical exponent are preferential over the DC values, in that the dimensionally dependent term expected to arise in the critical exponent of any percolation network can be clearly assigned as ν, while the values of t do not agree with such

mathematical predictions. Now that the values of *a* have been determined, the associated length scales have been plotted in Figure 71.

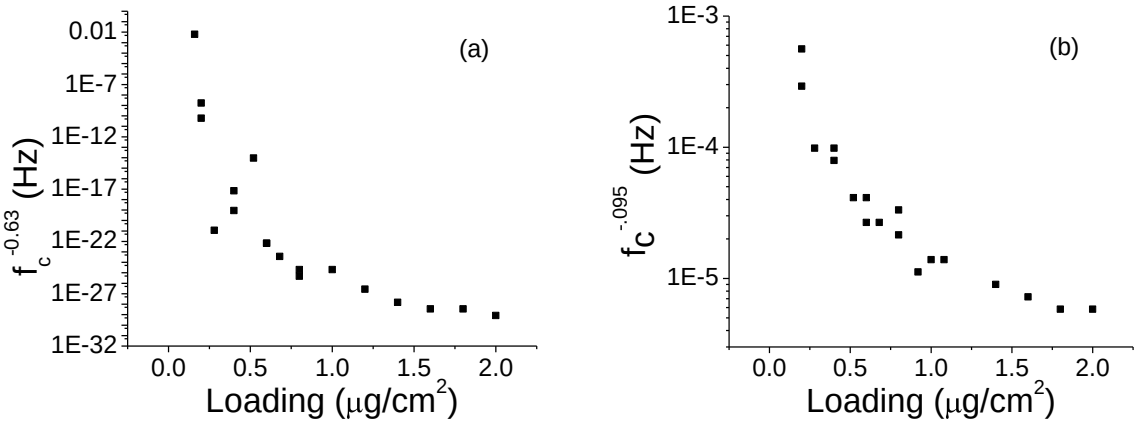

Figure 71 Length scales (without constant of proportionality) for two dispersants. The calculated values of a=0.63 (Triton X-100) and a=0.95 (SDS) have been used (see Table 8). Triton X-100 (a) has a length scale many orders of magnitude larger than SDS (b).

7.11 Junctions and length scales

The number of junctions per bundle increases linearly with the number of bundles, and therefore the distance between junctions decreases linearly as well. The fact that f_c has a linear dependence on conductivity reinforces the idea that the length scale being probed is indeed the distance between intersections of bundles. If the length scale measured primarily inner-bundle interactions, f_c would not be expected to exhibit a strong dependency on loading, as the makeup of a SWNT bundle does not change as the films become thicker. The number of inter-bundle interactions, however, clearly depends on loading, and the distance between inter-bundle connections does drop as the films become thicker.

The number of intersections per stick, *j*, the average stick length, *l*, and the distance between intersections, *d*, is, from simple geometry, related by $j = l/d - 1$. Furthermore, if the probing scale of critical frequency is the distance between intersections, then

$$j + 1 = l/d \propto l/f_c^{-a} \tag{7.27}$$

from equation 7.19. It is known that at percolation threshold, there is on average one intersection per stick [31]. So the average distance between intersections is equal to half the length of a stick. Therefore, for a film at percolation threshold,

$$2 f_c^{-a} \propto l \tag{7.28}$$

With knowledge of average stick length, and the exponential behavior of critical frequency approaching percolation threshold, the constant of proportionality can be determined for a given SWNT sample or dispersant. Similarly, with knowledge of the constant of proportionality, the probing distance can be determined, and physical meaning of the length scale confirmed.

7.12 Conclusions

It was found that the percolation equation holds for SWNT networks in two dimensions, down to very low loadings. There was no evidence of a second, metallic percolation threshold with non-standard percolation behavior at low loadings, as found by Unlan [15]. Our application of this percolation model to two-dimensional networks works for loadings over ten times higher than the percolation threshold, despite the as-derived n-dimensional model only being expected to hold very near percolation threshold [153, 154, 161].

By using different methods of SWNT dispersion, it was found that SDS gives lower value of p_c than Triton X-100, allowing onset of conductivity at a higher transmittance. It was also found that purified SWNT have a conductivity onset at higher transmittances than as-grown SWNT, with as-grown SWNT requiring 2.5 times the amount of material than purified SWNT. This is expected, due to the higher average aspect ratio of SWNT samples without inclusions of non-nanotube carbon. So as a general rule, higher absorbance purities translate into lower values of p_c.

The conductivity prefactor, α, was related to Raman G/D ratio and absorbance purity, with a higher value of α, and therefore higher network conductivity, corresponding to a low G/D ratio and high absorbance purity.

The conductivity exponent was not related to nanotube purity, but instead only to method of dispersion. Its value was higher than the expected value of 1.3 in all cases, ranging from 1.4-2.0. It was shown that this variation arises when a network is composed of a wide range of conductivities. The higher exponents are due to a wider range of conductivities, and a value of 1.3 is only expected if all bundles and junctions fall into a very narrow range of conductivities. For this reason, the conductivity exponent could also be used as a judge of how well the nanotubes are dispersed.

In the case of widely distributed bundle conductivities, the conductivity prefactor of single-bundle conductivity is replaced with an expectation value of bundle conductivities. In this model, low values of σ would also imply a wider distribution, as the distribution function

(equation 7.13) has a wider range of *f* values at lower values of σ. This would fit into the results for pure SWNT in different dispersants, but not into the results for networks with large amounts of non-nanotube inclusions. This is due to the fact that a network with wide distribution of conductivities is dominated by highest conductivity bonds, and while the non-nanotube inclusions still move the percolation threshold to a lower transmittance, the conductivity is dominated by the smaller range of high-conductivity SWNT.

The doping of SWNT films with $SOCl_2$ changes the conductivity by a constant factor dependent on dispersant and on dopant, independent of the density of the network. This means that changing the conductivity of the SWNT or junctions does not change the percolation threshold, as expected. That is, the percolation threshold depends on network morphology, not on the conductivity of the objects which comprise the network.

This also means that the conductivity exponent is not changed by S OCl_2 doping. While this is expected in the lattice percolation model, in the continuum model, this suggests that doping does not change in the distribution of conductivities. This is strange, as absorbance spectroscopy shows that doping alters network conductivity primarily by increasing conductivity of the semiconducting SWNT. This could imply that metallic SWNT dominate the conductivity, and continue to do so after doping, except that it has been shown in chapter 6.7 that doping brings the semiconducting SWNT conductivity to levels nearly of metallic SWNT. More likely, this means that the junctions are a large contributor to network conductivity, and the well-connected junctions are not affected by dopants and are a dominating factor in determining network conductivity. This agrees with the findings of chapter 5.6.

Frequency-dependent impedance measurements have also been made, and the critical frequency found and determined to be linearly proportional to DC resistance. Critical frequency was fit to the same scaling law as conductivity, which arrives at the same percolation thresholds and critical exponents. This allowed a correlation length scale to be extracted from the measurements, which is related to critical frequency via power law by equation 7.20, whose exponent is extracted from the experimentally determined percolation exponent using the theoretically derived dimensional dependence.

Constants of proportionality for the length scales from critical frequency measurements have been determined and also related to DC measurements. These coefficients were found to not be universal among nanotube networks, and were shown to be related to the conductivity prefactor by a power law with the same exponent that relates critical frequency to length scale. These relationships allow a back-calculation of critical DC values, such as conductivity prefactor α, and conversely, the ability to back-calculate the critical AC values such as the critical frequency exponent, a, from DC values. These measured and calculated values can vary from 3%-32% difference.

The correlation length scale, as probed by critical frequency measurements, is a measure of long range connectivity for networks below percolation threshold. This length scale was determined for our networks, all above percolation threshold. Since it has been shown that the distance between inter-bundle junctions decreases linearly with loading, and this length scale has a nonlinear dependence on loading, it cannot be solely a probe of inter-bundle connections.

Within continuum model framework, however, it is reasonable that there are enough high conductivity junctions which are “skipped over” by the frequency probe, which would mean a nonlinear dependence of measured length scale on loading. The deviation from linearity would then be related to the deviation of the conductivity exponent from the expected dimensionally dependent value, which it is.

CHAPTER 8 USE OF SWNT FILMS IN OLED AND OPV DEVICES

The major technological importance of investigating the properties of SWNT networks is their potential use as transparent electrodes. In order to understand the properties of SWNT films necessary for a functioning device, films of several different methods of manufacture were sent to Bin Hu's group in Materials Science and Engineering department. These films were made into either organic photovoltaics (OPV) or organic light emitting diodes (OLED), and their function and efficiencies were tested.

A series of films were prepared on both glass substrates and on Indium Tin Oxide (ITO) substrates. Films were made with different purities of SWNT, both as-grown and chemically purified, and with the centrifugation purification technique described in chapter 4. SDS was used as the dispersant, and the films for all samples were from 70-80% optical transmittance (at 550nm), and from 200-600 Ω/Sq sheet resistance (before doping). A series of these films were doped with the dopants and procedure described in chapter 6, to determine which dopants made the devices function more effectively.

The devices were built in a standard fashion for OLED/OPV devices[165, 166], as shown in Figure 72. These films were used as the base electrode (anode) for OLED and OPV devices. In addition, a solution of crown-ether modified SWNT was prepared by dispersion in water, as in chapter 4.6. The polymer PEDOT was added to this solution, and was spin coated onto substrate for use as the base electrode for OLEDs.

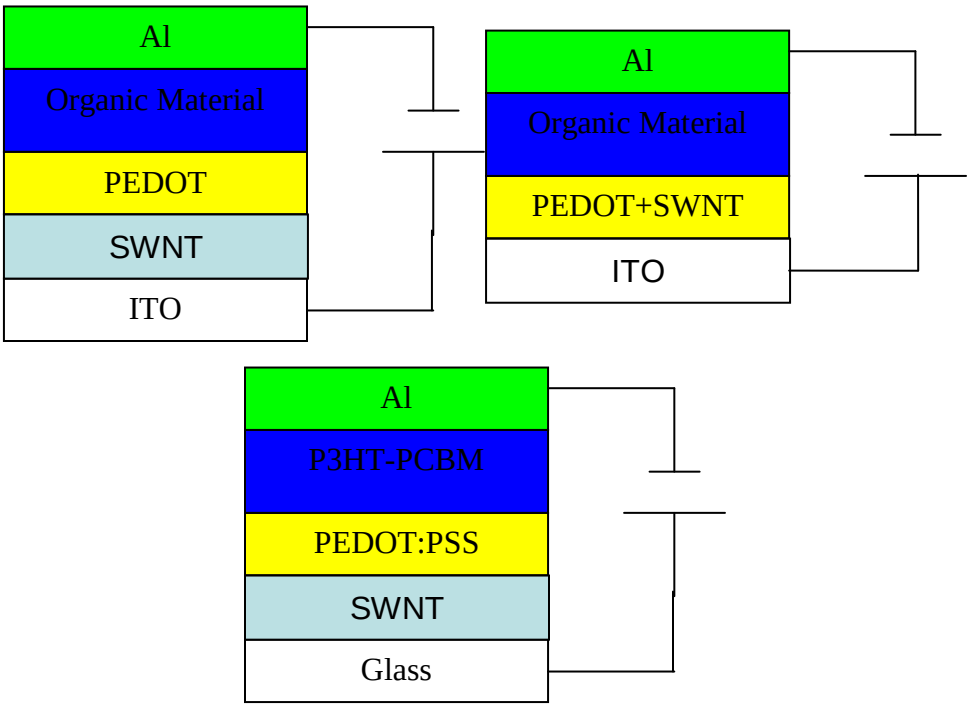

Figure 72 OLED (top) and OPV (bottom) device architecture.

8.1 SWNT films for OPVs

It was shown that an undoped SWNT film is capable of replacing ITO as the electrode in a photovoltaic cell. However, it is not as effective as ITO, giving only 1/13 of the zero-bias current as ITO under white light illumination (Figure 73). A device with neither ITO nor SWNT is shown for reference.

Some of the dopants described in chapter 6 were shown to improve the function of SWNT films when used in PV cells. From Figure 74, the doping changes the voltage necessary to provide current to the device, with ODCB having the greatest improvement. $SOCl_2$ doped SWNT actually perform worse than undoped SWNT.

8.2 SWNT films for OLEDs

For OLED devices, spin coating a layer of PEDOT onto the SWNT layer was necessary for a functioning device, as shown in Figure 72. This PEDOT layer is not needed for ITO-only devices. This polymer layer compensated for the roughness of the SWNT as compared to ITO. Without the PEDOT layer, the device performed very poorly, with an extremely low electroluminescent intensity (Figure 75).

The addition of a SWNT layer on top of ITO reduced the turn on voltage to a level five times lower than for an ITO-only device. However, the current at operation was 1000 times higher, which translates into a lower efficiency. It is believed this high operational current is due to leakage through the thinner sections of the PEDOT layer, also due to the roughness of the SWNT film.

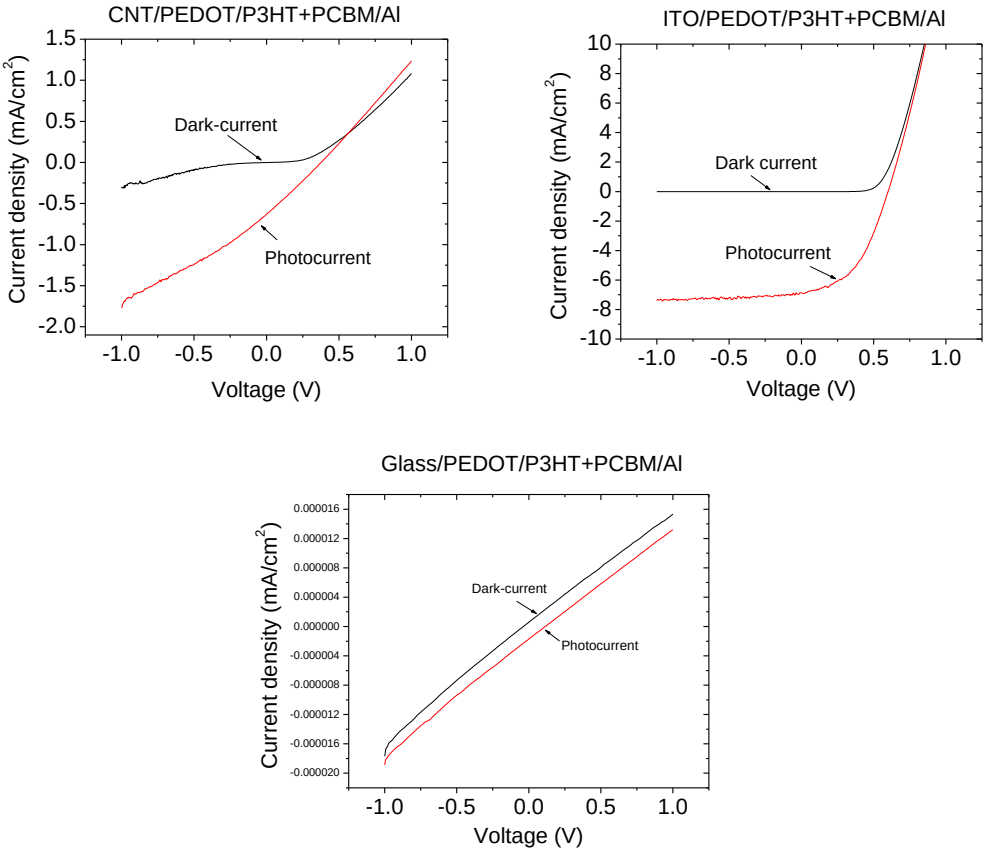

Figure 73 Photovoltaic cell using ITO as the electrode, and using a SWNT film as the electrode. PV cell using neither ITO nor SWNT is shown for reference. SWNT films are capable of replacing ITO as a photovoltaic, but are not as effective.

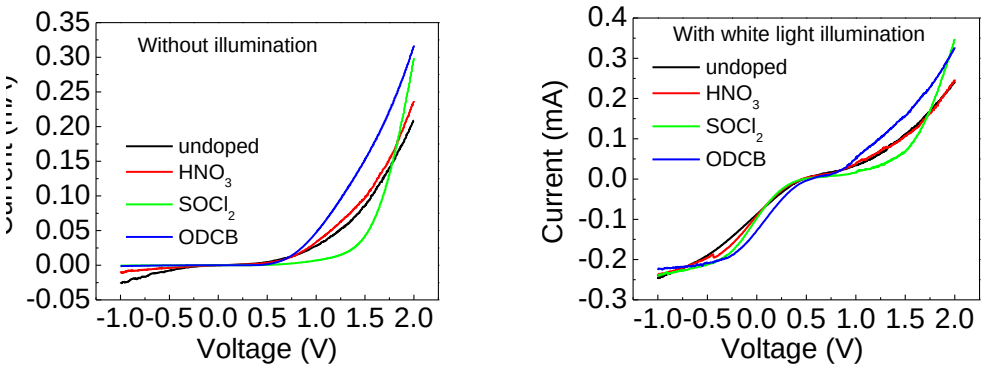

Figure 74 Films with different methods of doping were uszed in photovoltaic cells. ODCB doped films were the most effective in PV devices, $SOCl_2$ doped films were the least effective. PV cell has structure: Glass/SWNT/Pedot/P3HT:PCBM(1:0.8)/Al

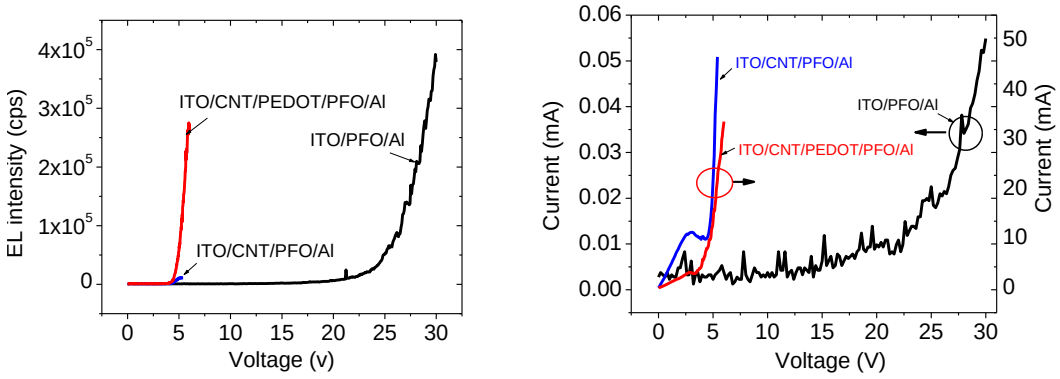

Figure 75 Electroluminescent intensity and current for an ITO-only and an ITO-SWNT OLED. SWNT reduce the turn-on voltage of the device, but have a current three orders of magnitude higher than the ITO device. The devices are only functional with an additional PEDOT layer over the SWNT.

Figure 76 shows a greater calculated power efficiency with the addition of SWNT to ITO than of ITO alone when forming the anode. Also, the color of the LED depends on the organic material used to make the OLED (Figure 72). PFO, MEHPPV, and Alq3 were used for blue, red, and green OLEDs in Figure 77, respectively. The MEHPPV (red) OLED was found to be most effective, having the lowest turn-on voltage. All of the SWNT/glass devices functioned at a lower voltage and had higher electroluminescence than an ITO/glass device.

8.3 SWNT in polymer for OLED

The SWNT/H_2O was prepared in a 50μg/ml solution, and then centrifuged at 9000rpm for 2.5 hours to remove aggregates. The top half of the supernatant was removed and then added to PEDOT in different concentrations: 0.01%, 0.02%, and 0.001% SWNT/PEDOT. Also, PEDOT with no SWNT was prepared as a control. Each SWNT/PEDOT solution was spun cast onto either glass or ITO substrate, and was made into an OLED as described in Figure 72.

When glass was used as a substrate, the device did not function; it would not emit light even at high currents. With ITO as a substrate, all the devices functioned, even the device containing the PEDOT layer without SWNT added. The addition of SWNT to the PEDOT lowered the turn-on voltage for all concentrations; however, as Figure 78 shows, the OLED brightness at a given current was dependent on concentration. A very low concentration of 0.001% SWNT/PEDOT did improve the brightness over PEDOT alone. This improvement increased with the addition of more SWNT, with a 300% improvement in power efficiency at 0.01% SWNT/PEDOT. Doubling that to a concentration of 0.02% actually decreases performance. This is characteristic

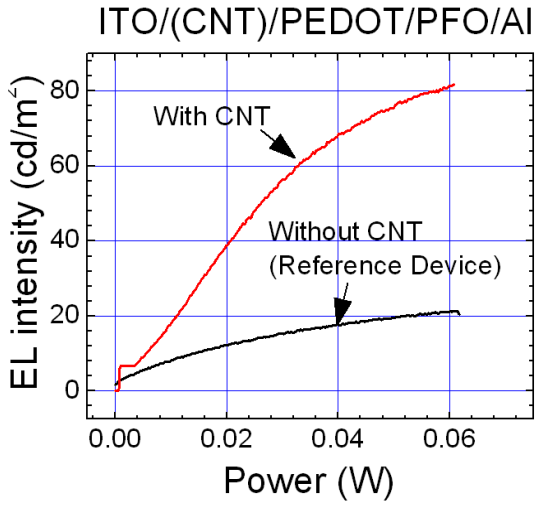

Figure 76 Calculated power efficiency of OLED with and without SWNT

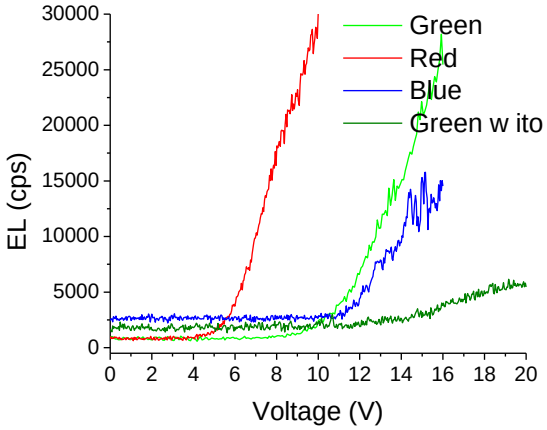

Figure 77 Performance of colored OLEDs with SWNT-on-glass electrode. SWNT on ITO as electrode shown for reference. The SWNT layer improves device performance in all cases, but is most effective for the red LED.

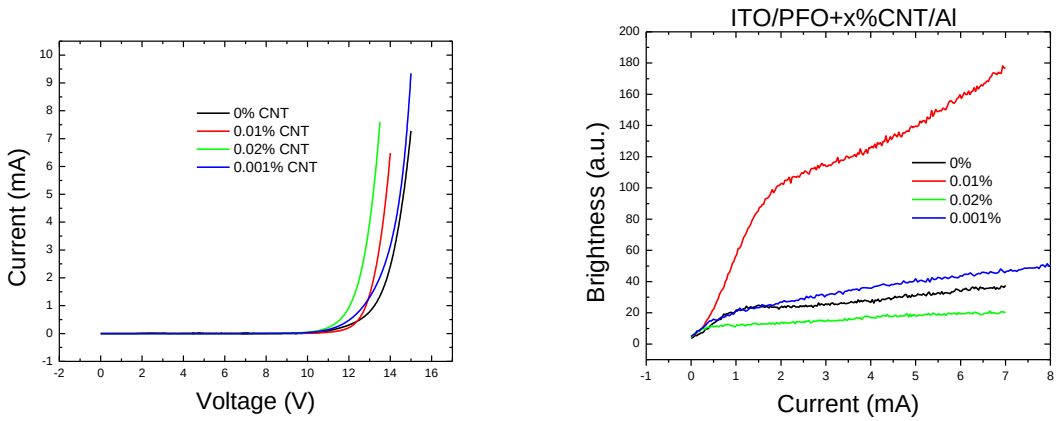

Figure 78 OLEDs with a SWNT/PEDOT composite on top of ITO as the anode. A 0.01% concentration SWNT/PEDOT is most effective; raising or lowering the concentrations do not improve performance. The existance of this critical concentrationis related to the percolation behavior of the composite.

of the critical behavior of percolation networks, where addition of material causes improved performance, but after saturation occurs, performance is degraded.

8.4 Roughness

The major inhibition to using a SWNT film instead of ITO as an electrode was found to be the roughness of the film. An ITO electrode has a 30nm difference in height between highest and lowest points, whereas the SWNT electrode has a 100nm difference. This corresponds to an RMS roughness (standard deviation of Z values) of 3nm and 10nm for ITO and SWNT, respectively, as the AFM images in Figure 79 show. For this reason, many of the SWNT electrodes caused shorts between layers of the devices. This was the reason for spin casting PEDOT over the SWNT electrode as described in chapter 8.2.

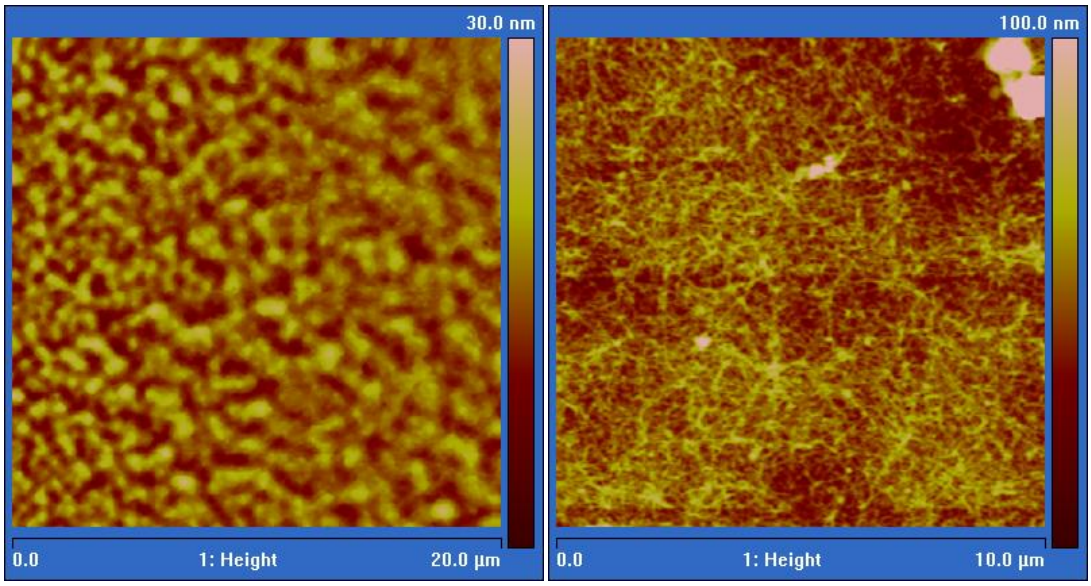

Figure 79 AFM images of ITO (left) and SWNT film (right). The SWNT film is notable rougher, with a height range of 100nm as opposed to 30nm. This proved to be the major inhibiting factor for making functioning devices.

In addition to the general roughness of the film, there are also aggregates which have heights much greater than the height of the film surface. The removal of these aggregates was the great advantage of using a centrifugation technique when preparing the nanotubes to make films. Films made without centrifugation did not work, regardless of whether or not the starting material was as-grown or chemically purified. Despite still having a surface roughness three times ITO, the SWNT still was able to comprise a functional electrode once the large aggregates were removed from solution prior to deposition.

Optical microscope pictures, such as in Figure 80, show that folding of the films near the edges is especially common. It is important to not use films with such folds when making devices. Simply wetting the film with acetone or isopropanol allows parts of films to be easily wiped

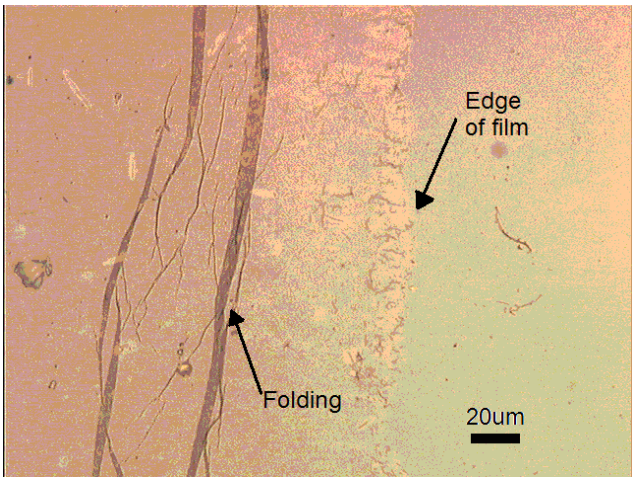

Figure 80 Optical microscope image of SWNT film showing unwanted folding near edges.

away, and this method was used to remove film edges, instead of discarding films with folded edges.

In addition to the roughness of the film, uniform adhesion of the SWNT film to the substrate is very hard to achieve. It was noticed that adhesion was especially hard onto ITO as opposed to glass.

8.5 Conclusions

It was shown that a SWNT film can replace ITO as the transparent electrode in a photovoltaic device. However, these SWNT devices do not function as well as an ITO device, giving less than 10% of the current upon exposure to white light. Certain dopants can increase the performance of the SWNT devices. ODCB was found to be the most effective dopant, although it is not understood why this is, since conductivity was not as high as the other doped films. Film conductivity by doping actually does not correspond to PV performance, with $SOCl_2$, the

dopant with the highest conductivity, performing worse than the undoped device. It has been considered that ODCB leaves a residual layer which interacts with the device structure. SWNT films were instead found to be most effective for improving the performance of OLEDs.

SWNT films were shown to have advantages over ITO alone when used in OLED and OPV devices as the anode. For OLEDs, PEDOT was required as a layer added on top of the SWNT film for hole injection to occur and the device to function. In addition the PEDOT layer compensated for the greater roughness of the SWNT film than ITO substrate. SWNT/glass has the advantage over ITO/glass in having a lower turn on voltage and higher electroluminescent intensity. SWNT/ITO/glass was found to have a greater power efficiency than ITO/glass alone. The addition of a SWNT layer to the ITO substrate improves efficiency by up to 300%.

In addition to coating a SWNT film with PEDOT, dispersing SWNT into PEDOT was found to be effective in making OLEDs. With SWNT/PEDOT OLED, an ITO base was necessary, the device would not function with SWNT/PEDOT on glass only. The performance of these devices was dependent on SWNT concentration, with dramatic improvement once a certain concentration was reached, and a diminished performance with too high a concentration. Although the percolation threshold of SWNT in PEDOT was not tested, this is the type of behavior one would expect from percolation phenomena. In such instances, performance would be enhanced as concentration approaches percolation threshold, and then performance diminished as saturation occurs above percolation threshold.

Roughness of the SWNT films is the major obstacle to be overcome in making of devices. Devices from films made without the developed centrifugation procedure did not function, as the roughness and aggregation shorted out the layered structure of the devices. But even with this process, current loss is still the major disadvantage of using SWNT over ITO, and smoother films will be necessary to cut those losses. In addition to roughness, inconsistency of films between batches is a problem comparing device performance. Degree of dispersion can vary between batches, which affects the yield upon completion of the centrifugation steps in the purification process. For this reason, SWNT prepared at the same time was used in experiments whenever possible. But in order make the processes more repeatable, to scale up the making of films and to be able to use SWNT grown and purified at different times, a further understanding of purification and dispersion is necessary.

CHAPTER 9 Conclusions and Future Research

9.1 Conclusions

A series of solvents and surfactants has been used to disperse SWNT, and films of different thickness were made from these solutions with different sonication times. A Figure of Merit that depends on conductivity and absorbance was proposed to assess the quality of the films, in order to compare films to one another. It was shown that surfactants, which bond to the surface of the SWNT, break down the SWNT into smaller bundles, and form films with higher conductivity at a given visible-spectrum transmittance. An ideal surfactant is one that will disperse SWNT as readily as non-nanotube carbon, without inducing sidewall defects or breaking down the nanotubes into amorphous carbon, and SDS was shown to have that quality.

Nanotube purity was shown to be a major deciding factor in film quality, and a purification method was developed specifically for thin film applications. Standard purification techniques were found to be inadequate, as the re-dispersion required for film manufacture results in a film of lower purity than the SWNT before being made into a film. Centrifugation of as-grown SWNT suspended in surfactant was shown to achieve higher purity films than films made from chemically purified SWNT in the same surfactant without centrifugation, an absorbance purity of 0.26 compared to 0.23. Films made with centrifugation of the chemically purified material was even only able to achieve a yield and purity equal to that of films prepared from centrifuged as-grown material. Thus, simple centrifugation was shown to be as effective at purification as multistep acid-oxidation and baking treatments in addition to a centrifugation step, when comparing purity and FOM of SWNT films. Centrifugation of chemically purified SWNT did have the advantage over centrifugation of as-grown SWNT, in that there were fewer aggregates

on the resultant film. The improvement from additional centrifugation of pre-purified material is largely due to the removal of these aggregates.

Nanotube films were doped with $SOCl_2$, ODCB, and HNO_3 by exposing the completed film to these dopants. This was done by either immersing the film in the dopant, or exposing the film to vapors of the dopant. By doping the SWNT after formation of the network, we were able to isolate the effects of dopants from effects of network morphology. It was shown that the S_{11} absorbance band is suppressed upon exposure to most dopants, and the conductivity change inflicted upon a given SWNT film is linearly proportional to the fractional change of S_{11} band intensity. This allows predictions to be made about film conductivity with only knowledge of the NIR absorbance spectrum, which would be particularly useful in changing film conductivity by controlling the degree of doping, as one could rely on in-situ measurements of absorbance rather than in-situ measurements of conductivity.

For SWNT networks of different thicknesses, doping was shown to change conductivity by a multiplicative amount, resulting in up to a factor of 19 increase in conductivity. This multiplicative factor depends on the dopant, and on the original method of dispersion. For different methods of dispersion (and therefore different resistance values for each given %T,) films of a given transmittance are doped by different multiplicative factors, but end up at the same post-doping resistance.

Doping also changes the frequency response of a SWNT, with the critical frequency changing linearly with the doping conductivity change. This means that for applications where frequency

dependent conductivity cutoff is desired, the cutoff frequency can be controlled independently of transmittance, by changing the degree of doping.

AC impedance response up to 8MHz has been measured and modeled. The model separated the impedance into two parts, an element from the SWNT themselves, and an element from the connections between the SWNT. Each element was found to have a resistance and capacitance part only. The AC measurements were carried out in a two-probe configuration, and compared to four probe DC measurements. Contributions from probe-tip resistance and capacitance was ruled out, both from the results of the impedance model, and from comparison of DC measurements to the low-frequency AC measurements. The impedance model was used to separate the contributions of the SWNT bundles themselves from the contributions of the junctions between bundles. Applied to doped networks, the model was able to separate the dopants' effect on nanotube bundles from the dopants' effect on nanotube junctions.

The percolation behavior of SWNT films prepared by different dispersants and with different SWNT purities was modeled. The percolation threshold of as-grown SWNT was shown to occur at over twice the loading of purified material, due to the inclusion of non-nanotube material with low aspect ratio. The critical exponent was not the dimensionally dependent 1.3 as predicted by most models, but was a higher value, ranging from 1.4 to 2.0, due to the bundles and junctions composing a wide distribution of conductivities. It was shown that the continuum of conductivities must be taken into account to accurately interpret not only the critical exponent, but also the conductivity prefactor.

Critical frequency was shown to obey the same percolation scaling law as conductivity. The probing length scale was found from this relationship. This length scale was proposed to arise from probing a distance between low-conductivity regions, junctions. The nonlinear dependence of length scale with nanotube density was explained in terms of the continuum model.

The performance of LED and PV devices that were fabricated with SWNT anodes showed that centrifugal purification was necessary for functional devices, and that film roughness is the major hindrance of device operation. Even so, the addition of a SWNT film to ITO substrate was shown to have a 300% improvement in power efficiency over ITO alone in an OLED.

9.2 Future Research

The SWNT in these networks have a fixed morphology, with a constant arrangement of bundles and number of junctions. Sidewall defects can be induced onto SWNT in the networks by heating, ozonation, or laser treatment. These would not change the morphology of the network. Doing this to a series of films would then allow us to study the effect of defects on critical frequency, and map the dependence of conductivity on Raman G/D ratio, and also to more directly determine and dependency of defects on absorbance purity.

Similarly, sufficiently high current will destroy metallic SWNT, leaving semiconducting SWNT intact. Creating a network with only semiconducting SWNT by these methods would change network morphology, but even so would give important information about transport behavior of networks composed of only one type of nanotube. This would be especially useful for studying

the mechanism of doping; the fractional change in resistance of an entirely semiconducting network would show how much the dopants effect semiconducting vs. metallic SWNT.

The multiplicative change of conductivity from a given dopant has not been shown to be loading-independent for the thinnest films, with transmittances above 93%T. Preparation of such films would allow percolation modeling of doped films. This is especially important in interpreting the experimental origin of the continuum distribution terms in the percolation equation. A loading-dependent multiplicative change in conductivity would result in a different critical exponent for doped films. This would indicate a change in the distribution of conductivities, while an unchanged critical exponent would indicate that the majority of transport occurs in a number of high-conductivity channels whose distribution remains unchanged during doping. From this reasoning, it is plausible that the stronger dopants would inflict a different change in the conductivity exponents than weaker dopants, and would be very interesting to see if the critical exponent changes from doping series of networks with different undoped critical exponents.

The contribution of bundles vs. junctions in the resistance of networks is still an important issue. Extremely thin films, both slightly above and below percolation threshold, could be made, and parallel electrodes deposited varying distances apart from one another. If those distances were in the range of a single bundle length, the impedance properties would have no junction dependence as the electrodes approached one another and passed that critical separation. The frequency response from this experiment would give information on the origins of the frequency-dependent length scale, and the resistance of inter-bundle connections could be deconvoluted

from the change in resistance as electrode spacing becomes larger than the single-bundle length. Since the films would be extremely thin, AFM measurements in addition to the resistance measurements would give the dimensions of a bundle, and the aspect ratio relations described in chapter 7.2 confirmed.

Electric Field Induced Contrast (EFIC) is a recently developed technique which allows transport to be actively observed in the SEM. For films very near percolation, observing which paths contribute to transport would be a valuable tool. It also allows transport paths to be observed even when the SWNT are embedded in polymer. The concentration of SWNT/PEDOT that makes the most effective OLED electrode likely is related to percolation threshold. EFIC imaging would illuminate those paths, and show at which concentration percolation occurs.

Through sufficiently low temperature ranges, metals and semiconductors have different behaviors, with the resistance of metals decreasing and the resistance of semiconductors increasing with decreasing temperature. Running such tests on SWNT films would determine which type of SWNT dominates film resistance. The predicted semiconducting and metallic percolation thresholds which occur at different film thicknesses could then be confirmed.

The weight yield of the centrifugation purification procedure has not been directly determined, nor has the change in metal content upon centrifugation. This purification method was developed specifically for thin film applications, so there is not a loose powder of SWNT at the end of the process. Special techniques would then be required to measure these things. Attempts were made to measure the weight of the films while still attached to the filter paper, and also to

detach the films from the paper to weigh separately. Films were also adhered onto TGA pans in order to determine metal content. The results of these experiments were inconclusive, beyond the reach of current techniques and equipment available to us at the time. These two results are important for judging the worth of any nanotube purification process, and should be pursued.

In the material purified by centrifugation, TEM images show larger amounts of catalyst particles in the samples nearest the bottom of the centrifuge tubes. Even if reliable TGA is not attainable from this purification process, the addition of non-nanotube carbon to the pre-centrifuged solution (without catalyst particles) would determine if the added density of the attached catalyst is the mechanism which separates nanotubes from the non-nanotube carbon during purification. Also, the differences in yield from purification with and without the added non-nanotube carbon would also tell us the relative amounts of nanotubes and non-nanotube carbon are preserved during the centrifugation process.

List of References

1. Ebbesen, T., *Carbon Nanotubes: Preparation and Properties*. 1997: CRC Press.
2. Samsonidze, G., et al., *The Concept of Cutting Lines in Carbon Nanotube Science.* Journal of Nanoscience and Nanotechnology, 2003. **3**: p. 431-457.
3. Hamada, N., S.-i. Sawada, and A. Oshiyama, *New one-dimensional conductors: Graphitic microtubules.* Physical Review Letters, 1992. **68**(10): p. 1579-1581.
4. Saito, R.F., M.; Dresselhaus, G.; Dresselhaus, M.S., *Electronic structure of chiral graphene tubules.* Applied Physics Letters, 1992. **60**(18): p. 2204.
5. Liu, *Polymer Electrolyte-Gated Carbon Nanotube Field-Effect Transistor.* Nano Letters, 2004. **4**(4): p. 623-627.
6. Snow, *Macroelectronic applications of carbon nanotube networks.* Solid State Electronics, 2004: p. 1753-1756.
7. Artukovic, E., et al., *Transparent and Flexible Carbon Nanotube Transistors.* Nano Letters, 2005. **5**(4): p. 757-760.
8. Lee, K.W., Z; Chen, Z; Ren, F; Pearton, S; Rinzler, A, *Single Wall Carbon Nanotubes for p-type Ohmic Contancts to GaN Light-Emitting Diodes.* Nano Letters, 2004. **4**(5): p. 911-914.
9. Aguirre, C., et al., *Carbon nanotube sheets as electrodes in organic light emitting diodes.* Applied Physics Letters, 2006. **88**: p. 183104-1 - 183104-3.
10. Du Pasquier, A.U., H; Kanwal, A; Miller, S; Chhowalla, M, *Conducting and transparent single-wall carbon nanotube electrodes for polymer-fullerene solar cells.* Applied Physics Letters, 2005. **87**: p. 203511-1 - 203511-3.
11. Rowell, M.T., M; Mcgehee, M; Prall, H; Dennler, G; Sariciftci, N; Hu, L; Gruner, G, *Organic solar cells with carbon nanotube network electrodes.* Applied Physics Letters, 2006. **88**: p. 233506-1 -233506-3.
12. Gordon, R., *Criteria for Choosing Transparent Conductors.* MRS Bulliten, 2000. **25**(8): p. 52-57.
13. Green, A. and M. Hersam, *Colored Semitransparent conductive Coatings Consisting of Monodisperse Metallic Single-Walled Carbon Nanotubes.* Nano Letters, 2008. **8**: p. 1417-1422.
14. Hu, L., D.S. Hecht, and G. Gruner, *Percolation in Transparent and Conducting Nanotube Networks.* Nano Letters, 2004. **4**: p. 2513-2517.
15. Unalan, H.E., et al., *Design Criteria for Transparent Single-Wall Carbon Nanotube Thin-Film Transistors.* Nano Letters, 2006. **6**: p. 677-682.
16. Williams, Q.L., et al., *Boron-doped carbon nanotube coating for transparent, conducting, flexible photonic devices.* Applied Physics Letters, 2007. **91**: p. 143116.
17. Bertoni, C., V. Skakalova, and S. Roth, *Layer-by-layer deposition of ultra-thin films of carbon nanotubes.* Physica E, 2008. **40**: p. 2257-2262.
18. Castro, M.R.S. and H.K. Schmidt, *Preparation and characterization of low- and high-adherent transparent multi-walled carbon nanotube thin films.* Materials Chemistry and Physics, 2008. **111**: p. 317-321.
19. Ng, M.H.A., et al., *Efficient coating of transparent and conductive carbon nanotube thin films on plastic substrates.* Nanotechnology, 2008. **19**: p. 205703.
20. Gruner, G., *Carbon nanotube films for transparent and plastic electronics.* Journal of Materials Chemistry, 2006. **16**: p. 3533-3539.

21. Li, Z., et al., *Does the wall number of carbon nanotubes matter as conductive transparent material.* Applied Physics Letters, 2007. **91**: p. 053115.
22. Geng, H., et al., *Effect of Acid Treatment on Carbon Nanotube-Based Flexible Transparent Conducting Films.* Journal of the American Chemical Society, 2007. **129**: p. 7758-7759.
23. Huang, L., et al., *Self-organizing high-density single-walled carbon nanotube arrays from surfactant suspensions.* Nanotechnology, 2004. **15**: p. 1450-1454.
24. Wu, Z.C., Z; Du, X; Logan, J; Sippel, J; Nikolou, M; Kamaras, K; Reynolds, J; Tanner, D; Hebard, A; Rinzler, A, *Transparent, Conductive Carbon Nanotube Films.* Science, 2004. **305**: p. 1273-1276.
25. Hennrich, F.L., S; Malik, S; Tracy, J; Barczewski, M; Rosner, H; Kappes, M, *Preparation, characterization and applications of free-standing single walled carbon nanotube thin films.* Physical Chemistry Chemical Physics, 2002: p. 2273-2277.
26. Buldum, A. and J.P. Lu, *Contact resistance between carbon nanotubes.* Physical Review B, 2001. **63**(16): p. 161403-1 -161403-4.
27. Zhou, C.K., J; Dai, H, *Electrical measurements of individual semiconducting single-walled carbon nanotubes of various diameters.* Applied Physics Letters, 2000. **76**(12): p. 1597-1599.
28. Kong, J.Z., C; Morpurgo, A; Soh, H; Quate, C; Marcus, C; Dai, H, *Synthesis, integration, and electrical properties of individual single-walled carbon nanotubes.* Applied Physics A, 1999. **69**: p. 305-308.
29. Bezryadin, A., et al., *Multiprobe Transport Experiments on Individual Single-Walled Carbon Nanotubes.* Physical Review Letters, 1998. **80**(18): p. 4036-4039.
30. Fuhrer, M., et al., *Crossed Nanotube Junctions.* Science, 2000. **288**: p. 494-497.
31. Pike, G. and C. Seager, *Percolation and conductivity: A computer study.* Physical Review B, 1974. **10**(4): p. 1421-1434.
32. Snow, E.N., J; Campbell, P; Park, D, *Random networks of carbon nanotubes as an electronic material.* Applied Physics Letters, 2003. **82**(13): p. 2145-2147.
33. Blackburn, J.L., et al., *Transparent Conductive Sigle-Walled Carbon Nanotube Networks with Precisely Tunable Ratios of Semiconducting and Metallic Nanotubes.* ACS Nano, 2008. **2**: p. 1266-1274.
34. Dettlaff-Weglikowska, U., et al., *Effect of $SOCl_2$ Treatment on Electrical and Mechanical Properties of Single-Wall Carbon Nanotube Networks.* Journal of the American Chemical Society, 2005. **127**(14): p. 5125-5131.
35. Kovtyukhova, N.I., et al., *Individual Single-Walled Nanotubes and Hydrogels Made by Oxidative Exfoliation of Carbon Nanotube Ropes.* Journal of the American Chemical Society, 2003. **125**: p. 9761-9769.
36. Minami, N., et al., *Cellulose Derivatives as excellent dispersants for single-wall carbon nanotubes as demonstrated by absorption and photoluminescence spectroscopy.* Applied Physics Letters, 2006. **88**: p. 093123.
37. Skakalova, V.K., A; Dettlaff-Weglikowska, U; Hrncarikova, K; Roth, S, *Effect of Chemical Treatment on Electrical Conductivity, Infrared Asorption,and Raman Sectra of Single-Walled Carbon Nanotubes.* Journal of Physical Chemistry B, 2005. **109**(15): p. 7174-7181.

38. Itkis, M., et al., *Purity Evaluation of As-Prepared Single-Walled Carbon Nanotube Soot by Use of Solution-Phase Near-IR Spectroscopy.* Nano Letters, 2003. **3**: p. 309-314.
39. Valdes, L.B., *Resistivity Measurements on Germanium for Transistors.* Procedings of the IRE, 1954: p. 420-427.
40. Uhlir, A., *The Potentials of Infinite Systems of Sources and Numerical Solutions of Problems in Semiconductor Engineering.* . The Bell System Technical Journal, 1955: p. 105-128.
41. Smits, F.M., *Measurement of Sheet REsistivities with the Four-Point Probe.* The Bell System Technical Journal, 1958: p. 710-718.
42. Sunde, E.D., *Earth Conduction Effects in Transmission Systems*. 1949, New York: D Van Nostrand Company, Inc. p45.
43. Kataura, H., et al., *Optical Properties of Single-Wall Carbon Nanotubes.* Synthetic Metals, 1999. **103**: p. 2555-2558.
44. Jorio, A., et al., *Characterizing carbon nanotube samples with resonance Raman scattering.* New Journal of Physics, 2003. **5**: p. 139.1-139.17.
45. Wang, F., et al., *The optical Resonances in Carbon Nanotubes Arise from Excitons.* Science, 2005. **308**: p. 838-841.
46. Spataru, C., et al., *Excitonic Effects and Optical Spectra of Single-Walled Carbon Nanotubes.* Physical Review Letters, 2004. **92**: p. 077402.
47. Itkis, M.E., et al., *Comparison of Analytical Techniques for Purity Evaluation of Single-Walled Carbon Nanotubes.* Journal of the American Chemical Society, 2005. **127**: p. 3439-3448.
48. Landi, B.J., et al., *Purity Assessment of Single-Wall Carbon Nanotubes, Using Optical Absorption Spectroscopy.* Journal of Physical Chemistry B, 2005. **109**: p. 9952-9965.
49. Freiman, S., et al., *Measurement Issues in Single Walled Carbon Nanotubes*, in *NIST Recommended Practice Guide*. 2008, NIST: Washington, DC.
50. Thomsen, C. and S. Reich, *Raman Scattering in Carbon Nanotubes*. Light Scattering in Solids IX, ed. R.M. M Cardona. 2006: Springer-Verlag.
51. *Raman Spectroscopy Tutorial*. 2008, Kaiser Optical Systems.
52. Saito, R., et al., *First and Second-Order Resonance Raman Process in Graphite and SingleWall Carbon Nanotubes.* Japanese Jounal of Applied Physics, 2002. **41**: p. 4878-4882.
53. Saito, R., et al., *Double resonance Raman spectroscopy of single-wall carbon nanotubes.* New Journal of Physics, 2003. **5**: p. 157.1-157.15.
54. Dillon, A.C., et al., *Systematic inclusion of defects in pure carbon single-wall nanotubes and their effect on the Raman D-band.* Chemical Physics Letters, 2005. **401**: p. 522–528.
55. Heller, D.A., et al., *Using Raman Spectroscopy to Elucidate the Aggregation State of Single-Walled Carbon Nanotubes.* Journal of Physical Chemistry B, 2004. **108**: p. 6905-6909.
56. Maultzsch, J., et al., *Radial breathing mode of single-walled carbon nanotubes: Optical transition energies and chiral-index assignment.* Physical Review B, 2005. **72**: p. 205438.
57. Rao, A.M., et al., *Effect of van derWaals Interactions on the Raman Modes in SingleWalled Carbon Nanotubes.* Physical Review Letters, 2001. **86**: p. 3895-3898.

58. Tuinstra, F. and J.L. Koenig, *Raman Spectrum of Graphite.* Journal of Chemical Physics, 1970. **53**: p. 1126-1130.
59. Pimenta, M.A., et al., *Diameter dependence of the Raman D-band in isolated single-wall carbon nanotubes.* Physical Review B, 64. **64**: p. 041401.
60. Filho, A.G.S., et al., *Competing spring constant versus double resonance effects on the properties of dispersive modes in isolated single-wall carbon nanotubes.* Physical Review B, 2003. **67**: p. 035427.
61. Ohno, Y., et al., *Raman Scattering of Single-Walled Carbon Nanotbes Implanted with Ultra-Low-Energy Oxygen Ions.* Japanese Jounal of Applied Physics, 2005. **44**: p. 1615-1620.
62. Jorio, A., et al., *Carbon Nanotube Photophysics.* MRS Bulliten, 2004: p. 276-280.
63. Fraser, D.B. and H.D. Cook, *Highly Conductive, Transparent Films of Sputtered* $In_{2-x}Sn_xO_{3-y}$. Journal of the Electrochemical Society, 1972. **119**: p. 1368-1374.
64. Haacke, G., *New figure of merit for transparent conductors.* Journal of Applied Physics, 1976. **47**: p. 4086-4089.
65. Niyogi, S., et al., *Ultrasonic Dispersions of Single-Walled Carbon Nanotubes.* Journal of Physical Chemistry B, 2003. **107**: p. 8799-8804.
66. Kim, D.S., D. Nepal, and K.E. Geckeler, *Individualization of Single-Walled Carbon Nanotubes: Is the Solvent Important?* Small, 2005. **1**: p. 1117-1124.
67. R Schonfelder, M.H.R., W Gruner, M Loffler, J Acker, V Hoffmann, T Gemming, B Buchner and T Pichler, *Purification-induced sidewall functionalization of magnetically pure single-walled carbon nanotubes.* Nanotechnology, 2007. **18**: p. 375601.
68. A.G. Rinzler, J.L., H. Dai, P. Nikolaev, C.B. Huffman, F.J. Rodríguez-Macías, P.J. Boul, A.H. Lu, D. Heymann, D.T. Colbert, R.S. Lee, J.E. Fischer, A.M. Rao, P.C. Eklund, R.E. Smalley, *Large-scale purification of single-wall carbon nanotubes: process, product, and characterization.* Applied Physics A, 1998. **67**: p. 29-37.
69. Jinyong Li, Y.Z., *A simple purification for single-walled carbon nanotubes.* Physica E, 2005. **28**: p. 309-312.
70. Huanjun Li, L.F., Lunhui Guan, Zujin Shi, Zhennan Gu, *Synthesis and purification of single-walled carbon nanotubes in the cottonlike soot.* Solid State Communications, 2004. **132**: p. 219-224.
71. Aiping Yu, E.B., Mikhail E. Itkis, Danylo Fakhrutdinov, and a.R.C.H. Robert Webster, *Application of Centrifugation to the Large-Scale Purification of Electric Arc-Produced Single-Walled Carbon Nanotubes.* Journal of the American Chemical Society, 2004. **128**: p. 9902-9908.
72. Hui Hu, A.Y., Eric Kim, Bin Zhao, Mikhail E. Itkis, Elena Bekyarova, and Robert C. Haddon, *Influence of the Zeta Potential on the Dispersability and Purification of Single-Walled Carbon Nanotubes.* journal of Physical Chemistry B, 2005. **109**: p. 11520-11524.
73. A. C. Dillon, T.G., K. M. Jones, J. L. Alleman, P. A. Parilla, M. J. Heben, *A Simple and Complete Purification of Single-Walled Carbon Nanotube Materials.* Advanced Materials, 1999. **11**(16): p. 1354-1358.
74. I. W. Chiang, B.E.B., R. E. Smalley, J. L. Margrave, and R. H. Haug, *Purification and Characterization of Single-Wall Carbon Nanotubes.* Journal of Physical Chemistry B, 2001. **105**: p. 1157-1161.

75. Hisashi Kajiura, S.T., Houjin Huang, Yousuke Murakami, *High-quality single-walled carbon nanotubes from arc-produced soot.* Chemical Physics Letters, 2002. **364**: p. 586-592.
76. Avetik R. Harutyunyan, B.K.P., Jiping Chang, Gugang Chen, and and P.C. Eklund, *Purification of Single-Wall Carbon Nanotubes by Selective Microwave Heating of CatalystParticles.* Journal of Physical Chemistry B, 2002. **106**: p. 8671-8675.
77. Shunji Bandow, A.M.R., K. A. Williams, A. Thess, R. E. Smalley, and P. C. Eklund, *Purification of Single-Wall Carbon Nanotubes by Microfiltration.* Journal of Physical Chemistry B, 1997. **101**: p. 8839-8842.
78. Jeong-Mi Moon, K.H.A., Young Hee Lee, Young Soo Park, Dong Jae Bae, Gyeong-Su Park, *High-Yield Purification Process of Singlewalled Carbon Nanotubes.* Journal of Physical Chemistry B, 2001. **105**: p. 5677-5681.
79. John L. Zimmerman, R.K.B., Chad B. Huffman, Robert H. Hauge, and John L. Margrave, *Gas-Phase Purification of Single-Wall Carbon Nanotubes.* Chemistry of Materials, 2000. **12**: p. 1361-1366.
80. Shelimov, K.B.E., R. O.; Rinzler, A. G.; Huffman, C. B.; Smalley, S. E. , *Purification of single-wall carbon nanotubes by ultrasonically assisted filtration.* Chemical Physics Letters, 1998. **282**: p. 429-434.
81. M. T. Martínez, M.A.C., A. M. Benito, W. K. Maser, M. Cochet, J. M. Andrés, J. and O.C. Schreiber, and J. L. G. Fierro, *Microwave single walled carbon nanotubes purification.* Chemical Communications, 2002. **9**: p. 1000.
82. J.G. Wiltshire, A.N.K., L.J. Li, S.G. Lyapin, G.A.D. Briggs, R.J. Nicholas, *Comparative studies on acid and thermal based selective purification of HiPCO produced single-walled carbon nanotubes.* Chemical Physics Letters, 2004. **386**: p. 239-243.
83. Karla L. Strong , D.P.A., Khalid Lafdi, John N. Kuhn, *Purification process for single-wall carbon nanotubes.* Carbon, 2002. **41**: p. 1477–1488.
84. Houjin Huang, H.K., Atsuo Yamada, Masafumi Ata, *Purification and alignment of arc-synthesis single-walled carbon nanotube bundles.* Chemical Physics Letters, 2002. **356**: p. 567–572.
85. Landi, B., et al., *Thermal Oxidation Profiling of Single-Walled Carbon Nanotubes.* Chemistry of Materials, 2005. **17**: p. 6819-6834.
86. M. Monthioux, B.W.S., B. Burteaux, A. Claye, J.E. Fischer, D.E. Luzzi, *Sensitivity of single-wall carbon nanotubes to chemical processing: an electron microscopy investigation.* Carbon, 2001. **39**: p. 1251-1272.
87. E.T. Mickelson, C.B.H., A.G. Rinzler, R.E. Smalley, R.H. Hauge, J.L. Margrave, *Fluorination of single-wall carbon nanotubes.* Chemical Physics Letters, 1998. **296**: p. 188-194.
88. C. A. Furtado, U.J.K., H. R. Gutierrez, Ling Pan, E. C. Dickey, and Peter C. Eklund, *Debundling and Dissolution of Single-Walled Carbon Nanotubes in Amide Solvents.* Journal of the American Chemical Society, 2004. **2004**: p. 6095-6105.
89. Tour, C.A.D.a.J.M., *Solvent-Free Functionalization of Carbon Nanotubes.* Journal of the American Chemical Society, 2003. **125**: p. 1156-1157.
90. Shuhui Qin, D.Q., Warren T. Ford, Jose E. Herrera, Daniel E. Resasco, Sergei M. Bachilo, and R. Bruce Weisman, *Solubilization and Purification of Single-Wall Carbon*

Nanotubes in Water by in Situ Radical Polymerization of Sodium 4-Styrenesulfonate. Macromolecules, 2004. **37**: p. 3965-3967.
91. R Schonfelder, M.H.R., W Gruner, M Loffler, J Acker, V Hoffmann, T Gemming, B Buchner and T Pichler, *Purification-induced sidewall functionalization of magnetically pure single-walled carbon nanotubes.* Nanotechnology, 2007. **18**.
92. Avetik R. Harutyunyan, B.K.P., Jiping Chang, Gugang Chen, and Peter C. Eklund, *Purification of Single-Wall Carbon Nanotubes by Selective Microwave Heating of Catalyst Particles.* Journal of Physical Chemistry B, 2002. **106**: p. 8671-8675.
93. Bin Zhao, H.H., Sandip Niyogi, Mikhail E. Itkis, Mark A. Hamon, Paragranjita Bhowmik, Mark S. Meier, and Robert C. Haddon, *Chromatographic Purification and Properties of Soluble Single-Walled Carbon Nanotubes.* Journal of the American Chemical Society, 2001. **123**: p. 11673-11677.
94. M. T. Martínez, M.A.C., A. M. Benito, W. K. Maser, M. Cochet, J. M. Andrés, J. and O.C.a.J.L.G.F. Schreiber, *Microwave single walled carbon nanotubes purification.* Chemical Communications, 2002: p. 1000-1001.
95. E. Gregan , S.M.K., A. Maguire, T.G. Hedderman, L.O. Neill, G. Chambers, H.J. Byrne, *Purification and isolation of SWNTs.* Carbon, 2004. **42**: p. 1031-1035.
96. A.G. Ryabenko , T.V.D., G.I. Zvereva, *UV–VIS–NIR spectroscopy study of sensitivity of single-wall carbon nanotubes to chemical processing and Van-der-Waals SWNT/SWNT interaction. Verification of the SWNT content measurements by absorption spectroscopy.* Carbon, 2004. **42**: p. 1523-1535.
97. Nepal, D., D.S. Kim, and K.E. Geckeler, *A facile and rapid purification method for single-walled carbon nanotubes.* Carbon, 2005. **43**: p. 651-673.
98. Michael J. O'Connell, S.M.B., Chad B. Huffman, Valerie C. Moore, Michael S. Strano, Erik H. Haroz, Kristy L. Rialon, Peter J. Boul, William H. Noon, Carter Kittrell, Jianpeng Ma, Robert H. Hauge, R. Bruce Weisman, Richard E. Smalley, *Band Gap Fluorescence from Individual Single-Walled Carbon Nanotubes.* Science, 2002. **297**: p. 593-596.
99. T. Murakami , K.K., T. Tokuda, K. Matsumoto, H. Harima, K. Mitikami, T. Isshiki, *Raman and photoluminescence from dispersed single walled carbon nanotubes.* Diamond and Related Materials, 2007. **16**: p. 1192-1194.
100. E. Artukovic, M.K., D. S. Hecht, S. Roth, G. Gru1ner, *Transparent and Flexible Carbon Nanotube Transistors.* Nano Letters, 2005. **5**: p. 757-760.
101. Frank Hennrich, S.L., Sharali Malik, Joseph Tracy, Matthias Barczewski, Harald Rosner and Manfred Kappes, *Preparation, characterization and applications of free-standing single walled carbon nanotube thin films.* Physical Chemistry Chemical Physics, 2002. **4**: p. 2273-2277.
102. Holm, *Electric Contacts: Theory and Application*. 1967, New York: Springer-Verlag.
103. Albers, J. and H.L. Berkowitz, *The Relation Between Two-Probe and Four Probe Resistances on Nonuniform Structures.* Journal of the Electrochemical Society Solid-State Science and Technology, 1984. **131**(2): p. 392-398.
104. Novosel'skii, I.M., N.N. Gudina, and Y.I. Fetistov, *Identical Equivalent Impedance Circuits.* Soviet Elektrokhimiya, 1972. **8**: p. 565-567.
105. Bauerle, J.E., *Study of Solid Electrolyte Polarization by a complex Admittance Method.* Journal of Physics and Chemistry of Solids, 1969. **30**: p. 2657-2670.

106. Hsieh, G., et al., *Experimental limitations in impedance spectroscopy: Part VI. Four-point measurements of solid material systems.* Solid State Ionics, 1997. **100**: p. 297-311.
107. Vladikova, D. *The Technique of the Differential Impedance Analysis Part I: Basics of the Impedance Spectroscopy*. in *Proceedings of the International Workshop "Advanced Techniques for Energy Sources Investigation and Testing"* 2004. Sofia, Bulgaria.
108. Dygas, J.R., G. Fafilek, and M.W. Breiter, *Study of grain boundary polarization by two-probe and four-probe impedance spectroscopy.* Solid State Ionics, 1999. **119**: p. 115-125.
109. Esfarjani, K., et al., *Nonlinear Charging and Transport in Doped Nanotubes Junctions.* Journal of the Physical Society of Japan, 2005. **74**: p. 515-518.
110. Macdonald, J.R., *Impedance Spectroscopy*. 1987, New York: John Wiley & Sons.
111. Fernandes, E., D. Soares, and A. DeQueiroz, *Electrical properties of electrodeposited polyaniline nanotubes.* Journal of Materials Science: Materials in Electronics, 2008. **19**: p. 457-462.
112. Loh, K., et al., *Tailoring Piezoresistive Sensitivty of Mulitlayer Carbon Nanotube composite Strain Sensors.* Journal of Intelligent Materials Systems and Structures, 2008. **19**: p. 747-764.
113. Hennrich, F., et al., *Reversible modification of the absorption properties of single-walled carbon nanotube thin films via nitric acid exposure.* Physical Chemistry Chemical Physics, 2002. **5**: p. 178-183.
114. Liu, J., et al., *Fullerene Pipes.* Science, 1998. **280**: p. 1253-1256.
115. Niyogi, S., et al., *Chemistry of Single-Walled Carbon Nanotubes.* Accounts of Chemical Research, 2002. **35**: p. 1105-1113.
116. Geng, H., et al., *Doping and de-doping of carbon nanotube transparent conducting films by dispersant and chemical treatment.* Journal of Materials Chemistry, 2007. **18**: p. 1261-1266.
117. Monthioux, M., et al., *Sensitivity of single-wall carbon nanotubes to chemical processing: an electron microscopy investigation.* Carbon, 2001. **39**: p. 1251-1272.
118. Zhou, W.V., J; Nemes, N; Fischer, J; Borondics, F; Kamaras, K; Tanner, D, *Charge transfer and Fermi level shift in p-doped single-walled carbon nanotubes.* Physical Review B, 2005. **71**: p. 2052443-1 -205243-7.
119. Barnes, T., et al., *Reversibility, Dopant Desorption, and Tunneling in the Temperature-Dependent Conductivity of Type-Separated, Conductive Carbon Nanotube Networks.* ACS Nano, 2008. **2**: p. 1968-1976.
120. Yu, Z. and L. Brus, *Reversible Oxidation Effect in Raman Scattering from Metallic Single-Walled Carbon Nanotubes.* Journal of Physical Chemistry A, 2000. **103**: p. 10995-10999.
121. Bower, C., et al., *Intercalation and partial exfolation of single-walled carbon nanotubes by nitric acid.* Chemical Physics Letters, 1998. **288**: p. 481-486.
122. Graupner, R., et al., *Doping of single-walled carbon nanotube bundles by Bronstead acids.* Physical Chemistry Chemical Physics, 2003. **5**: p. 5472-5476.
123. Kulesza, S., et al., *High-temperature electrical transport properties of buckpapers composed of doped single-walled carbon nanotubes.* Carbon, 2006. **44**: p. 2178-2183.
124. Krupke, R., et al., *Seperation of Metallic from Semiconducting Single-Walled Carbon Nanotubes.* Science, 2003. **301**: p. 344-347.

125. Arnold, M.S., et al., *Sorting carbon nanotubes by electronic structure using density differentiation.* Nature Nanotechnology, 2006. **1**: p. 60-65.
126. Chen, Z., et al., *Metallic/Semiconducting Nanotube Seperation and Ultra-thin Transparent Nanotube Films.* Electronic Properties of Synthetic Nanostructures, 2004: p. 69-74.
127. Kavan, L. and L. Dunsch, *Diameter-Selective Electrochemical Doping of HiPco Single-Walled Carbon Nanotubes.* Nano Letters, 2003. **3**(7): p. 969-972.
128. Kavan, L., et al., *Electrochemical Doping of Chirality -Resolved Carbon Nanotubes.* Journal of Physical Chemistry B, 2005. **109**: p. 19613-19619.
129. Rao, A., et al., *Evidince for charge transfer in doped carbon nanotube bundles from Raman scattering.* Nature, 1997. **388**: p. 257-259.
130. Strano, M., et al., *Reversible, Band-Gap-Selective Protonation of Single-Walled Carbon Nanotubes in Solution.* Journal of Physical Chemistry B, 2003. **107**: p. 6979-6985.
131. Gu, Z., et al., *In situ Raman studies on lithiated single-wall carbon nanotubes in liquid ammonia.* Chemical Physics Letters, 2005. **410**: p. 467-470.
132. Fagan, S., et al., *1,2-Dichlorobenzene Interacting with Carbon Nanotubes.* Nano Letters, 2004. **7**: p. 1285-1288.
133. Graupner, R., *Raman spectroscopy of covalently functionalized single-wall carbon nanotubes.* Journal of Raman Spectroscopy, 2007. **38**: p. 673-683.
134. Rafailov, P.M., et al., *Raman Spectroelectrochemistry on SWNTs at higher doping levels: Evidence for a transition to intercalative doping.* Physica Status Solidi (b), 2007. **244**(11): p. 4060-4063.
135. Hu, L., D.S. Hecht, and G. Gruner, *Percolation in transparent and conducting carbon nanotube networks.* Nano Letters, 2004. **4**(12): p. 2513-2517.
136. Kumar, S., J.Y. Murthy, and M.A. Alam, *Percolating conduction in finite nanotube networks.* Physical Review Letters, 2005. **95**(6): p. 066802.
137. Snow, E.S., et al., *Random networks of carbon nanotubes as an electronic material.* Applied Physics Letters, 2003. **82**(13): p. 2145-2147.
138. Bocharova, V., et al., *Ultrathin Transparent Conductive Films of Polymer-Modified Multiwalled Carbon Nanotubes.* Journal of Physical Chemistry B, 2006. **110**: p. 14640-14644.
139. Pike, G.E. and C.H. Seager, *Percolation and conductivity: A computer study. I.* Physical Review B (Solid State), 1974. **10**(4): p. 1421-34.
140. Balberg, I. and N. Binenbaum, *Computer study of the percolation threshold in a two-dimensional anisotropic system of conducting sticks.* Physical Review B (Condensed Matter), 1983. **28**(7): p. 3799-812.
141. Schmidt, R.H., et al., *The effect of aggregation on the electrical conductivity of spin-coated polymer/carbon nanotube composite films.* Langmuir, 2007. **23**(10): p. 5707-5712.
142. Wescott, J.T., P. Kung, and A. Maiti, *Conductivity of carbon nanotube polymer composites.* Applied Physics Letters, 2007. **90**(3): p. 033116.
143. Coleman, J.N., et al., *Physical doping of a conjugated polymer with carbon nanotubes.* Synthetic Metals, 1999. **102**(1-3 pt 2): p. 1174-1175.
144. Grossiord, N., et al., *On the crucial role of wetting in the preparation of conductive polystyrene-carbon nanotube composites.* Chemistry of Materials, 2007. **19**(15): p. 3787-3792.

145. Kymakis, E., I. Alexandou, and G.A.J. Amaratunga. *Single-walled carbon nanotube-polymer composites: Electrical, optical and structural investigation*. 2002. Strasbourg: Elsevier Science Ltd.
146. Kymakis, E. and G.A.J. Amaratunga, *Electrical properties of single-wall carbon nanotube-polymer composite films.* Journal of Applied Physics, 2006. **99**(8): p. 084302.
147. McLachlan, D., et al., *AC and DC Percolative Conductivity of Single Wall Carbon Nanotube Polymer Composites.* Journal of Polymer Science, 2005. **43**: p. 3273-3287.
148. Unalan, H.E., et al., *Design criteria for transparent single-wall carbon nanotube thin-film transistors.* Nano Letters, 2006. **6**(4): p. 677-682.
149. Giovanni Fanchini, H.E.U., Manish Chhowalla, *Optoelectronic properties of transparent and conducting single-wall carbon nanotube thin films.* Applied Physics Letters, 2006. **88**: p. 191919.
150. N. Pimparkar, Q.C., S. Kumar, J. Y. Murthy, J. Rogers, M. A. Alam, *Current-Voltage Characteristics of Long-Channel Nanobundle Thin-Film Trnsistors: A BottomUp Perspective.* IEEE Electron Device Letters, 2007. **28**(2): p. 157-160.
151. Lagarkov, A.N. and A.K. Sarychev, *Electromagnetic properties of composites containing elongated conducting inclusions.* Physical Review B, 1996. **53**: p. 6318-6336.
152. Balberg, I., et al., *Excluded volume and its realtion to the onset of percolation.* Phsical Review B, 1984. **30**: p. 3933-3943.
153. Stauffer, D. and A. Aharony, *Intorduction to Percolation Theory*. Second ed. 1992, Washington DC: Taylor & Francis.
154. Balberg, I., *Recent developments in continuum percolation.* Philisophical Magazine B, 1987. **56**: p. 991-1003.
155. Bekyarova, E., et al., *Electronic Properties of Single-Walled Nanotube Networks.* Journal of the American Chemical Society, 2004. **127**: p. 5990-5995.
156. Feng, S., B. Halperin, and P. Sen, *Transport properties of continuum systems near percolation threshold.* Physical Review B, 1987. **35**: p. 197-214.
157. Kogut, P.M. and J.P. Straley, *Distribution-induced non-universality of the percolation threshold.* Journal of Physics C, 1979. **12**: p. 2151-2159.
158. Ounaies, Z., et al., *Electrical properties of single wall carbon nanotube reinforced polyimide composites.* Composites Science and Technology, 2003. **63**: p. 1637-1646.
159. Fanchini, G., H. Unalan, and M. Chhowalla, *Optoelectronic properties of transparent and conducting single-wall carbon nanotube thin films.* Applied Physics Letters, 2006. **88**: p. 191919.
160. Kilbride, B.E., et al., *Experimental observation of scaling laws for alternating current and direct current conductivity in polymer-carbon nanotube composite thin films.* Journal of Applied Physics, 2002. **92**: p. 4024-4030.
161. Keblinski, P. and F. Cleri, *Contact Resistance in Percolating Networks.* Physical Review B, 2004. **69**: p. 184201.
162. Archie, G., *The Electrical Resistivity Log as and Aid in Determining Some Reservoir Characteristics.* Transactions of AIME, 1942. **146**: p. 54-62.
163. Xu, H., et al., *Frequency- and electric-field-dependent conductivity of single-walled carbon nanotube networks of varying density.* Physical Review B, 2008. **77**: p. 075418-1-6.

164. Halperin, B.I., S. Feng, and P.N. Sen, *Differences Between Lattice and Continuum Percolation Transport Exponents.* Physical Review Letters, 1985. **54**: p. 2391-2394.
165. Godlewski, J. and M. Obarowska, *Organic light emitting devices.* Opto-electronics Review. **15**: p. 179-183.
166. Wang, G.F., et al., *Improvement in performance of light-emitting devices by inclusion of multi-wall carbon nanotubes.* Journal of Luminescence, 2007. **16**: p. 602-606.

Vita

Matthew Garrett was born in Richmond, Virginia on October 29, 1980. He graduated in 2002 with university honors from Virginia Commonwealth University with a major in physics and minor in mathematics. He went on to the University of Tennessee, where he received his doctoral degree in 2009.